Thermomechanical processing of Al-Ce-based alloys and their mechanical properties for elevated temperature applications

by

Humphrey Wara Odhiambo

A dissertation submitted to the graduate faculty

In partial fulfilment of the requirements for the degree of

DOCTOR OF PHILOSOPHY

Major: Materials Science and Engineering

Academic Plan Committee:

Jun Cui, Major Professor

Ralph Napolitano

Patrick Johnson

Sid Pathak

Shan Hu

The student author, whose presentation of the scholarship herein was approved by the Academic Plan Committee, is solely responsible for the content of this dissertation. The Graduate College will ensure this dissertation is globally accessible and will not permit alterations after a degree is conferred.

Iowa State University of Science and Technology

Ames, Iowa

2025

DEDICATION

I dedicate this work to my late father, George Washington Odhiambo Wara, a devoted educator, father, and mentor. His legacy of hard work continues to inspire me. Though his journey ended far too soon, his presence lives on in our hearts.

CHAPTER 1: TABLE OF CONTENTS

Page

LIST OF FIGURES

Page

LIST OF SUPPLEMENTARY FIGURES

Page

LIST OF TABLES

Page

ACKNOWLEDGEMENTS

We stand on the shoulders of giants who preceded us. My PhD journey has been a humbling experience of confidently exploring the unknown. Along the way, I have learned profoundly from the scientific community at Iowa State University - the values of discipline, consistency, hard work, and professionalism. I once told my friend, Dr. ChaoChao Pan, that I was eager to meet the person I would become at the end of this program. Today, I am proud of that person. My thirst for knowledge remains unquenched, reminding me that this is only one step in a lifelong journey of discovery. May those who come after me find this journey exhilarating in equal measure.

To my committee members, I am grateful for your support and wise counsel at every stage of this journey, helping me remain true to the highest precepts of professionalism. I also extend my gratitude to our funding partners – the Ames National Laboratory, the U.S. Department of Energy, and Iowa State University – without whose resources and contributions this work would not have been possible. To my colleagues in Prof. Cui's lab, thank you for your input in my research and for the positive spirit you bring to our work environment.

I would also like to acknowledge our collaborators at Rensselaer Polytechnic Institute and GE Aerospace. Working with you has been both rewarding and enlightening, and I look forward to future collaborations. More broadly, I remain indebted to every individual who contributed – whether in obvious or subtle ways – by offering guidance along the way. I also deeply appreciate the many professors who welcome students from across the world into their programs, mentoring them with commitment and dedication, securing resources through tireless proposal writing, and ensuring that their students are prepared to contribute meaningfully to the world of science and technology.

I am especially thankful to Prof. Jun Cui, whom I approached in 2022 in search of a mentor; in him, I found one. I remain deeply grateful for his mentorship, scientific reasoning, and unwavering support. I also owe special thanks to Dr. Ouyang Gaoyuan, scientist at Ames National Laboratory, whose patience, composure, and insights have shaped my growth as a researcher. I cannot imagine how many mistakes I made or how much ignorance I exhibited in training, but his patience in correcting and guiding me has been invaluable. To Prof. Napolitano, I sincerely appreciate your mentorship and guidance; the experiments we

conducted in our collaborative project remain deeply ingrained as a reference point that will inform my future career as a researcher.

Finally, I owe heartfelt gratitude to my family. To my brothers Cliffe, Fordam, Nick, Elvis, Gerald, thank you for believing in my dreams and supporting them - you have always been perfect gentlemen, and this PhD is your victory as well. To my mother, Loice Odhiambo, your faith in me and encouragement to begin this journey remain a source of pride and strength. To my loving wife, Daizy, thank you for standing steadfastly by my side throughout this journey - this achievement is as much yours as is mine. Above all, gratitude and praise be to God.

This Project Funded by U.S. Department of Energy (DOE) under Grant No. DE-EE0010219 document number AL-T 3389.

ABSTRACT

Aluminum is lightweight, castable, corrosion resistant, and the most abundant structural metal in the Earth's crust, making it indispensable in automotive and aerospace applications. However, the common limitation to the application of Al alloys is their limited operating temperature range. A low melting temperature range is associated with grains and precipitate coarsening at temperatures higher than ~200ºC [25]. Current commercial Al alloys exhibit rapid strength degradation above ~200 °C due to precipitate dissolution and microstructural coarsening, creating a significant gap in high-temperature alloy design. In this work, Al-Ce alloys are proposed as a promising alternative due to the in situ formation of the stable $Al_{11}Ce_3$ intermetallic phase in these alloys. This phase is incoherent with the Al matrix, enabling Orowan looping as a strengthening mechanism while suppressing precipitate and grain coarsening because of the negligible solubility and diffusivity of Ce in Al. As a result, Al-Ce alloys retain mechanical integrity at elevated temperatures without requiring post-solidification heat treatment.

While Al-Sc alloys are known for superior properties, their high cost and limited availability constrain widespread use. Cerium, by contrast, is an abundant and low-cost by-product of the extraction and purification of Nd, Pr, Dy and Tb. This dissertation explores compositional optimization and thermomechanical processing of Al-Ce alloys to enhance both room-temperature and high-temperature performance. For example, extrusion of as-cast Al-10Ce and Al-10Ce-4Mg alloys increased their yield strengths from 62.3 MPa and 176 MPa to 94 MPa and 200 MPa, respectively, due to microstructural refinement. Building on these results, a new multicomponent alloy, Al-10Ce-4Mg-xCu-yZr, was designed, processed, and characterized. This alloy system exhibits high property retention at both ambient and high temperatures. These findings demonstrate that systematic compositional tuning and process design can produce lightweight Al-Ce alloys with high strength retention up to 300 °C, addressing a critical limitation of current commercial alloys and highlighting their potential for next-generation aerospace and automotive application.

Keywords: Al-Ce alloy; Mechanical Properties; Microstructure; high temperature stability; yield strength; strengthening mechanism.

CHAPTER 1: INTRODUCTION

1.1 Aluminum and its Alloys

1.1.1 Basic properties of Al

Aluminium is the most abundant metallic element in the Earth's crust, accounting for roughly 8.3% by weight. Its electronic configuration ($3s^2 3p^1$) provides three valence electrons available for metallic bonding, which underpins its relatively high elastic modulus (~70 GPa) and melting point (660 °C) compared to the alkaline earth metals. As a Group 13 element, Al combines metallic bonding with partial covalent character, giving rise to its hallmark attributes: low density (2.70 g/cm^3), high ductility, and excellent thermal and electrical conductivity. The early extraction of Al in the mid-19th century relied on the reduction of $AlCl_3$ with alkali metals such as sodium or potassium. This approach was inefficient and costly, restricting availability. Major technological advances between 1886 and 1888 transformed Al into a widely available engineering material. These include:

(1) The Hall-Héroult electrolytic process enabled large-scale reduction of alumina (Al_2O_3) to Al metal
(2) The Bayer process provided a cost-effective route to refine Al_2O_3 from bauxite ore, and
(3) Advances in electric power generation lowered the cost of electrolysis.

Aluminium solidifies in a face-centered cubic (FCC) crystal structure. Its low critical resolved shear stress (~1 MPa) on the {111}〈110〉 slip system means that high-purity single crystals yield at very low stresses (~2 MPa). The stacking-fault energy (≈150 mJ/m^2) of Al is relatively high, producing narrow stacking-fault ribbons only a few atomic spacings wide. These faults are thermally unstable and collapse easily, facilitating cross-slip of dislocations and contributing to the high ductility of the metal. To enhance the thermal stability of Al for structural applications, strategic alloying with elements such as Cu, Mg, Sc, and Ce becomes essential, as these additions modify microstructural evolution and retard high-temperature degradation.

1.1.2 Al Alloys for elevated temperature

Pure Al has limited structural applications due to its low intrinsic strength. To overcome this limitation, alloying additions such as Cu, Mg, Mn, Si, Sn, Ni, and Zn are commonly introduced to form solid solutions and/or precipitate-strengthened Al alloys. Since the early 20th century, a wide variety of Al alloys have been developed, tailored for their low density, high specific strength, good castability, and excellent corrosion resistance [1]. Today, Al alloys are the most widely used structural metals after steel, with critical applications in the aerospace and automotive industries.

Most commercial Al alloys are designed for room-temperature use, with an upper service temperature of approximately 150 °C. Above this threshold, their strength rapidly deteriorates due to precipitate coarsening and dissolution. For instance, the widely used Al-Mg 6061 alloy exhibits an ultimate tensile strength (UTS) of ~300 MPa at room temperature, but its strength decreases to ~100 MPa at 300 °C. Despite their lightweight nature and superior corrosion resistance, this temperature sensitivity has limited the broader use of Al alloys in high-temperature environments.

Currently, Ti alloys dominate the ~300 °C temperature regime owing to their high specific strength. However, Al alloys remain attractive alternatives because they are lighter and more cost effective. The commercially available high-temperature Al alloys include the Al-Cu (2618 series) and Al-Zn-Mg-Cu (7085 series) systems. At 100 °C, the 2618 and 7085 alloys achieve UTS values of ~380 MPa and ~430 MPa, representing ~20% and ~30% improvements, respectively, compared to 6061 [27, 28, 29]. Nonetheless, their mechanical properties degrade severely above 150 °C due to the dissolution of strengthening precipitates, restricting their practical use at elevated temperatures.

Consequently, there is strong interest in developing new alloy systems capable of maintaining strength at ~300 °C. Promising candidates include Al-Sc alloys and Al-Ce alloys, both of which form highly stable intermediate dispersoids that resist coarsening. These microstructural features provide pathways for enhancing thermal stability and extending the application of Al alloys in high-temperature automotive and aerospace environments. Figure 1.1 below illustrates high-temperature tensile strength comparisons for commercial Al alloys 7085, 2618, and 6061.

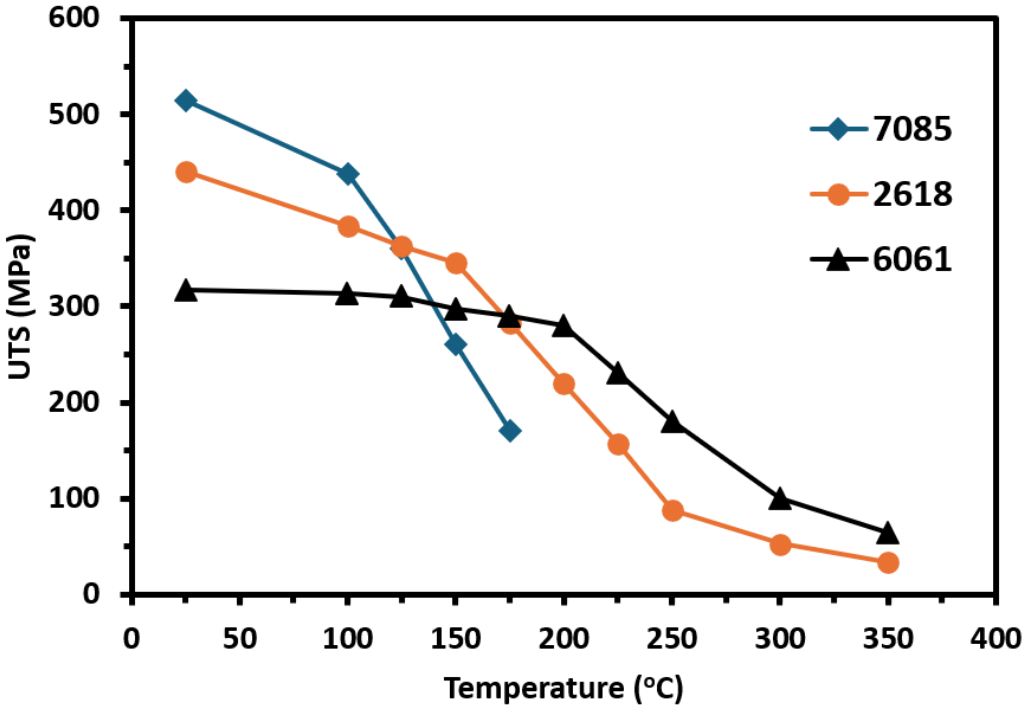

Figure 1.1 Temperature dependence of the strength of 7085, 2618, and 6061 commercial Al alloys

1.1.3 Al-Mg alloys

Being among the most widely used wrought Al alloys, Al-Mg-Si alloys (notably the 6xxx series) are valued for their well-balanced combination of mechanical properties, excellent workability, good machinability, and high corrosion resistance. A representative alloy, 6061 in the T6 temper, achieves a tensile strength of approximately 300 MPa, which is sufficient for structural applications while retaining good machinability. In addition, 6061 exhibits good ductility and toughness, with a room-temperature elongation of about 8–10%, enabling the alloy to be readily formed by bending, rolling, or extrusion into a wide range of engineering components.

Mg additions strengthen Al primarily through solid-solution hardening, enhancing room-temperature strength. However, at elevated temperatures (~300 °C), Mg gradually dissolves into the Al matrix, causing strength reduction. The incorporation of thermally stable elements such as Ce and Zr mitigates this degradation, improving strength retention. In binary Al–Mg alloys, Mg exhibits limited solubility and forms coherent β′ precipitates below 200 °C, which remain stable due to slow diffusion kinetics. Upon extended annealing near 200 °C, these transform toward equilibrium Al_3Mg_2, but at room temperature, strengthening

is dominated by Mg atoms in solid solution that impede dislocation motion and enhance overall hardness.

A defining characteristic of Al-Mg alloys is their tendency to undergo discontinuous plastic flow, manifested as serrated stress-strain curves. This instability is attributed to dynamic strain aging (DSA), the microscopic origin of the macroscopic Portevin-Le Chatelier (PLC) effect. At the atomic scale, DSA arises from the interaction between mobile dislocations and solute Mg atoms. Solute clustering around dislocation strain fields enhances the effective lattice resistance, producing repeated cycles of pinning and unpinning. This intermittent resistance to dislocation glide gives rise to the observed serrations and negative strain-rate sensitivity in specific ranges of temperature and strain rate

The occurrence of DSA is strongly temperature- and strain-rate dependent. Within a specific domain (−80 °C to ~110 °C at strain rates below 10^{-1} s^{-1} in AA5182-O), the strain rate sensitivity (SRS) becomes negative, favoring localization of plastic strain into PLC bands [22]. At lower or higher temperatures, solute mobility is either too sluggish or too rapid to sustain clustering during dislocation arrest times, and deformation becomes smooth. Importantly, the clustering mechanism is now understood to occur predominantly at forest dislocations, where residence times are long enough to allow diffusion-mediated binding, rather than on mobile dislocations.

Despite negative SRS, Al-Mg alloys remain among the most ductile Al alloys, owing to their high work-hardening capacity. Ductility exhibits a characteristic “U-shaped” dependence on temperature: it decreases from cryogenic conditions to room temperature (where serrations are most pronounced), then increases again at elevated temperatures as solute mobility reduces clustering and DSA weakens. Thus, the interplay of solid solution strengthening, β′/Al_3Mg_2 precipitation, and solute-dislocation interactions define both the high ductility and the characteristic serrated flow behavior of Al-Mg alloys.

1.1.4 Al-Zr Alloys

Zr enhances the strength and thermal stability of Al alloys primarily through the precipitation of coherent, ordered Al_3Zr ($L1_2$) dispersoids during controlled solidification or aging. These nanoscale precipitates form uniformly within the Al matrix and generate coherency strain fields that effectively impede dislocation motion, producing significant precipitation strengthening [4,8]. Due to the minimal lattice mismatch (~1%) between Al and

Al_3Zr, these particles remain coherent and resist coarsening even after prolonged thermal exposure [26]. Additionally, Al_3Zr dispersoids exert a strong Zener pinning effect on grain boundaries, suppressing recrystallization and grain growth during high-temperature deformation or annealing [8]. The low diffusivity of Zr in Al further stabilizes the dispersoid distribution, enabling sustained microstructural integrity and mechanical strength at temperatures exceeding 400 °C [26, 31]. Consequently, Zr serves as a potent microalloying addition for developing thermally stable, high-strength Al alloys suitable for elevated-temperature structural and electrical applications.

1.1.5 Al-Cu Alloys

The discussion of Al-Cu alloys is relevant here because they represent the archetype of precipitation-hardened Al-alloys, providing a critical foundation for understanding and comparing strengthening mechanisms in Al-Ce-based alloys. While Al-Cu alloys achieve exceptional strength through coherent and semi-coherent precipitates (GP zones, θ″, θ′), these phases are metastable and prone to coarsening or dissolution above ~200 °C, leading to rapid loss of strength. In contrast, Al-Ce alloys rely on the in-situ formation of the thermodynamically stable, incoherent $Al_{11}Ce_3$ phase, which resists coarsening even after prolonged thermal exposure. Therefore, studying Al-Cu alloys establishes a reference framework for how microstructural stability governs high-temperature mechanical performance and highlights the advantages of Al-Ce systems for applications requiring strength retention beyond 300 °C.

1.5.1 Strengthening Mechanism

Copper strengthens Al primarily through precipitation hardening (age hardening) and limited solid-solution strengthening. The mechanism depends on temperature and alloy condition:

1. Solid-Solution Strengthening (in the solution-treated state):
   When Cu atoms dissolve in the Al lattice, they create local lattice distortions due to atomic size and modulus mismatch. These distortions impede dislocation motion, increasing strength modestly. However, the solid solubility of Cu in Al is limited (~5.7 wt% at 548 °C, near zero at room temperature), so this effect is temporary—mainly before precipitation begins.

2. Precipitation (age) Hardening (dominant mechanism):
   Upon quenching and aging, supersaturated Cu atoms precipitate sequentially as GP zones → θ″ → θ′ → θ (Al_2Cu).

   (i) GP zones (fully coherent): Create strong elastic strain fields that pin dislocations.
   (ii) θ″ (coherent): Increase lattice strain and strengthen further.
   (iii) θ′ (semi-coherent): Provide high resistance to dislocation motion through shearing and Orowan looping.
   (iv) θ (Al_2Cu, incoherent): Represents the overaged condition, where coarsened particles reduce strength.

Thus, the primary strengthening mechanism of Cu in Al is precipitation hardening, where finely dispersed coherent and semi-coherent Cu-rich phases hinder dislocation motion, providing high yield and tensile strength at room temperature but limited thermal stability above ~200 °C.

1.1.6 Al-Sc Alloys

To overcome these limitations, Sc has been extensively studied as a potent alloying element for high temperature strengthening. In binary Al-Sc systems, Sc forms thermodynamically stable Al_3Sc precipitates that adopt an $L1_2$ structure. With a lattice mismatch of only 1.34% relative to Al at room temperature [2], these precipitates remain coherent even at relatively large sizes and resist coarsening up to ~350 °C. Reports by Blake and Hopkin [3] and Hyde et al. [4] demonstrate that primary Al_3Sc particles form readily in hypereutectic compositions, acting as heterogeneous nucleation sites that refine grain size. Pan et al studied the effect of Sc and Zr on the microstructure of Al-5Mg alloy. The results indicated that 0.6wt.% Sc decreased the average grain size of as-cast Al-5Mg from 265.1μm to 50.3μm [33]. Grain refinement and stabilization directly promote grain-boundary strengthening, while Al_3Sc precipitates also hinder recrystallization via Zener drag [5,6].

Multicomponent systems represent an advanced stage in alloy design where synergistic interactions between multiple alloying elements are deliberately utilized to overcome the intrinsic limitations of binary systems. In Al alloys, such compositional complexity enables the simultaneous optimization of strength, ductility, and thermal stability – a balance that is often unattainable through single-element additions. Within these systems,

Sc plays a pivotal role due to its strong interactions with other solute elements. Jiang et al. [7] demonstrated that in Al-Cu alloys, Sc segregation at Al/θ′ interfaces reduces interfacial energy and slows θ′ precipitate growth kinetics, thereby enhancing microstructural stability during aging. In Al-Mg-Sc alloys, magnesium accelerates Al_3Sc precipitation and decreases lattice mismatch with the Al matrix, preserving precipitate coherency to larger sizes and suppressing discontinuous precipitation [8,9]. Furthermore, Zr additions to Al-Sc systems increase the number density of nanoscale precipitates and refine their size distribution. The resulting core–shell $Al_3(Sc,Zr)$ precipitates, characterized by Sc-rich cores and Zr-rich shells, markedly retard coarsening and inhibit recrystallization, leading to enhanced high-temperature strength and structural stability.

1.1.7 Al-Ce Alloys

Aluminium alloys remain critical in the transportation sector due to their high specific strength and castability. However, their performance is limited at elevated temperatures. Above 150 °C, most commercial Al alloys exhibit a marked decline in ultimate tensile strength (UTS) and yield stress, and by ~300 °C they typically retain only ~30% of their load-carrying capacity [15]. Current alloy design strategies aim to overcome these limitations by stabilizing strength through thermally resistant, incoherent dispersoids. Notable examples include Al-Fe-V and Al-Fe-Mo-V alloys, which maintain ~50% of their room-temperature strength at high temperatures. Nevertheless, these systems suffer from limited toughness and exhibit pronounced sensitivity of UTS to temperature fluctuations, constraining their widespread application.

Despite these outstanding attributes, the prohibitive cost and limited availability of Sc curtail the widespread adoption of Al-Sc alloys. Cerium (Ce), by contrast, offers a cost-effective and sustainable alternative. As a low-value by-product of Nd/Pr production, Ce provides an abundant supply chain advantage [10,11]. While Al-Sc alloys can achieve higher peak strengths, Al-Ce alloys deliver superior economic viability and impressive high-temperature stability. Their performance derives from the in-situ formation of the stable $Al_{11}Ce_3$ intermetallic during solidification. Unlike metastable precipitate-strengthened alloys prone to over-aging, Al-Ce systems resist coarsening due to negligible Ce solubility in Al and the extremely low diffusivity of Ce atoms even at elevated temperature (~300°C). Consequently, their microstructures retain mechanical resilience under prolonged exposure to elevated temperatures [12,13].

In Al alloys the addition of Ce enhances strength primarily through the formation of the thermodynamically stable intermetallic phase $Al_{11}Ce_3$. These intermetallics exhibit high thermal stability and a melting point (congruent melting temperature of 1253 °C) exceeding 300 °C, rendering Al-Ce alloys particularly attractive for higher temperature applications. Early powder metallurgy studies in the 1980s demonstrated that alloys containing as little as 4 wt.% Ce displayed high-temperature mechanical properties (low Ce/high Mg Al alloy showed 120% yield retention after 1000 hours aging, which was higher than high Ce/low Mg Al alloy, which showed 90% yield retention after 100 hours aging) superior to those of the best commercial Al castings available at the time [24]. From an economic standpoint, Ce is especially appealing since Ce oxide is abundantly produced as a by-product during the extraction of higher-value rare earths such as Nd and Pr and is often discarded.

More recent investigations, including those of Weiss (2019), have shown that Al-Ce alloys fabricated via casting, extrusion, and additive manufacturing retain their mechanical properties at elevated temperatures approaching 500 °C, consistent with earlier findings by Sims et al. (2017) [10,24]. Additionally, Gröbner et al. (2004) examined Al alloys with up to 25 at.% Ce and 45 at.% Si, reporting that Ce additions in the range of 1-5 at.% acted as potent grain refiners. These additions also lowered the liquidus and growth temperature of Si, further demonstrating the promise of Ce as a functional alloying element [25]. The continued development of Al-Ce casting alloys is driven by two primary motivations. First, there is a growing demand for Al alloys capable of retaining mechanical performance at elevated temperatures. Second, the availability of excess Ce – produced as a by-product during the production of high-value critical rare earths such as Nd, Dy, Tb, and Sm – provides a compelling economic rationale for its utilization as an alloying addition.

Cerium strengthens Al-Ce alloy via precipitation strengthening due to its extremely low solubility in Al. Multiple intermetallics form in the Al-Ce alloy system due to the significant size, and electrical negativity difference between the two elements. The most sought intermetallic compound for Al-Ce is $Al_{11}Ce_3$. The $Al_{11}Ce_3$ intermetallic phase is remarkably stable at elevated temperatures (~300 °C) and exhibits strong resistance to coarsening under thermal exposure. Its incoherence with the Al matrix imposes a substantial barrier to dislocation motion, forcing bypass through Orowan looping rather than shearing. This mechanism increases the effective lattice resistance, thereby enhancing the strength and

creep resistance of the alloy while maintaining microstructural stability. The eutectic composition between Al and $Al_{11}Ce_3$ is at 10wt% Ce at 621ºC.

Depending on the alloy composition, the alloy's mechanical properties can vary differently. When the Cu:Ce ratio is approximately 2:1, Cu interacts with Al and Ce to form stable Al-Ce-Cu intermetallic phases that contribute significantly to precipitation strengthening [20]. Belov et al. reported an invariant quasi-binary eutectic reaction L→(Al) + Al_8CeCu_4 (610ºC, 14 wt.% Cu and 7wt.% Ce), in ternary Al-Ce-Cu alloys. The resulting eutectic exhibited a refined microstructure that remained resistant to coarsening, even after fragmentation and spheroidization during thermal exposure. Notably, the average particle size did not exceed 2 μm after annealing at 590 °C [21]. Rapid solidification of such alloys further refines the microstructure to the nanocrystalline scale, thereby enhancing strength and thermal stability and enabling unique combinations of mechanical performance.

The room-temperature ultimate tensile strength (UTS) of as-cast Al–Ce alloys typically ranges from 72 to 163 MPa, with elongation values between 1.4 % and 15.4 % [14, 24, 32]. To further enhance strength while maintaining adequate ductility, additional alloying elements such as Mg and Zr have been investigated. Magnesium contributes primarily through solid-solution strengthening, increasing the matrix lattice resistance to dislocation motion. For instance, the addition of 0.4 wt.% Mg to as-cast Al–12Ce raises the UTS to ~200 MPa, representing an ~18 % improvement, with ductility of approximately 6 %. Zirconium, on the other hand, promotes precipitation strengthening via the formation of coherent, thermally stable Al_3Zr dispersoids, which inhibit dislocation motion and suppress recrystallization, thereby enhancing both high-temperature strength and microstructural stability [26].

In addition to the compositions, the processing routes also play a significant role in the properties of Al-Ce based alloys. The grain size and precipitate size are strongly depended on the cooling rates, the recrystallization, grain growth, and residual stress are heavily reliant on how the alloys are being processed. More recently, Zhonghua et al. (2022) studied the microstructural evolution and microhardness of rapidly solidified Al-8Ce (hypoeutectic) and Al-20Ce (hypereutectic) alloys. Their findings indicated that rapid solidification did not markedly alter the phase constituents in either composition, and no age-hardening response was observed in melt-spun ribbons. The as-spun microstructures exhibited thermal stability during annealing below 300 °C; however, above this threshold,

stability deteriorated rapidly, resulting in microstructural coarsening and a corresponding decline in hardness [16]. These observations reveal that while Al-Ce alloys offer intrinsic stability advantages relative to conventional precipitation-hardened systems, their high-temperature performance still depends critically on processing route and service conditions.

Experimental studies underscore the benefits of thermomechanical processing in Al-Ce alloys. Extruded binary Al-Ce alloys achieve ultimate tensile strengths (UTS) near 400 MPa and yield strengths (YS) up to 320 MPa, enabled by refined eutectic morphologies [14]. Even without deformation processing, hot isostatic pressing (HIP) yields robust performance (UTS ≈ 280 MPa, YS ≈ 220 MPa), demonstrating the intrinsic strength of solidification-derived microstructures [10]. The eutectic reaction in Al-Ce occurs at ~10.6 wt.% Ce and 621 °C, forming a fine lamellar network of α-Al and $Al_{11}Ce_3$ [15]. Although solid solution strengthening is negligible due to Ce's minimal solubility in Al, the introduction of minor alloying additions such as Mg, Si, or Cu enables further refinement of the eutectic structure and introduces additional hardening pathways. For example, alloying Al-12Ce with 4 wt.% Si and 0.4 wt.% Mg increases the yield strength from ~57 MPa to ~75 MPa, albeit with some reduction in ductility.

Inoue et. al studied the microstructures and thermal stability of glass forming ability of chill-block melt spun alloys composed of Al matrix and rare earths [17]. He found out that crystalline α-Al solid solutions formed below 7-9 at% Ce replaced an amorphous phase with up to 10-17at% Ce. Jones et.al focused on Al-Ce additions below the amorphous phase, with a particular attention to microstructure selection, growth temperature, and thermal stability of Al-Ce alloy under rapid solidification [18]. Currently, the strengthening methods of industrial casting Al alloys are mainly solution strengthening by adding elements and age strengthening by heat treatment. These strengthening methods will improve the strength and stiffness of the alloy and reduce thermal expansion rate. However, under long-term high temperatures, the microstructure of the second phase and the strengthening phase of Al alloys will undergo drastic changes, which will reduce their mechanical properties [19].

1.7.1 Al-Ce versus Al-Sc

A comparison of basic physical properties between Al-Ce and Al-Sc alloys are listed in Table 1. In comparison, the contrast in strengthening mechanisms highlights their suitability for distinct application regimes. Al-Sc alloys achieve exceptional strength through

the precipitation of coherent, ordered Al_3Sc phases, which form during solution treatment and aging within the FCC Al matrix. The near-lattice match between Al_3Sc and Al imparts coherency strains that act as strong barriers to dislocation motion, enabling pronounced precipitation hardening and excellent strength retention at ambient and intermediate temperatures [4,8]. At peak aging, Al-Sc alloys exhibit ultimate tensile strengths in the range of 550-600 MPa with good ductility, making them attractive for aerospace and defense applications. This mechanism, however, is metastable; beyond ~300 °C, Al_3Sc precipitates undergo coarsening and lose coherency, leading to a rapid degradation in mechanical performance.

By contrast, Al-Ce alloys are strengthened through the in-situ formation of thermodynamically stable $Al_{11}Ce_3$ intermetallic dispersoids during solidification. Despite their incoherency with the matrix, these intermetallics act as rigid, load-bearing phases that obstruct dislocation motion via Orowan looping while simultaneously refining the eutectic microstructure into thermally stable lamellar morphologies [10, 24]. The extremely low solid solubility and diffusivity of Ce in Al suppress Ostwald ripening, ensuring dimensional stability of the dispersoids under long-term thermal exposure. As a result, Al-Ce alloys retain more than 70% of their hardness after extended aging at 300-350 °C and maintain mechanical stability up to 500 °C. Extruded Al-Ce alloys achieve tensile strengths of ~380-400 MPa with yield strengths near 320 MPa, while hot isostatically pressed variants demonstrate ~280 MPa UTS and ~220 MPa YS [10, 24]. Thus, while Al-Sc alloys remain unrivalled for applications requiring maximum strength and ductility at room and intermediate temperatures, Al-Ce alloys provide a cost-effective and thermally robust alternative for sustained high-temperature service, particularly in transportation and energy sectors where performance retention at ≥300 °C is essential.

$Al_{11}Ce_3$ precipitates are incoherent with the Al matrix and therefore do not impart coherency strain hardening as observed in Al-Sc alloys. Instead, they contribute to strengthening by acting as rigid, thermodynamically stable dispersoids that obstruct dislocation motion through Orowan looping and load transfer. Their remarkable stability is attributed to the extremely low solubility and diffusivity of Ce in Al, which suppresses coarsening and ensures retention of mechanical properties during prolonged thermal exposure up to ~500 °C. A trade-off of this mechanism is reduced ductility, arising from the brittle nature of the intermetallic phase, although this limitation can be partially alleviated through

compositional tuning with elements such as Mg or Cu. Taken together, the incoherency of $Al_{11}Ce_3$ makes Al-Ce alloys less reliant on metastable precipitation and uniquely suited for long-term high-temperature applications

Table 1.1.0 A Comparison of Al-Ce and Al-Sc Alloy

Feature	**Al-Ce Alloys**	**Al-Sc Alloys**
Strengthening phase	$Al_{11}Ce_3$ (incoherent, thermodynamically stable intermetallic). As-Cast Al-4Ce has a room temperature yield strength of ~29.9 MPa[14].	Al_3Sc (coherent, $L1_2$-ordered precipitate). As-cast Al-8Sc has a room temperature yield strength of ~75MPa [30].
Formation	Forms directly during solidification (eutectic Al + $Al_{11}Ce_3$); no heat treatment required	Requires solution treatment and aging to form nanoscale coherent precipitates
Strengthening mechanism	Dispersion strengthening and load transfer from rigid, stable particles; Orowan looping	Precipitation hardening via coherency strain fields that strongly resist dislocations
Thermal stability	High: stable up to ~500 °C due to low Ce diffusivity in Al	Limited: stable only up to ~300 °C, after which precipitates lose coherency and coarsen
Microstructure	Fine eutectic lamellae (Al + $Al_{11}Ce_3$), refined by rapid solidification or extrusion (as-cast size is ~0.6-1 μm)	Uniform nanoscale precipitates in Al matrix; microstructure sensitive to processing (as-cast size is ~10 to 30nm).
Strength retention	Retains >70% hardness at 300-350 °C, stable under long exposures	High strength at room and intermediate temperatures, but drops sharply above 300 °C

Table 1.1.0 Continued

Feature	**Al-Ce Alloys**	**Al-Sc Alloys**
Ductility / toughness	Lower (due to brittle intermetallic); can be improved with Mg or Cu additions. As-cast Al-4Ce has a ductility of 15.4% [14].	Generally better ductility because precipitates are coherent and non-brittle. As-cast Al-4Sc has a ductility of 10 % [30].
Economics	Ce is abundant, low-cost, a by-product of rare-earth mining	Sc is scarce and expensive, limiting large-scale adoption

1.1.8 Problem formulation and approach

This research was designed around three overarching objectives:

1. To develop Al-Ce-X alloys with enhanced tensile strength at both ambient and elevated temperatures (~300 °C). The targeted mechanical performance included a room-temperature yield strength exceeding 350 MPa, with strength retention (~300MPa yield strength) after 100 h exposure at 300 °C aging, and an ultimate tensile strength (UTS) above 100 MPa at 350 °C.
2. To provide the first comprehensive datasets on the fracture and fatigue behavior of Al–Ce alloys, establishing a foundation for their structural design and life-prediction modeling.

In pursuing these objectives, four central research questions guided this research:

1. How can we optimize processing procedure to improve mechanical properties of Al-Ce alloys especially high temperature stability?
2. What is the primary strengthening mechanism that enhances mechanical strength at high temperature for Al-Ce alloys?
3. What is the correlation between grain size and mechanical property?
4. How can we increase the yield strength without compromising ductility?

Research Context and Approach

Conventional Al alloys are widely appreciated for their castability and corrosion resistance; however, their mechanical integrity deteriorates above approximately 150 °C due to precipitate dissolution and coarsening, leading to a rapid loss in strength and ductility. To overcome this limitation, the present work employed two synergistic strategies: (i) processing design to control solidification kinetics and microstructural refinement, and (ii) strategic alloying of Al-Ce with Mg, Zr, and Cu combined with thermomechanical heat treatments.

Processing governs cooling rate and, consequently, grain refinement and phase distribution. Rapid solidification promotes metastable, fine-scale microstructures that suppress diffusion and enhance strength in accordance with the Hall-Petch relationship. The focus of this research is on understanding the formation of the precipitates capable of retaining their morphology and strengthening effect at elevated temperature, resisting coarsening even under prolonged thermal exposure.

Magnesium contributes to solid-solution strengthening in Al-Ce alloys but gradually dissolves during long-term exposure at high temperature. In contrast, the $Al_{11}Ce_3$ intermetallic dispersoids exhibit remarkable thermal stability, maintaining strength through their resistance to coarsening. The addition of Zr further improves stability by forming Al_3Zr dispersoids that encapsulate the $Al_{11}Ce_3$ particles, generating core-shell structures (Ce-rich core, Zr-rich shell). These complex dispersoids suppress grain boundary migration and inhibit phase coarsening. Moreover, the incorporation of Zr promotes the formation of $Al_3(Ce_{1-x}Zr_x)$ phases, which exhibit enhanced coarsening resistance and higher recrystallization temperature. The Cu-Zr master alloy facilitates Zr incorporation through the formation of eutectic phases that improve solubility and dispersion within the Al matrix.

The combined effects of compositional tuning and processing control determine the fraction, morphology, and spatial distribution of strengthening phases, which in turn govern the mechanical performance and thermal stability of Al-Ce alloys. Thus, the four guiding questions are addressed holistically within the framework of processing design, alloy chemistry, and thermomechanical optimization.

1.1.9 Dissertation organization

This dissertation is organized in an alternate format, with the following four chapters prepared in the form of papers that have been or will be submitted for publication. The current chapter provides a general introduction of the subject, review of the existing literatures and identifies the research problem with planned approaches. The conclusion chapter summarizes the entire work and provides suggestions for future work.

CHAPTER 1 – INTRODUCTION

Background, motivation and problem statement.

CHAPTER 2 – EFFECT OF THERMOMECHANICAL PROCESSING ON MECHANICAL PROPERTIES AND THE MICROSTRUCTURE OF BINARY AL-CE ALLOY

This paper develops temperature-resistant Al–Ce alloys and evaluates cast Al–4Ce, Al-10Ce, Al-16Ce, and extruded Al–10Ce. Extrusion at 300 °C refines Al(fcc) grains (~582 μm → ~2–3 μm) and fragments $Al_{11}Ce_3$, doubling strength (UTS ≈ 228 MPa) and raising ductility (>20%). Properties are exceptionally stable after 300 °C/100 h aging: strength retention > 99% and fracture toughness ≈ 55.4 kJ m^{-2} with ~97.6% retention. Elevated-temperature testing shows Al-10Ce outperforms AA2618 at 300 °C and retains far more of its room-temperature strength. Results link processing-induced refinement, texture, and stable $Al_{11}Ce_3$ dispersoids to sustained high-temperature performance.

CHAPTER 3 – EFFECT OF THERMOMECHANICAL PROCESSING ON MECHANICAL PROPERTIES AND THE MICROSTRUCTURE OF TERNARY AL-CE-MG ALLOY

This paper investigates microstructural refinement, mechanical performance, and fracture resistance of extruded Al-10Ce-4Mgalloys. Extrusion increases tensile strength to ~390 MPa and ductility to ~15%. After 300 °C/100 h exposure, the alloy retains ~86% of its strength. Fracture toughness remains high, decreasing minimally from ~23 kJ/m^2 to ~22.5 kJ/m^2 (~97.6% retention), with stable fatigue response. These results outperform AA2618, demonstrating Al–Ce–Mg alloys as strong candidates for high-temperature aerospace applications.

CHAPTER 4 – MECHANICAL PROPERTIES AND MICROSTRUCTURE OF AL-CE-MG ALLOY PROCESSED BY ROLLING

Hot rolling of Al-10Ce-4Mg alloy produced a refined microstructure with improved strength and ductility. The rolled alloy achieved 260 MPa tensile strength, nearly double the as-cast value, and retained 81 % strength after 100 h at 300 °C. Stable $Al_{11}Ce_3$ dispersoids and Mg solid-solution strengthening ensured excellent thermal stability and high-temperature performance.

CHAPTER 5 – STRUCTURE AND PROPERTY RELATIONS OF A RAPIDLY SOLIDIFIED AL-CE-XY ALLOY

Rapid solidification of Al-7Ce-14Cu-0.5Zr alloy produced a refined microstructure with submicron α-Al grains and uniformly distributed $Al_{11}Ce_3$ intermetallics. The melt-spun ribbon achieved ~244 HV, double the as-cast hardness, and retained 77% after 100 h at 350 °C, confirming outstanding thermal stability and demonstrating rapid solidification as an effective strengthening route.

CHAPTER 6 – CONCLUSION

Summary of the entire work and recommendations for future work.

1.2 References

[1] Mondol S, Alam T, Banerjee R, Kumar S, Chattopadhyay K. Development of a high temperature high strength Al alloy by addition of small amounts of Sc and Mg to 2219 alloy. Materials Science and Engineering: A. 2017 Feb 27;687:221-31.

[2] Harada Y, Dunand DC. Thermal expansion of al3sc and al3 (sc0. 75x0. 25). Scripta Materialia. 2003 Feb 1;48(3):219-22.

[3] Blake N, Hopkins MA. Constitution and age hardening of Al-Sc alloys. Journal of Materials Science. 1985 Aug;20(8):2861-7.

[4] Hyde KB, Norman AF, Prangnell PB. The effect of cooling rate on the morphology of primary Al3Sc intermetallic particles in Al-Sc alloys. Acta Materialia. 2001 May 8;49(8):1327-37.

[5] Norman AF, Prangnell PB, McEwen RS. The solidification behaviour of dilute aluminium-Sc alloys. Acta materialia. 1998 Oct 9;46(16):5715-32.

[6] Mukhopadhyay AK, Kumar A, Raveendra S, Samajdar I. Development of grain structure during superplastic deformation of an Al-Zn-Mg-Cu-Zr alloy containing Sc. Scripta Materialia. 2011 Mar 1;64(5):386-9.

[7] Jiang L, Li JK, Cheng PM, Liu G, Wang RH, Chen BA, Zhang JY, Sun J, Yang MX, Yang G. Microalloying ultrafine grained Al alloys with enhanced ductility. Scientific reports. 2014 Jan 8;4(1):3605.

[8] Marquis EA, Seidman DN, Asta M, Woodward C, Ozoliņš V. Mg Segregation at A l/A l 3 S c Heterophase Interfaces on an Atomic Scale:<? format?> Experiments and Computations. Physical review letters. 2003 Jul 18;91(3):036101.

[9] Mondol S, Alam T, Banerjee R, Kumar S, Chattopadhyay K. Development of a high temperature high strength Al alloy by addition of small amounts of Sc and Mg to 2219 alloy. Materials Science and Engineering: A. 2017 Feb 27;687:221-31.

[10] Sims ZC, Rios OR, Weiss D, Turchi PE, Perron A, Lee JR, Li TT, Hammons JA, Bagge-Hansen M, Willey TM, An K. High performance Al-cerium alloys for high-temperature applications. Materials Horizons. 2017;4(6):1070-8.

[11] Yang Y, Bahl S, Sisco K, Lance M, Shin D, Shyam A, Plotkowski A, Dehoff RR. Primary solidification of ternary compounds in Al-rich Al-Ce-Mn alloys. Journal of Alloys and Compounds. 2020 Dec 5;844:156048.

[12] Meyers MA, Chawla KK. Mechanical behavior of materials. Cambridge university press; 2008 Nov 6.

[13] Plotkowski A, Rios O, Sridharan N, Sims Z, Unocic K, Ott RT, Dehoff RR, Babu SS. Evaluation of an Al-Ce alloy for laser additive manufacturing. Acta Materialia. 2017 Mar 1;126:507-19.

[14] Singh G, Odhiambo HW, Tasneem MH, Ouyang G, Soare MA, Cui J, Napolitano RE, Picu CR. Effect of thermomechanical processing on mechanical properties and the

microstructure of binary Al-Ce alloy. Materials Science and Engineering: A. 2024 Nov 1;916:147395.

[15] Czerwinski F. Thermal stability of Al alloys. Materials. 2020 Aug 4;13(15):3441.

[16] Zhang Z, Bian X, Wang Y. Microstructural characterization and microhardness of rapidly solidified Al-Cealloys. International Journal of Materials Research. 2022 Jan 3;93(6):578-84.

[17] Inoue A, Ohtera K, Masumoto T. New amorphous Al-Y, Al-La and Al-Ce alloys prepared by melt spinning. Japanese journal of applied physics. 1988 May 1;27(5A):L736.

[18] Juarez-Hernandez A, Jones H. Growth temperatures and microstructure selection during Bridgman solidification of hypereutectic Al-La and Al-Cealloys. Journal of crystal growth. 2000 Jan 1;208(1-4):442-8.

[19] Khvan AV, Eskin DG, Starodub KF, Dinsdale AT, Wang F, Fang C, Cheverikin VV, Gorshenkov MV. New insights into solidification and phase equilibria in the Al-Al3Zr system: Theoretical and experimental investigations. Journal of Alloys and Compounds. 2018 Apr 30;743:626-38.

[20] Wang Y, Hou F, Fu Z, Mao H, Xu H. Microstructure and mechanical properties of novel heat-resistant Al-12Ce-xCu-yMg alloy under laser melting. Journal of Alloys and Compounds. 2022 Nov 30;924:166359.

[21] Belov NA, Khvan AV. The ternary Al-Ce-Cu phase diagram in the Al-rich corner. Acta Materialia. 2007 Sep 1;55(16):5473-82.

[22] Picu RC, Vincze G, Ozturk F, Gracio JJ, Barlat F, Maniatty AM. Strain rate sensitivity of the commercial Al alloy AA5182-O. Materials Science and Engineering: A. 2005 Jan 15;390(1-2):334-43.

[23] Li Q, Liu X, Wang J, Xue C, Wang S. Boosting the grain refinement of commercial Al alloys by compound addition of Sc. Journal of Materials Research and Technology. 2024 Jan 1;28:1774-83.

[24] Weiss D. Improved high-temperature Al alloys containing cerium. Journal of Materials Engineering and Performance. 2019 Apr 1;28(4):1903-8.

[25] Gröbner J, Mirković D, Schmid-Fetzer R. Thermodynamic aspects of the constitution, grain refining, and solidification enthalpies of Al-Ce-Si alloys. Metallurgical and materials transactions A. 2004 Nov;35(11):3349-62.

[26] Knipling KE, Dunand DC, Seidman DN. Criteria for developing castable, creep-resistant Al-based alloys–A review. International Journal of Materials Research. 2022 Jan 11;97(3):246-65.

[27] Zang J, Dai P, Yang Y, Liu S, Huang B, Ru J, Luo X. Study on the Relationship between High Temperature Mechanical Properties and Precipitates Evolution of 7085 Al Alloy after Long Time Thermal Exposures. Metals. 2021 Sep 18;11(9):1483.

[28] Summers PT, Chen Y, Rippe CM, Allen B, Mouritz AP, Case SW, Lattimer BY. Overview of Al alloy mechanical properties during and after fires. Fire Science Reviews. 2015 Apr 29;4(1):3.

[29] Kun M, Tingting L, Ya L, Xuping S, Jianhua W. Study on strengthening and toughening mechanisms of Al alloy 2618-Ti at elevated temperature. High Temperature Materials and Processes. 2018 Jan 26;37(1):9-15.

[30] Liu S, Wang X, Zu Q, Han B, Han X, Cui C. Significantly improved particle strengthening of Al–Sc alloy by high Sc composition design and rapid solidification. Materials Science and Engineering: A. 2021 Jan 7;800:140304.

[31] Røyset J, Ryum N. Scandium in aluminium alloys. International Materials Reviews. 2005 Feb 1;50(1):19-44.

[32] Weiss D, Rios O, Sims Z, McCall S, Ott R. Casting characteristics of high cerium content Al alloys. InLight Metals 2017 2017 Feb 12 (pp. 205-211). Cham: Springer International Publishing.

[33] Pan D, Zhou S, Zhang Z, Li M, Wu Y. Effects of Sc (Zr) on the microstructure and mechanical properties of as-cast Al–Mg alloys. Materials Science and Technology. 2017 Apr;33(6):751-7.

CHAPTER 2: EFFECT OF THERMOMECHANICAL PROCESSING ON MECHANICAL PROPERTIES AND THE MICROSTRUCTURE OF BINARY AL-CE ALLOY

Gaurav Singh[1], Humphrey Wara Odhiambo[2], Mohamad Hasan Bin Tasneem[1], Gaoyuan Ouyang[2,3*], Monica A. Soare[4], Jun Cui[2,3], Ralph E. Napolitano[2], Catalin R. Picu[1*]

[1]Department of Mechanical, Aerospace and Nuclear Engineering, Rensselaer Polytechnic Institute, Troy, NY 12180

[2]Department of Materials Science & Engineering, Iowa State University, Ames, IA 50011

[3]Division of Materials Sciences and Engineering, Ames National Laboratory, Ames, IA 50011

[4]General Electric Global Research, Niskayuna, NY 12309

Corresponding Authors: Catalin R. Picu (picuc@rpi.edu) & Gaoyuan Ouyang (gaoyuan@iastate.edu)

2.1 ABSTRACT

A new generation of Al alloys based on the Al-Ce system, with microstructure and properties weakly sensitive to elevated temperatures, is being developed for applications such as thermal engine blocks and supersonic aircraft fuselage components. Cast Al-Ce binary alloys with 4, 10 and 16 wt% Ce were produced by slab casting and further processed by extrusion. Extrusion produces a highly refined microstructure resulting in a twofold increase in strength (tensile strength of 228 MPa at room temperature). We show that the Al-10Ce is highly stable (more than 99% strength retention after 300°C 100 h exposure), far superior to high temperature grade Al alloy AA2618. The extruded Al-10Ce also shows a room temperature ductility of more than 20%, with a fracture toughness of 55.42 kJ/m^2 that does not degrade after high temperature exposure (97.6% toughness retention after 300°C 100h exposure). Results from testing at different temperatures are also reported.

Keywords: Al-Ce alloy; Mechanical Properties; Microstructure; Fracture toughness; Extrusion.

2.2 Statement of Contribution

The materials presented in this chapter have been published in *Materials Science and Engineering A (MSEA)*. My specific contributions to the published work include:

1. Al-Ce alloy design and compositional optimization
2. Development of processing routes
3. Microstructural and mechanical characterization, including scanning electron microscopy (SEM), X-ray diffraction (XRD), room-temperature tensile testing, and Vickers microhardness test measurements.

2.3 Introduction

Al alloys are broadly used in subsonic aircraft design due to their high specific strength and corrosion resistance. Supersonic aircrafts are subjected to elevated temperatures due to aerodynamic friction. The temperature of critical components of the skin and fuselage increases linearly with the Mach number and reaches values of 300℃ at Mach 3 and is larger than 450℃ at Mach 4. This precludes the use of current Al alloys, such as the precipitate hardened AA2XXX and AA7XXX series, as their properties degrade rapidly above ~220℃ [1]. The main strengthening mechanism of precipitate hardening is disabled at higher temperatures due to precipitate coarsening and dissolution [2]. A current solution is to use more thermally stable but heavier alloys, e.g. Ti-based, for such applications [3].

A new generation of temperature-resistant Al alloys based on the Al-Ce system is considered as a potential solution for high temperature airframe applications [4–6], enabling replacement of selected Ti alloy components and realization of significant weight reduction that reflect in reduced energy consumption and reduced emissions. The goal of this material development effort is to obtain microstructures stable enough to retain the room temperature yield strength, tensile strength and fracture toughness [7–9] upon exposure to elevated temperatures (300℃).

Ce is the most abundant rare earth metal, currently lacking high-volume applications [10,11]. In the literature, it is described as one of the potential candidates for acting as a primary alloying element in Al alloys [12]. Within the composition range considered here (≤ 16 wt%Ce), microstructures generally involve the $Al_{11}Ce_3$ intermetallic phase within the Al (fcc) majority phase. For the purposes of achieving high strength, a uniform dispersion of fine intermetallics is desirable [17]. With Ce exhibiting vanishing solubility and very low

diffusivity in the Al (fcc) phase, precipitation strengthening through conventional diffusional aging processes is precluded. However, if fine Ce-bearing intermetallic dispersions can created through other means, these are likely to be highly stable at elevated temperatures since coarsening processes would also be very sluggish [13–16]. In this work we examine the potential for using casting and thermomechanical processing to achieve the desired microstructures and corresponding high temperature properties.

Al-Ce alloys in the near-eutectic range (5-20 wt% Ce) exhibit excellent castability and resistance to hot tearing and cracking [21–24] with off-eutectic microstructures containing the expected primary phases, typically dendritic Al (fcc) for hypoeutectic or faceted script-like or plate-shaped $Al_{11}Ce_3$ particles for hypereutectic alloys. In either case, the nonuniform spatial distribution of intermetallic does not lead to the most efficient strengthening [13–15]. Given the potential utility of Al-Ce alloys in high temperature applications, conventionally cast alloys require further processing for microstructural refinement to enable suitable performance in applications requiring high strength under prolonged exposure to elevated temperatures. Forging, rolling and extrusion, as well as severe plastic deformation (SPD) processes, such as high-pressure torsion and equi-channel angular pressing, have been used extensively to produce microstructural refinement in metallic materials [16], however, processing of Al-Ce alloys by these methods has received limited attention.

Zhang et al [26] studied the effect of heat treatment on the mechanical properties of an Al-9Ce alloy produced by casting in a heated (300℃) graphite mold followed by 85% reduction in thickness by cold rolling. Two important effects of cold rolling were identified. First, rolling of the hypoeutectoid structure resulted in flattening of the primary dendritic Al (fcc) phase, producing a laminar composite overall structure consisting of alternating layers of primary Al (fcc) and a fine two-phase eutectic constituent (Al (fcc) + $Al_{11}Ce_3$) which itself consists of fine lamella or rods of $Al_{11}Ce_3$. Enhanced ductility and toughness were attributed in part to this composite structure, where the large Al (fcc) grains provide high capacity for plastic deformation and the fine composite structure in the eutectic provides a mechanism for ductile blunting of microcracks potentially emanating from the brittle $Al_{11}Ce_3$ phase.

Second, the cold rolling process resulted in the refinement of the eutectic $Al_{11}Ce_3$ particles through mechanical fracture along with preferential alignment of the resulting particles along the rolling direction. It was asserted that this particle alignment contributes to the observed increase in strength, presumably through more efficient load transfer of the

aligned composite structure. Post-deformation heating further showed significant Al recrystallization at 300℃ and substantial grain growth at 400℃, but these changes had little effect on mechanical properties, which are largely dictated by the morphology and distribution of the hard/brittle phase. Stanislav et al. showed the effect of high-pressure torsion on the microstructure and tensile properties of Al-9Ce. The process leads to the formation of nanograins and a large increase of the yield stress and tensile strength [4,17].

While reports of investigations into the influence of extrusion processing on mechanical properties of Al-Ce alloys are limited, significant promise has been shown. Indeed, extrusion of binary Al-Ce alloys has been reported to produce ultimate/yield strengths of 400/340 MPa, competitive with high strength wrought aluminum alloys (e.g. AA2618) and with far lower extrusion ratios (i.e. 3:1 as compared with 10:1) [18]. Other reports of extrusion in Al-Ce (based) alloys are seemingly confined to processing of dilute alloys (>= 99% Al) for applications such as electrical conductors [19,20].

With clear evidence that the mechanical properties of Al-Ce alloys are largely attributable to the fraction, morphology, and spatial distribution of the intermetallic $Al_{11}Ce_3$ particles and that these can be substantially controlled through Ce content and processing (solidification, deformation, and heat treatment), the present work focuses on the thermal stability of cast Al-4Ce, Al-10Ce and Al-16Ce and extruded Al-10Ce alloy (all percentages in wt%). Microstructures are characterized using SEM, XRD, and EBSD and mechanical properties are measured at ambient and elevated temperatures by uniaxial tensile testing and fracture toughness testing. We examine microstructural refinement, thermal stability, strengthening mechanisms, and the fracture toughness of cast and extruded Al-10Ce alloys before and after heat treatment. We conclude that extrusion produces significant precipitate and grain refinement, and the microstructure is stable upon exposure to 300℃ for durations up to 100 h, with minimal reduction of mechanical properties associated with heat treatment.

2.4 Experimental

2.3.1 Materials and processing

Al-Ce ingots with 4, 10 and 16% Ce were produced by slab casting (graphite open slab mold) at casting temperature of 850ºC and a mold temperature of 400ºC. The eutectic composition Al-10Ce was selected for extrusion. 25.4 mm diameter as-cast rods were reduced to 9.5 mm diameter by extrusion at 300℃. At the onset of the experiment, the

heating rate of the extrusion furnace chamber is 10℃/min using Innovare LMS extrusion press. An equilibration at the target temperature for 30 minutes is applied before extrusion; extrusion is performed by adjusting the pressure from 11.6 ksi (80 MPa) to 81.4 ksi (561 MPa) within 5 minutes. At the end of extrusion, a fan is used to cool the extruded rod to room temperature, after which the rod is ejected.

The mechanical properties were measured in the as-cast (AC) and cast/extruded (CE) conditions and also in the corresponding heat-treated conditions (AC-10, AC-100, CE-10, CE-100), where the number indicates hours at 300ºC. In addition, the response to prolonged high temperature exposure was examined for Al-10Ce (AC-xx) by measuring hardness at room temperature after annealing at 300ºC for durations up to 400 h, as indicated by the time, "xx" in hours. Table 2.1 summarizes the tested alloys and conditions used in the present study along with the naming convention established for the remainder of this communication.

Table 2.1: Summary of the alloys and conditions utilized in the present study.

Naming Convention	**Description**
AC	As - Cast
CE	Cast and extruded
AC-10	As – Cast + 300C for 10 hours
AC-100	As – Cast + 300C for 100 hours
CE-10	Cast and extruded + 300C for 10 hours
CE-100	Cast and extruded + 300C for 100 hours

2.3.2 Tensile and fracture experiments

Tensile specimens were machined using CNC per the ASTM E8 standard [21] for all cast, extruded, and heat-treated conditions. The tensile direction is parallel to the extrusion direction. The sample's gauge has rectangular cross-section of dimensions 5 x 6 mm^2 and the gauge length is 52 mm. Tensile tests were performed using an Instron machine (Instron 5969, 50kN load cell) under quasi-static conditions ($\dot{\varepsilon} = 3 \times 10^{-3}\ s^{-1}$) at room temperature (25℃). We have used the mechanical extensometer to measure the strain. There are 3 repetitions for each material condition.

Tests at elevated temperatures of 150℃, 200℃, 250℃, 300℃ and 350℃ were performed with the same system, the sample being heated at a rate of $5℃/s$ to reach the test temperature, followed by a 300 s hold before the beginning of the test. The deformation of samples tested at elevated temperatures was provided by the machine. Hardness was measured with a microhardness tester (Qness 60M QATM) with a load of 500 g, with 15 s dwell time [22], in accordance with ASTM E92. At least three samples were tested in each condition, and 10 measurements were made of each sample. The average values are reported here.

Elastic-plastic fracture toughness (J_{Ic}) was measured using an Instron (Instron 5969, 50kN load cell) uniaxial load frame by single-edge bend testing according to the ASTM E1820 standard [23]. Specimens had dimensions 12 X 6 X 60 mm and the loading span was 50 mm. Prior to testing, fatigue loading with amplitudes of 0.10 to 0.20 kN, was used to generate a pre-crack extending a length of 1.2 mm from a machined notch, normal to the axial direction of the extruded rods to achieve a standard crack length to width ratio of 0.5.

2.3.3 Microstructure characterization

Test specimens for both XRD and metallographic (SEM/EBSD) analysis were prepared by sectioning and grinding with fixed abrasive papers (320, 800, and 1200 grit) followed by polishing with loose abrasive suspension-embedded cloths (alumina and colloidal silica, 5 mm to 0.05 mm). XRD patterns were collected using a Panalytical XRD instrument with Cu-K_α radiation between 20^0 to 90^0, with a scan rate of 1^0 per minute. FEI SEM was used for the metallography and fractography studies. Polished planar surfaces were prepared for examination by etching with Kellar's reagent for 10 s whilst fracture surfaces were examined directly, with no further preparation.

EBSD was performed using an Oxford SEM microscope. The respective specimens were polished using diamond and colloidal silica to minimize the surface roughness. The EBSD step size is 0.05 mm for CE, CE-10, and CE-100, and it is 1 mm for as-cast Al-10%Ce. The analysis of EBSD images was performed using MTEX software. The mapping is based on the FCC Al and orthorhombic $Al_{11}Ce_3$.

2.5 Results

2.4.1 Phase analysis

The normalized XRD spectra of hypoeutectic (Al-4Ce), eutectic (Al-10Ce), and hypereutectic (Al-16Ce) cast alloys are shown in Fig. 2.1a. The a-Al phase (red) and $Al_{11}Ce_3$ precipitates (black) are identified in all three alloys. Normalized XRD spectra of as-cast, as-extruded, and extruded and heat treated Al-10Ce eutectic alloy are shown in Fig. 2.1b. These samples also indicate the presence of a-Al and $Al_{11}Ce_3$ precipitates. In Fig. 2.1 a, the relative intensities of $Al_{11}Ce_3$ peaks in the as-cast samples increase as the Ce concentration increases, as expected. The height of these peaks is essentially invariant upon annealing at 300℃ for 100 h. The highest intensity peaks for a-Al are (111) or (200) in all compositions and material states considered. The intensity of the Al (200) peak decreases after extrusion and heat treatment as compared to as cast Al-10Ce, which indicates the development of (111) texture during extrusion, as discussed further in section 2.4.2. No evidence of phase transformations is observed during extrusion and heat treatment, illustrating the thermal stability of this alloy, at least with regard to phase composition.

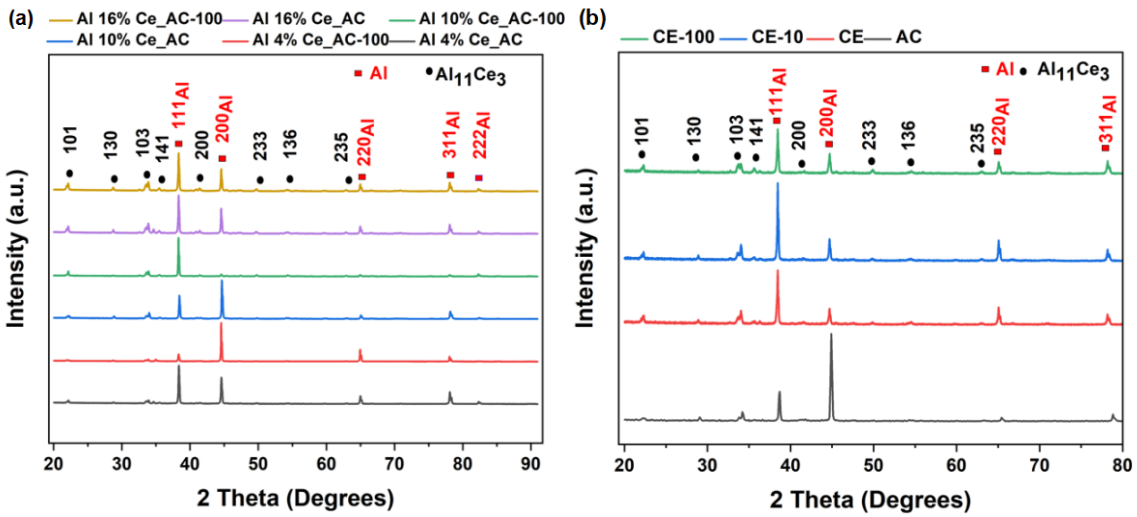

Figure 2.1. (a) XRD of Al-4Ce, Al-10Ce, and Al-16Ce for samples AC and AC-100 (b) XRD of AC, CE, CE-10, and CE-100 for Al-10Ce.

2.4.2 Microstructural evolution during extrusion and subsequent annealing

2.4.2.1 Scanning electron microscopy

The microstructure of AC Al-4Ce, Al-10Ce and Al-16Ce is observed by scanning electron microscopy (SEM) and representative micrographs are shown in Fig. 2.2(a-c). The microstructure for Al-4Ce shown in Fig 2.2a includes primary Al (fcc) phase, appearing as large dendritic features separated by a two-phase interdendritic eutectic constituent, comprised of Al (fcc) (dark) and $Al_{11}Ce_3$ (light) phases with a fine irregular lamellar structure. The Al-10Ce microstructure presents exclusively the eutectic constituent (Fig. 2.2b), while the Al-16Ce microstructure includes primary $Al_{11}Ce_3$ phase (light) exhibiting a blocky script-like morphology within the irregular eutectic constituent of Al (fcc) plus $Al_{11}Ce_3$, as shown in Fig 2.2c. These observations are consistent with expectations and with the previously published literature on Al-Ce binary alloys [15,24–26]. More uniform and finer microstructures were formed in the Al-10Ce alloy compared to the other two compositions considered. Due to this, we focus the subsequent microstructure characterization on the eutectic Al-10Ce alloy. The intermetallic mean size (lamellar thickness) of Al-4%Ce, Al-10%Ce, and Al-16%Ce is 0.28 mm, 0.24 mm, and 0.60 mm, respectively. The inter-lamellar spacing of Al-4%Ce, Al-10%Ce, and Al-16%Ce is 0.39 mm, 0.65 mm, and 1.98 mm, respectively.

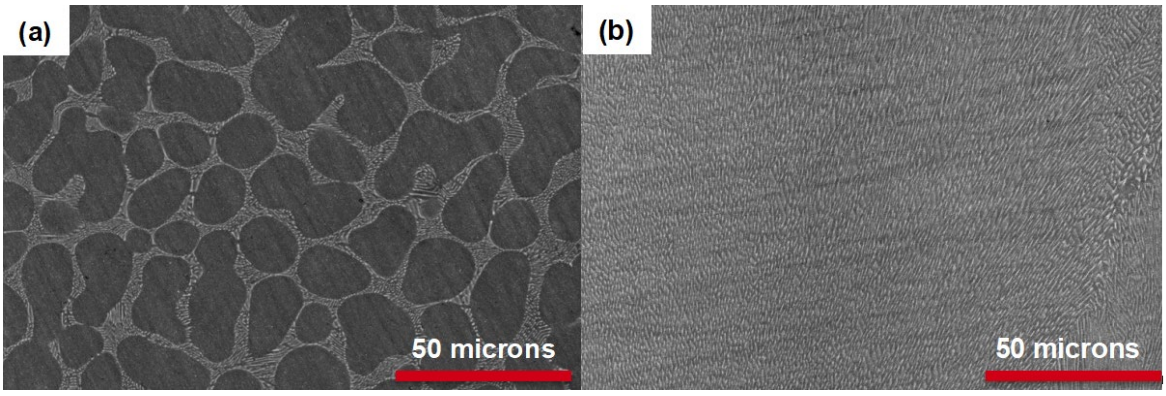

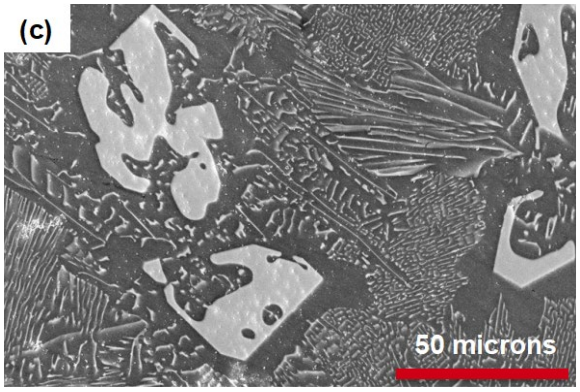

Figure 2.2: The microstructure of as-cast: (a) Al-4Ce alloy (black = Al, white = $Al_{11}Ce_3$, lighter shade = eutectic), (b) Al-10Ce eutectic alloy, (black = Al, white = $Al_{11}Ce_3$) and (c) Al-16Ce alloy (black = Al, white = $Al_{11}Ce_3$).

The microstructure of CE, CE-10, CE-100 (Al-10Ce) is shown in Fig. 2.3 A homogenous and highly refined microstructure was observed after extrusion. Two phases are present: the a-Al (fcc) matrix and the eutectic structure, with the eutectic structure including Al and $Al_{11}Ce_3$ intermetallic. Comparison between Fig 2.3a and Fig 2.3b reveals the changes in $Al_{11}Ce_3$ morphology within the eutectic structure associated with the extrusion process. Particles are refined in size and undergo a change of shape from longer plate-like lamellae to shorter lamellae in the extruded condition. In addition, the particles become preferentially aligned with the extrusion direction.

These observations are consistent with prior reports of lamellar fragmentation and alignment during cold rolling [27], as previously discussed. This morphology change is expected to influence ductility, a consideration discussed further in section 2.4.7 The post-extrusion $Al_{11}Ce_3$ particle size within the eutectic constituent appears to be somewhat bimodal, with a small fraction of coarse particles, suggesting that some particles remain unbroken. Figure 2.3 further shows that the particle distribution remains unchanged after exposure to 300℃ for 10 h and 100 h since, again consistent with expectations given the low diffusivity of Ce in Al and the correspondingly sluggish particle coarsening. The intermetallic particle mean size (lamellar thickness) of CE, CE-10, and CE-100 is 0.24 mm, 0.19 mm, and 0.21 mm, respectively. The interlamellar distance of CE, CE-10, and CE-100 is 0.36 mm, 0.29 mm, and 0.30 mm, respectively.

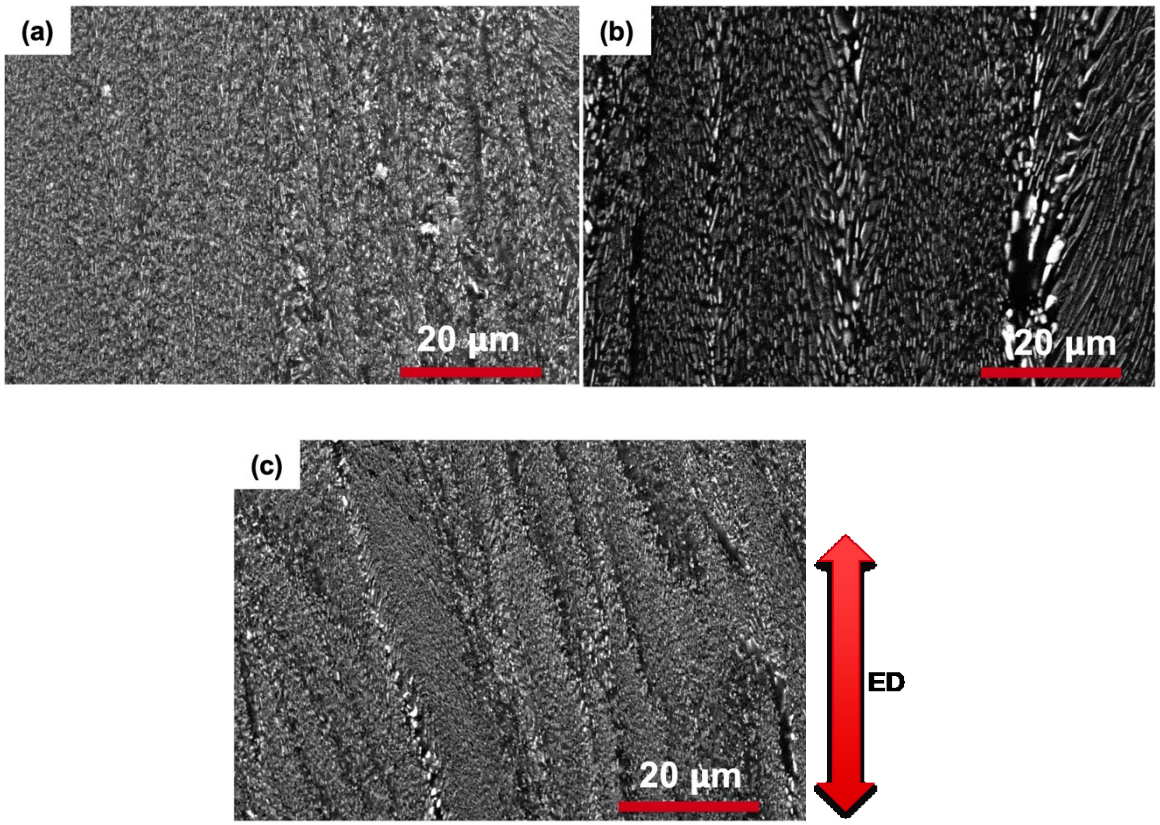

Figure 2.3: Microstructure of Al-10Ce in the (a) CE, (b) CE-10, and (c) CE-100 states. The extrusion direction is shown by the red arrow and applies to all 3 panels.

2.4.3 Electron backscattered diffraction

Electron backscattered diffraction technique is used to characterize the grain size, grain misorientation, phase fraction, micro strain, and texture in the as cast, extruded and heat-treated Al-10Ce alloy. Figures 2.4a-c show the electron backscattered diffraction (EBSD) maps of Al-10Ce in the CE, CE-10, and CE-100 conditions. The map of the CE sample shows a heterogenous microstructure with different grain sizes in different regions. For example, the grain size of (101) oriented grains is 3.27 $\pm$ 2.67 mm, 2.66 $\pm$ 0.78 mm, and 3.67 $\pm$ 0.76 mm for CE, CE-10, and CE-100 conditions. We observe strip-like regions oriented in the extrusion direction, with larger grains also elongated in the extrusion direction, and which are separated by finer grains. This microstructure in annealed conditions exhibits similar features, but the fine grains are distributed more uniformly throughout the microstructure. The average grain size in the extruded state is 2.06 $\pm$ 0.68 mm. The grain size distribution is shown in the Supplementary material, Fig. S1. The CE-10 and CE-100 have mean grain sizes of 2.27 $\pm$ 0.75 mm and 2.99 $\pm$ 0.72 mm, respectively, i.e annealing does not

modify the grain size within the accuracy of the present measurements. The respective distributions are also shown in Fig. S1.

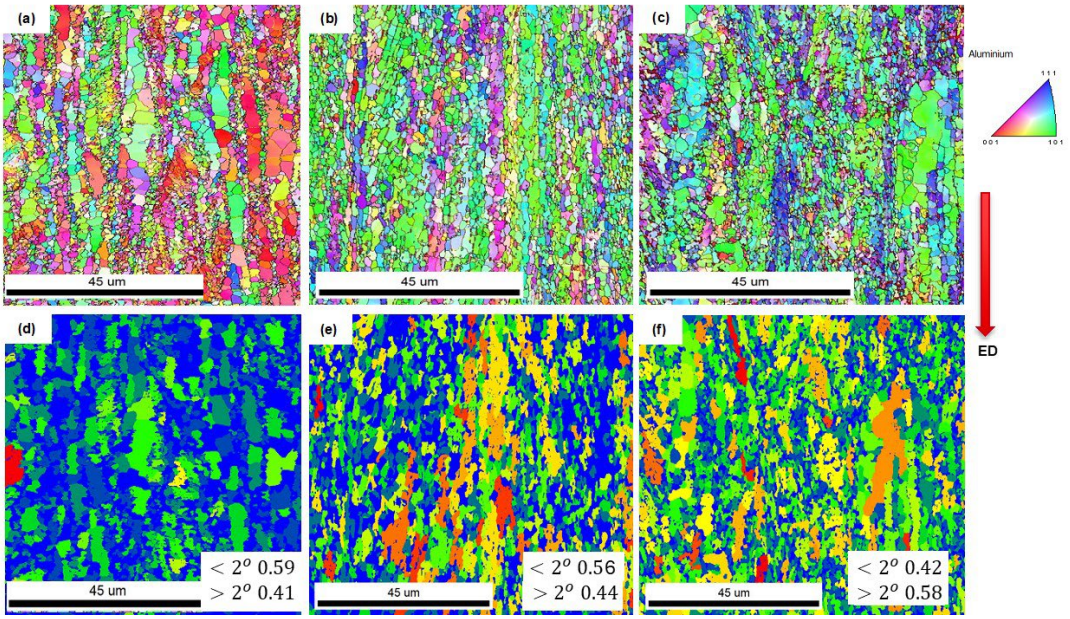

Figure 2.4: IPF maps of Al-10Ce in the (a) CE, (b) CE-10, (c) CE-100 states. The GOS maps corresponding to panels (a), (b) and (c) are shown in (d), (e) and (f), respectively. Values in the legend represent grain fractions with GOS values above and below the 2^o threshold.

The average misorientation distribution is 28.93°, 26.53°, 26.40° for CE, CE-10, and CE-100, respectively. The distributions of misorientation are shown in Fig. S1 for all states. Annealing leads to a gradual shift of the misorientation distribution to lower angles. The fraction of high angle grain boundaries is 0.71, 0.65, and 0.62 for CE, CE-10, and CE-100 sample condition respectively. The inverse pole figure, grain size distribution and the misorientation distribution of as-cast samples are shown in the Supplementary material, Fig. S2. The grain size of as cast samples is 582 ± 143.35 mm, which underlines the significant grain size reduction obtained upon extrusion. The average misorientation distribution is 11.54°, smaller than in the extruded samples.

The Grain Orientation Spread (GOS) maps for the three states are shown in Fig. 2.4d-f. The fractions of grains with GOS values below and above the 2^o threshold are indicated in the legend for each panel. We observe that annealing, which does not change the grain size, as discussed in the previous paragraph, leads to increasing the fraction of low angle grain boundaries. The phase maps for the three states shown in Fig. S3. The $Al_{11}Ce_3$ phase volume fraction inferred from these images is 7% in the extruded state and 8.2% and 8.4% after

annealing at 300℃ for 10h and 100h, respectively. However, XRD data shown in Fig. 2.1 indicates no change in the height of the peaks corresponding to the intermetallic during annealing. This suggests that the non-monotonic variation obtained from EBSD (Fig. S3) is an artifact due to the limited field of view and possibly the error associated with the identification of small precipitates.

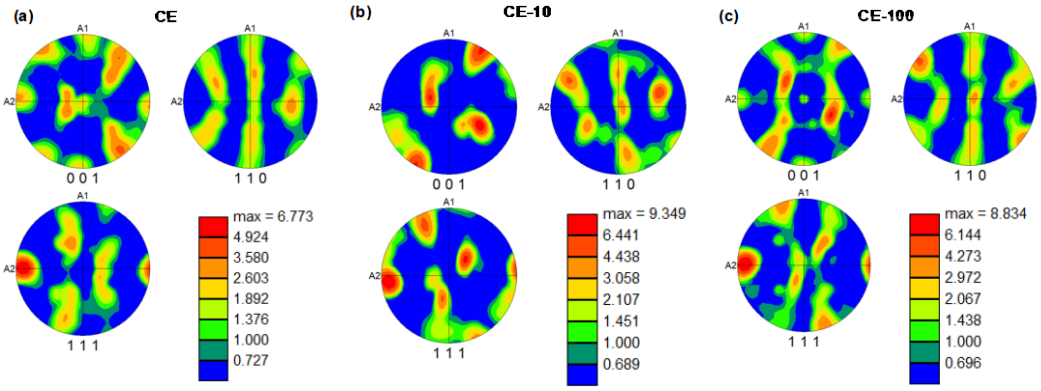

Figure 2.5: Pole figure texture of (a) CE, (b) CE-10, (c) CE-100, A1 is extrusion direction and A2 is transverse direction.

Figures 2.5a-c show the pole figure of (001), (110), and (111) projections in the CE, CE-10, and CE-100 sample conditions. The brass texture ({110}<112>)observed in the extruded sample becomes stronger after annealing for 10 h, while after annealing for 100 h the texture becomes less well defined. The maximum intensity of the pole figure is shown in Table 2. It further quantifies that the texture strengthens to some extent upon annealing for 10 h and becomes weaker after 100 h of annealing. This impacts the mechanical properties, as discussed in section 2.4.4 This texture evolution process entails the formation of low angle grain boundaries (evidenced by the GOS data in Fig. 2.4), while the total dislocation density remains largely unaffected – a conclusion emerging from the analysis presented next.

The kernel average misorientation (KAM) values of the CE, CE-10, and CE-100 are determined from the EBSD data and are used to evaluate the dislocation density. The dislocation density (geometrically necessarily dislocations), ρ_{GND}, is calculated based on the average KAM value. It is obtained using the classical strain gradient approach and is given by the following expression [28]:

$$\rho_{GND} = \frac{2\theta}{n\lambda|b_D|} \quad (1)$$

where θ is the experimentally measured KAM value, λ is the step size (1 mm), n is the number of nearest neighbors averaged in the KAM calculations (here it is 5), and b_D is the Burgers vector corresponding to the active slip system (b_D = 0.286 nm). The dislocation density values obtained with Eq. (1) are shown in Table 2.2. The dislocation density is approximately identical in the three states of the material and takes values in the vicinity of $10^{14}\ m^{-2}$.

The XRD data is also used to calculate the dislocation density ρ using the expression [29]:

$$\rho = \frac{2\sqrt{3}\epsilon}{d b_D} \tag{2}$$

where d is crystallite size, ϵ is the micro strain and b_D = 0.286 nm. The Williamson-Hall equation is used to determine the micro strain and crystallite size [30,31]:

$$\frac{\beta \cos\theta}{\lambda} = \frac{k}{d} + 4\epsilon \frac{\sin\theta}{\lambda} \tag{3}$$

where k is the Debye–Scherrer constant (k = 0.9), λ is the wavelength of the radiation, (l = 0.154 nm), β is the full width at half maximum (in radian), calculated from the obtained peaks in the XRD diffractogram, Fig. 2.1b, and θ is the half of the Bragg angle of the respective peaks. The Williamson-Hall plot for AC and CE-100 are shown in Fig. S4. The values of ρ obtained with Eq. (2) are provided in Table 2.2. It is observed that $\rho > \rho_{GND}$, this can be explained by the sensitivity of each technique to the depth of probing. EBSD extracts information from 10-20 nm thick layer under the surface while the thickness probed by XRD is up to several microns. Another aspect is that EBSD can distinguish between cells and random dislocations whereas XRD provides only an average value of ρ. this can be explained by the sensitivity of each technique to the depth of probing. However, EBSD distinguishes between geometrically necessary and stochastic dislocations, while XRD provides only an average value of the dislocation density.

We conclude from this data that extrusion produces strong microstructural refinement (both smaller grains and smaller intermetallic particle) and increased crystallographic texture. Annealing at 300℃ up to 100 h has a negligible effect on the grain and precipitate size, leaves the dislocation density unchanged, but reduces the texture. This suggests that this level of annealing should minimally impact the mechanical properties – a result discussed further in section 2.4.4.

Table 2.2. Grain size, maximum texture intensity, and dislocation density (obtained from XRD, ρ_{XRD} and EBSD, ρ_{GND}) for AC, CE, CE-10 and CE-100 Al-10Ce alloy.

	Grain size (mm)	**Maximum Texture Intensity**	**Main texture component**	**$\boldsymbol{\rho}$ ($\times \mathbf{10^{14}}\ \boldsymbol{m^{-2}}$) XRD**	**$\boldsymbol{\rho_{GND}}$ ($\times \mathbf{10^{14}}\ \boldsymbol{m^{-2}}$) EBSD**
AC	582	5.63	Random texture	2.92	0.10
CE	2.06	15.78	brass texture ({110}<112>)	5.56	1.16
CE-10	2.27	12.99	brass texture ({110}<112>)	2.56	0.90
CE-100	2.99	6.45	brass texture ({110}<112>)	2.94	1.40

2.4.4 Mechanical properties

In this section, we present testing results and analysis pertaining to the mechanical properties of the Al-Ce binary alloys. We consider first the effect of alloy composition and heat treatment, examining the tensile response and hardness for all three alloy compositions without any extrusion. We then focus on the eutectic alloy (Al-10Ce) and the coupled effects of extrusion and post-extrusion heat-treatment, specifically examining the AC, CE, CE-10, and CE-100 conditions. Third, we consider the elevated temperature mechanical properties, examining the response of the Al-10Ce alloy at temperatures from 150°C to 350°C. Finally, we examine the room temperature fracture toughness of the Al-10Ce alloy in all conditions.

2.4.4.1 Mechanical properties of as-cast samples

Figure 2.6a shows the observed stress-strain response for 4%, 10% and 16%Ce in the AC, AC-10, and AC-100 conditions, without extrusion. The nominal yield stress, strength and elongation at failure are compared in Table 2.3. As expected, the Al-10Ce alloy exhibits the highest strength, owing to the uniform distribution of fine intermetallics of the eutectic structure. Lower strength is obtained for the hypoeutectic composition, containing a substantial fraction of primary Al (fcc), while the hypereutectic is excessively brittle due to

the presence of large particles of primary $Al_{11}Ce_3$. Figure 2.6a reveals that the 300°C heat treatment has only a minor influence on tensile properties, with the highest ultimate strength observed after 100 h of exposure.

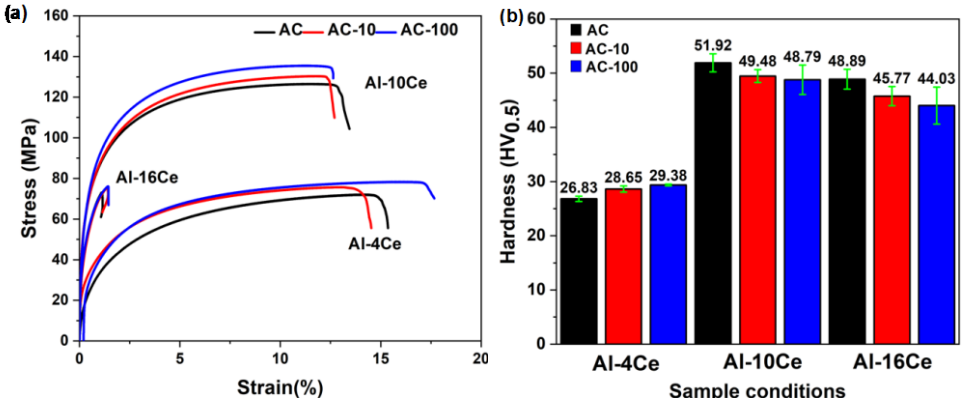

Figure 2.6. (a) Nominal stress-strain curves and (b) hardness of AC, AC-10, and AC-100 specimens for Al-4Ce, Al-10Ce, and Al-16Ce.

The influence of microstructure indicated by the measured tensile response is further supported by the microhardness test results shown in Fig. 2.6b. Each value represents the average of at least 10 measurements, with the standard deviation being indicated by the error bars. For the AC condition, the average hardness was measured to be 28, 52, and 48 HV for 4, 10, and 16 wt% Ce, respectively. Similar values and variation with Ce content were observed for the AC-10 and AC-100 conditions. The excellent property retention observed in both tensile and hardness testing is consistent with the microstructure-based observations of thermal stability discussed in the preceding section.

Table 2.3. Tensile properties (yield stress, YS, tensile strength, UTS, and strain at failure, %El) for three alloys in AC, AC-10, and AC-100 conditions. The standard deviation is shown in brackets.

	Al-4Ce			**Al-10Ce**			**Al-16Ce**		
	AC	**AC-10**	**AC-100**	**AC**	**AC-10**	**AC-100**	**AC**	**AC-10**	**AC-100**
YS (MPa)	29.9 (0.9)	28.12 (0.8)	27.8 (0.7)	62.3 (1.5)	61.7 (1.5)	59.9 (1.8)	44.7 (2.3)	42.0 (2.5)	45.4 (2.0)
UTS (MPa)	72.1 (1.8)	75.9 (1.8)	78.3 (1.8)	126.7 (3.0)	130.6 (2.7)	135.7 (3.4)	78.9 (4.0)	79.2 (3.5)	80.2 (2.3)

Table 2.3 Continued

	Al-4Ce			**Al-10Ce**			**Al-16Ce**		
	AC	**AC-10**	**AC-100**	**AC**	**AC-10**	**AC-100**	**AC**	**AC-10**	**AC-100**
%El	15.4 (0.1)	14.5 (0.2)	17.2 (0.1)	13.4 (0.1)	12.7 (0.2)	12.6 (0.8)	1.4 (0.01)	1.2 (0.01)	1.4 (0.01)

2.4.5 Comparison of mechanical properties of as cast and extruded samples

Since the eutectic alloy Al-10Ce showed superior mechanical properties compared to the other two compositions, it was further considered for extrusion and evaluation of property retention after exposure to elevated temperatures. The room temperature engineering stress-strain curves for this alloy in the CE, CE-10, and CE-100 conditions are shown in Fig. 2.7a. The extruded (CE) samples showed improved mechanical properties compared to the as-cast (AC) condition. The yield stress increases three times, while the tensile strength doubles, and elongation at failure increases from 13% to 22%. The improvement in ductility is attributed to refinement and increased uniformity of the distribution of the $Al_{11}Ce_3$ phase caused by extrusion. We note here that the structural refinement includes both size and shape of the particles, which change from thin and interconnected lamellae to rod-like shapes of rather low aspect ratio, Fig. 2.4a.

Fig. 2.7 shows that the mechanical properties are retained after exposure to 300℃ for 10 h and 100 h, for both the ac-cast (AC) and cast/extruded (CE) alloys. Moreover, the extruded alloy experiences a modest increase in strength and ductility after 10 h of exposure, an effect not observed for the AC alloy. Considering that heat treatment does not give rise to any observable grain growth or particle coarsening, as discussed in section 2.4.3, we attribute this effect to the brass texture ({110}<112>) which develops during extrusion and after 10 h annealing (i.e. CE-10) and then becomes weaker upon long-term exposure (i.e. CE-100). It is prudent here to note that these assertions are based on limited initial observations and that more definitive correlation with texture evolution and the influence of extrusion deformation will require further investigation. In any event, our mechanical property measurements show that the high thermodynamic stability and resistance to coarsening of the $Al_{11}Ce_3$ precipitates provides nearly 100% retention of the as-extruded mechanical properties during exposure to

300°C for up to 100 h, for the Al-10Ce alloy – a finding similar to that reported for as-cast samples in section 2.4.4.1. The Young's modulus of CE and CE-100 is ~74 GPa.

The microhardness of cast and extruded samples, before and after heat treatment, is shown in Fig. 2.7b. The hardness is 66.3 HV for the CE case, which is higher than the AC condition (51.92 HV) but the increase of the hardness in extruded samples compared with the cast state is smaller than the increase of the yield stress and strength, Fig. 2.7a. The hardness does not change upon heat treatment, within the accuracy of the present measurement. Annealing of the extruded samples at 300℃ for 100 h leads to a hardness of 60.97 HV. Longer anneals at the same temperature, of 300 h and 400 h, led to hardness values of 60.54 HV and 59 HV, respectively.

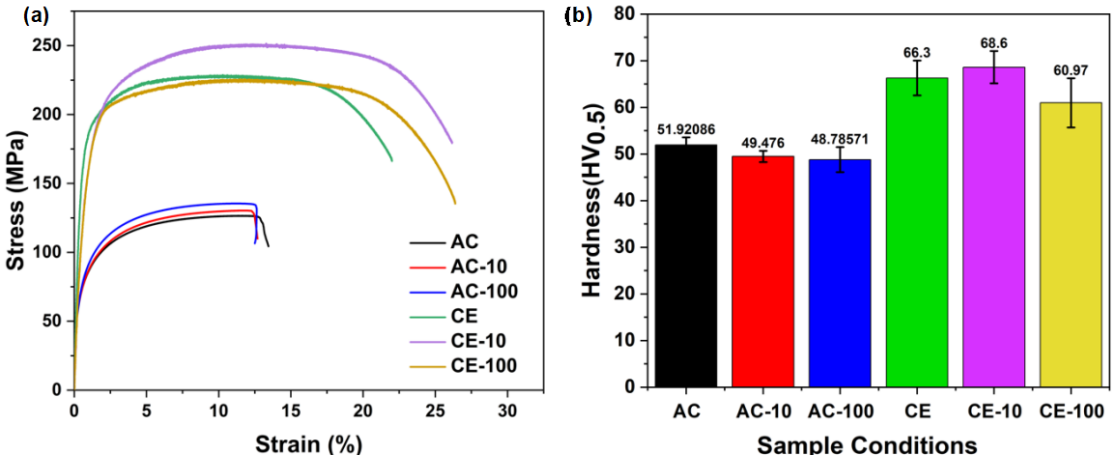

Figure 2.7. (a) Engineering stress-strain curves of extruded and cast Al-10Ce samples, and (b) hardness measured at room temperature for the same set of samples. The curves in (a) are averages of 3 samples for each reported state. The hardness in (b) is computed as average of 10 measurements for each condition and the bars show the standard deviation.

The fracture surfaces of samples subjected to tensile loading were imaged with SEM to investigate the mechanisms of failure and correlate with microstructural features. These images for Al-10Ce are shown in Fig. S5. Fracture surfaces of both cast and extruded samples contain mainly dimples. The cast samples showed some occasional shrinkage porosity. The extruded Al-10Ce alloys exhibit deeper and smaller dimples compared to as cast alloys, as shown in Fig. S5d-f. The small dimples size indicates that intense plastic deformation took place during failure. This agrees with the rather large strain at failure of 22% of the extruded samples.

2.4.6 High temperature mechanical properties of the cast and extruded Al-10Ce alloy

The eutectic alloy (Al-10Ce) was further tested at elevated temperatures of 150℃, 200℃ 250℃, 300℃ and 350℃. The stress-strain curves reported in Fig. 8a and 8b correspond to the AC and CE states, respectively. The yield stress and the strength are gradually decreasing with increasing temperature. We observe that the ductility does not change significantly as the temperature increases.

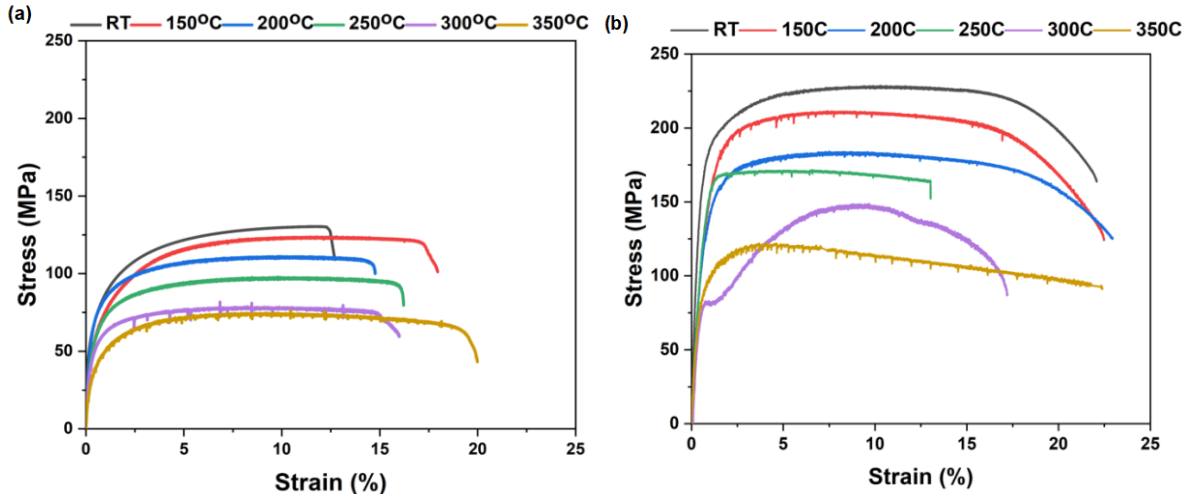

Figure 2.8. Nominal stress-strain curves of Al-10Ce alloy at temperatures ranging from room temperature to 350℃: (a) AC and (b) CE states.

It is instructive to compare the temperature resistance of this alloy with the behavior of AA2618, which is one of the commercial high temperature Al alloys. This comparison is shown in Fig. 2.9a, where the strength of Al-10Ce (Fig. 2.8) is plotted against temperature along with results from elevated temperature testing of pure Al [32,33] and AA2618 [34]. At 300℃ the tensile strength of both cast and extruded Al-10Ce is higher than the strength of AA2618. Figure 2.9b shows the temperature dependence of the strength normalized by the strength at room temperature. The alloys studied in this work lose 34% of their strength as temperature is increased to 300℃, while AA2618 looses 90% of its strength.

The decrease of the flow stress in Al-10Ce is due to the softening of the Al phase, while the invariance of the ductility is due to the fact that the precipitates do not evolve at these temperatures. The data in Fig. 2.9b supports this conjecture: consider the microstructure to be a composite of a soft phase (Al), with temperature-dependent flow stress, and a hard phase which does not flow plastically ($Al_{11}Ce_3$). In this situation, the temperature dependence

of the alloy is dictated by the temperature dependence of the soft phase. The pure Al curve in Fig. 9b is parallel to the two curves corresponding to AC and CE states, which confirms the hypothesis. It is interesting to observe that, at temperatures below 150℃, the flow stress of the alloy is temperature independent. This is probably due to the confinement effect of the fine $Al_{11}Ce_3$ precipitates on the plastic flow of the Al matrix. At the same time, the AA2618 curve exhibits a segment parallel to the pure Al segment at temperatures below 150℃, indicating thermal softening due to the Al "matrix," followed by an abrupt drop due to precipitate dissolution, which is followed by a third segment parallel to the pure Al curve.

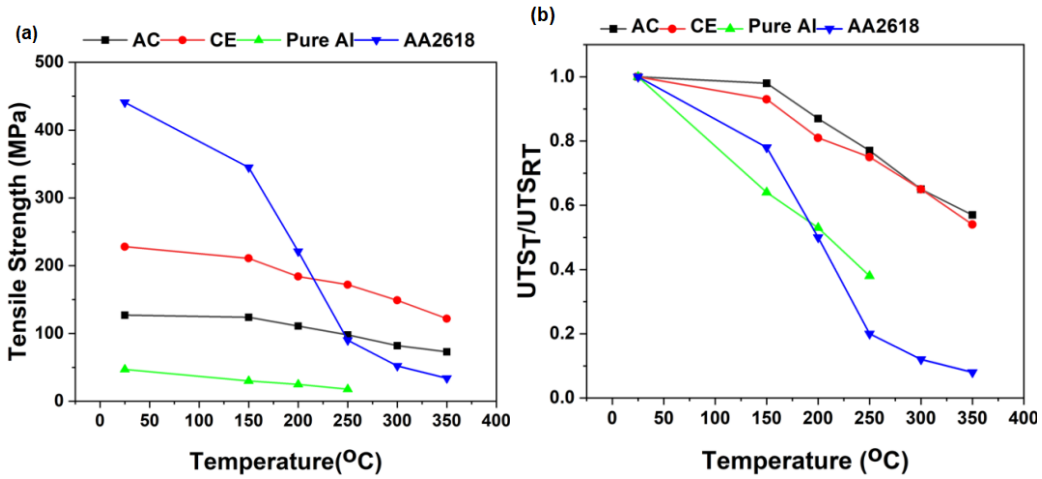

Figure 2.9. (a) Temperature dependence of the strength, UTS, and (b) ratio of UTS normalized by UTS at room temperature for Al-10Ce in AC, CE, pure Al and AA2618.

The superior thermal stability of Al-10Ce compared with AA2618 can be understood based on the stability of the $Al_{11}Ce_3$ precipitates. AA2618 has alloying elements such as Cu, Si, and Mg which have relatively high solubility in Al and higher diffusion coefficients in Al than Ce at these temperatures. The solubility of Ce in Al is low, with the maximum value being less than 0.005 wt% at 642 ℃. This is much lower than the solubility of Cu, Mg and Si in Al (5 wt% at 600℃, 14.9 wt% at 451℃ and 12.5 wt% at 577℃, respectively) [35]. The $Al_{11}Ce_3$ precipitates are thermodynamically stable up to 600℃, while the kinetics of dissolution is also very slow due to limited Ce diffusivity [36].

3.3.4 Fracture toughness of cast and extruded Al-10Ce alloys

The fracture toughness of the eutectic cast and extruded alloy before and after annealing at 300℃ for 10 h and 100 h was measured using the single-edge bend configuration with load-line displacement measurement, in accordance with the ASTM-

E1820 standard [23]. This requires evaluating the area under the force-displacement curve resulting from a 3-point bend test performed with a notched sample, up to the maximum force value, Fig. 10. The energy release rate has elastic and plastic components given by Eq. (4) and (5) [23]:

$$J_{el} = \frac{K_Q^2(1-\nu^2)}{E} \quad (4)$$

$$J_{pl} = \frac{\eta_{pl}A_{pl}}{B(W-a_0)} \quad (5)$$

where K_Q is the stress intensity at fracture (i.e. maximum attained), ν and E are the Poisson's ratio and elastic modulus, respectively. Values of 0.34 and 70 GPa are used for ν and E respectively, in agreement with our test results, for the calculation of J_{el}. Further, η_{pl} is taken to be 1.9 as defined by ASTM E-1820 standard, A_{pl} is the area under the load-displacement curve up to the maximum point. S, W, B, and a_o are the span length, width, net specimen thickness, and notch length. The critical energy release rate, J_{Ic}, is evaluated as the sum of the two components of Eqs. (4) and (5) corresponding to the moment of crack growth (i.e. peak force):

$$J = J_{el} + J_{pl} \quad (6)$$

The peak load values of J_{el}, J_{pl} and J_{Ic} are shown in Table 2.4. The extruded samples have substantially larger toughness (55.43 J/m^2) than the as-cast samples (18.62 J/m^2). The plastic component J_{pl} is much larger than J_{el} and represents 99% of J_{Ic}, which is expected for a ductile metallic alloy. The annealed samples show similar fracture toughness values as compared to their non-heat treated counterparts in both cast and extruded conditions which, again, underscores the microstructural stability of this alloy. The highest fracture toughness (J_{Ic}) values are reported in Al alloys for the wire-arc DED-processed Al-Si, which is 36.8 kJ/m^2[37]; Al-Li alloys have J_{Ic} value of ~26 kJ/m^2[38]. The important observation beyond the insensitivity to annealing supported by the other data reported here and, in the literature, is the drastic simultaneous increase of the toughness, strength and ductility of the alloy upon extrusion.

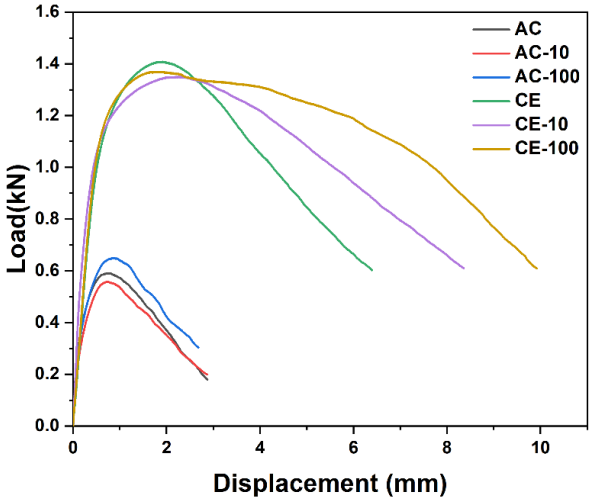

Figure 2.10. Load-displacement curves of notched samples in the 3-point bend configuration of the cast and extruded Al-10Ce alloy before and after heat treatment.

Table 2.4. Values of J_{el}, J_{pl} and J_{Ic} for cast and extruded samples, before and after annealing.

	Load (N)	J_{el} **(kJ/m²)**	J_{pl} **(kJ/m²)**	$J = J_{el} + J_{pl}$ **(kJ/m²)**
AC	591	0.57	18.05	18.62
AC-10	558	0.51	14.72	15.23
AC-100	650	0.68	19.22	19.90
CE	1408	0.058	55.36	55.42
CE-10	1349	0.045	43.28	43.33
CE-100	1369	0.10	54.02	54.12

2.4.7 Strengthening mechanisms and ductility of extruded samples.

The strengthening mechanisms operating in these alloys include grain size strengthening, strain hardening and strengthening due to the presence of the fine $Al_{11}Ce_3$ dispersion. Solid solution strengthening is precluded by the low solubility of Ce in Al. The contribution of the strengthening mechanisms is considered the be additive, which implies the assumption of them acting independently [27,39]:

$$\sigma_y = \sigma_{dis} + \sigma_d + \sigma_{gs}, \quad (7)$$

where, σ_y is the yield stress, σ_{dis} is the contribution of dispersion strengthening, σ_d corresponds to strain hardening, and σ_{gs} accounts for the effect of grain boundaries (Hall-Petch effect). Grain size strengthening is expressed by the Hall-Petch relation [40]:

$$\sigma_{gs} = \sigma_o + kd^{-0.5}, \quad (8)$$

Where σ_o is the lattice friction (Peierls stress), the grain size d is evaluated based on the EBSD results, Table 2.2, and k is the Hall-Petch coefficient with a value of 0.07 MPa $m^{0.5}$ [41]. σ_o is considered equal to 20 MPa, which is the yield stress of pure Al.

Strain hardening results from interaction and multiplication of dislocations during plastic deformation. The contribution of dislocation strengthening (i.e. strain hardening) can be calculated using the Taylor equation [42]:

$$\sigma_d = M\alpha b_D G\rho^{0.5}, \quad (9)$$

where M is the Taylor factor, with a value of 2.94 for Al [43], α is the strength coefficient with a value of 0.24 [44], b_D is the Burgers vector ($b_D = 0.286$ nm), G is the shear modulus (G = 26 GPa) for pure Al, and ρ is the dislocation density evaluated based on EBSD and reported in Table 2.2.

The dispersoid number density and, to a smaller extent, their shape and distribution, define the contribution of σ_{dis} to the total flow stress [27,45]. In this study, we use Eq. (7) along with Eqs. (8) and (9) to infer the contribution of σ_{dis} to the measured yield stress. Therefore, σ_{dis} is calculated as:

$$\sigma_{dis} = \sigma_y - \sigma_{gs} - \sigma_d. \quad (10)$$

The contributions of the various strengthening mechanisms are listed in Table 2.5 for cast and extruded Al-10Ce before and after annealing. The percentage contribution to the total yield stress of each mechanism is indicated in parentheses.

The as-cast alloy has large grains and relatively low dislocation density, which implies a low yield stress. The contribution of σ_{dis} to the yield stress results comparable with that of the grain size strengthening mechanism. The as extruded (CE) and annealed alloys (CE-10, CE-100) have larger yield stress and larger σ_{gs}, σ_d and σ_{dis} compared with AC. The grain size mechanism, σ_{gs}, makes the largest contribution to the yield stress. Since the grain

size and dislocation densities in these alloys are not very sensitive to annealing, the contributions of these mechanisms to the yield stress are largely independent of the annealing state. An exception is observed in the case of CE-10 where σ_d is smaller due to the lower dislocation density (ρ_{GND} in Table 2.2 was used for this evaluation). This is compensated by σ_{dis}, which is larger than the values reported for CE and CE-100. However, in broad terms, the contribution to the yield stress of the three strengthening mechanisms is somewhat similar (each contributes approximately 1/3 of the yield stress), which is surprising given their very different microstructures.

Table 2.5. Contribution of grain size strengthening, σ_{gs}, strain hardening, σ_d, and dispersoid strengthening, σ_{dis}, to the yield stress of Al-10Ce cast and extruded samples before and after annealing. The fraction of the respective contribution to the total yield stress is reported in parentheses for each case and mechanism.

	$\boldsymbol{\sigma_{gs}}$ **(MPa)**	$\boldsymbol{\sigma_d}$ **(MPa)**	$\boldsymbol{\sigma_{dis}}$ **(MPa)**
AC	22.9 (36.8%)	16.6 (26.6%)	22.8 (36.6%)
CE	68.8 (39.1%)	56.5 (32.1%)	50.7 (28.8%)
CE-10	66.5 (34.1%)	49.8 (25.5%)	78.7 (40.4%)
CE-100	60.5 (34%)	62.1 (34.9%)	55.4 (31.1%)

2.6 Conclusion

This study focuses on the effect of extrusion on the structure, mechanical properties and thermal stability of Al-Ce binary alloys. The as cast alloys have large grain size, relatively low yield stress and strength, but strong thermal stability arising from the low solubility and diffusivity of Ce in Al (fcc). Extrusion leads to substantial refinement of the microstructure, involving both the Al (fcc) grain size and the $Al_{11}Ce_3$ intermetallic particle size. Relative to the as-cast state, extrusion results in larger yield strength, ultimate tensile strength, and elongation by factors of 3, 2, and 2, respectively. Moreover, because these gains are largely attributed to the $Al_{11}Ce_3$ structure, these properties are preserved upon annealing at 300°C for up to 100 h. The toughness also more than doubles in the extruded states relative to the as cast state, irrespective of the annealing applied. Testing at elevated temperatures indicates that the strength decreases as the test temperature increases, but this decrease is

much less pronounced than in existing commercial Al alloys considered to be temperature resistant. This indicates that adequate processing leading to microstructural refinement may render this class of alloys useful in applications in which high temperature resistance is required.

Acknowledgement

This work was supported by the US Department of Energy (DOE) through Grant No. DE-EE0010219.

Data availability statement

The data resulting from this investigation is included in the article.

2.7 References

[1] Y.H. Gao, C. Yang, J.Y. Zhang, L.F. Cao, G. Liu, J. Sun, E. Ma, Stabilizing nanoprecipitates in Al-Cu alloys for creep resistance at 300°C, Mater Res Lett 7 (2019) 18–25. https://doi.org/10.1080/21663831.2018.1546773.

[2] S. Mondol, T. Alam, R. Banerjee, S. Kumar, K. Chattopadhyay, Development of a high temperature high strength Al alloy by addition of small amounts of Sc and Mg to 2219 alloy, Materials Science and Engineering: A 687 (2017) 221–231. https://doi.org/10.1016/J.MSEA.2017.01.037.

[3] Z. Huda, P. Edi, Materials selection in design of structures and engines of supersonic aircrafts: A review, Materials & Design (1980-2015) 46 (2013) 552–560. https://doi.org/10.1016/J.MATDES.2012.10.001.

[4] S.O. Rogachev, E.A. Naumova, Thermal Stability of Al-Ca and Al-Ce Alloys Obtained by High-Pressure Torsion, J Mater Eng Perform 30 (2021) 9192–9199. https://doi.org/10.1007/s11665-021-06105-4.

[5] S. Shen, C. Wu, Y. Li, Y. Huang, W. Huang, P. Zhang, S. Zhong, Y. Lu, G. Luo, Z. Gan, J. Liu, Refining mechanism and elevated-temperature mechanical properties of Al-Ce alloys solidified under super gravity field, Materials Science and Engineering: A 879 (2023). https://doi.org/10.1016/j.msea.2023.145191.

[6] Y. Guo, J. Hu, Q. Han, B. Sun, J. Wang, C. Liu, Microstructure diversity dominated by the interplay between primary intermetallics and eutectics for Al-Ce heat-resistant alloys, J Alloys Compd 899 (2022). https://doi.org/10.1016/j.jallcom.2021.162914.

[7] E.T. Stromme, H.B. Henderson, Z.C. Sims, M.S. Kesler, D. Weiss, R.T. Ott, F. Meng, S. Kassoumeh, J. Evangelista, G. Begley, O. Rios, Ageless Aluminum-Cerium-Based Alloys in High-Volume Die Casting for Improved Energy Efficiency, JOM 70 (2018) 866–871. https://doi.org/10.1007/s11837-018-2861-9.

[8] G.S. Cole, A.M. Sherman, Light weight materials for automotive applications, Mater Charact 35 (1995) 3–9. https://doi.org/10.1016/1044-5803(95)00063-1.

[9] B. Stojanovic, M. Bukvic, I. Epler, APPLICATION OF ALUMINUM AND ALUMINUM ALLOYS IN ENGINEERING, Applied Engineering Letters 3 (2018) 2466–4847. https://doi.org/10.18485/aeletters.2018.3.2.2.

[10] F. Czerwinski, Cerium in aluminum alloys, Journal of Materials Science 2019 55:1 55 (2019) 24–72. https://doi.org/10.1007/S10853-019-03892-Z.

[11] D. Weiss, Improved High-Temperature Aluminum Alloys Containing Cerium, J Mater Eng Perform 28 (2019) 1903–1908. https://doi.org/10.1007/s11665-019-3884-2.

[12] Z.C. Sims, O.R. Rios, D. Weiss, P.E.A. Turchi, A. Perron, J.R.I. Lee, T.T. Li, J.A. Hammons, M. Bagge-Hansen, T.M. Willey, K. An, Y. Chen, A.H. King, S.K. McCall, High performance aluminum-cerium alloys for high-temperature applications, Mater Horiz 4 (2017) 1070–1078. https://doi.org/10.1039/c7mh00391a.

[13] F. Czerwinski, The Growth of Quaternary Divorced Eutectic in Al–Ce–Si–Mg Alloys, Metall Mater Trans A Phys Metall Mater Sci 54 (2023) 391–398. https://doi.org/10.1007/s11661-022-06911-y.

[14] F. Czerwinski, B.S. Amirkhiz, On the Al-Al11Ce3 eutectic transformation in aluminum-cerium binary alloys, Materials 13 (2020) 1–27. https://doi.org/10.3390/ma13204549.

[15] J. Ye, K. Dai, M. Gao, J. Chen, R. Guan, Primary phase transformation mechanism in a hypereutectic Al-Ce alloy during rapid solidification, Mater Lett 340 (2023). https://doi.org/10.1016/j.matlet.2023.134172.

[16] W. Wang, Q. Pan, G. Lin, X. Wang, Y. Sun, X. Wang, J. Ye, Y. Sun, Y. Yu, F. Jiang, J. Li, Y. Liu, Microstructure and properties of novel Al-Ce-Sc, Al-Ce-Y, Al-Ce-Zr and Al-Ce-Sc-Y alloy conductors processed by die casting, hot extrusion and cold drawing, J Mater Sci Technol 58 (2020) 155–170. https://doi.org/10.1016/j.jmst.2020.03.073.

[17] S.O. Rogachev, E.A. Naumova, E.A. Lukina, A. V. Zavodov, V.M. Khatkevich, High strength al–la, al–ce, and al–ni eutectic aluminum alloys obtained by high-pressure torsion, Materials 14 (2021). https://doi.org/10.3390/ma14216404.

[18] Z.C. Sims, O.R. Rios, D. Weiss, P.E.A. Turchi, A. Perron, J.R.I. Lee, T.T. Li, J.A. Hammons, M. Bagge-Hansen, T.M. Willey, K. An, Y. Chen, A.H. King, S.K. McCall, High performance aluminum-cerium alloys for high-temperature applications, Mater Horiz 4 (2017) 1070–1078. https://doi.org/10.1039/c7mh00391a.

[19] W. Wang, Q. Pan, G. Lin, X. Wang, Y. Sun, X. Wang, J. Ye, Y. Sun, Y. Yu, F. Jiang, J. Li, Y. Liu, Microstructure and properties of novel Al-Ce-Sc, Al-Ce-Y, Al-Ce-Zr and Al-Ce-Sc-Y alloy conductors processed by die casting, hot extrusion and cold drawing, J Mater Sci Technol 58 (2020) 155–170. https://doi.org/10.1016/j.jmst.2020.03.073.

[20] D.S. Voroshilov, S.B. Sidelnikov, V.M. Bespalov, R.E. Sokolov, T.V. Bermeshev, V.A. Berngardt, S.N. Lezhnev, A.V. Durnopyanov, A.A. Kovaleva, I.L. Konstantinov, O.S. Novikova, M.M. Motkov, Combined rolling-extrusion of various billets from the Al–Ce–La alloy for electrical wire production, The International Journal of Advanced Manufacturing Technology 131 (2024) 4699–4725. https://doi.org/10.1007/s00170-024-13339-8.

[21] A. E8/E8M, Standard Test Methods for Tension Testing of Metallic Materials, ASTM International (2013).

[22] A. E384-17, Standard Test Method for Microindentation Hardness of Materials, (2016). https://doi.org/10.1520/E0384-17.

[23] F.M. Testing, ASTM Standard E1820-11. Standard Test Method for Measurement of Fracture Toughness, (2009).

[24] S. El-Hadad, M.E. Moussa, M. Shoeib, Influence of Al11Ce3 Size and Distribution on the Electrochemical Properties of Sonoprocessed Al-10 wt.% Ce Alloy, International

Journal of Metalcasting 17 (2023) 1606–1614. https://doi.org/10.1007/s40962-022-00870-1.

[25] Y. Sun, C. Hung, R.J. Hebert, C. Fennessy, S. Tulyani, M. Aindow, Eutectic microstructures in dilute Al-Ce and Al-Co alloys, Mater Charact 154 (2019) 269–276. https://doi.org/10.1016/j.matchar.2019.06.010.

[26] Y. Wang, X. Liang, L. Zeng, H. Wu, H. Li, The microstructure evolution of Al-5Ce alloy prepared by strain-induced melt activation during semi-solid isothermal treatment process, Mater Lett 326 (2022). https://doi.org/10.1016/j.matlet.2022.132948.

[27] C. Zhang, Y. Wang, H. Lv, H. Gao, J. Wang, B. Sun, Enhanced load transfer and ductility in Al–9Ce alloy through heterogeneous lamellar microstructure design by cold rolling and annealing, Materials Science and Engineering: A 821 (2021). https://doi.org/10.1016/j.msea.2021.141591.

[28] I. Basu, V. Ocelík, J.T.M. De Hosson, BCC-FCC interfacial effects on plasticity and strengthening mechanisms in high entropy alloys, Acta Mater 157 (2018) 83–95. https://doi.org/10.1016/J.ACTAMAT.2018.07.031.

[29] G.K. Williamson, R.E. Smallman, III. Dislocation densities in some annealed and cold-worked metals from measurements on the X-ray debye-scherrer spectrum, Philosophical Magazine 1 (1956) 34–46. https://doi.org/10.1080/14786435608238074.

[30] Z. Zribi, H.H. Ktari, F. Herbst, V. Optasanu, N. Njah, EBSD, XRD and SRS characterization of a casting Al-7wt%Si alloy processed by equal channel angular extrusion: Dislocation density evaluation, Mater Charact 153 (2019) 190–198. https://doi.org/10.1016/j.matchar.2019.04.044.

[31] S.C. WANG, Z. ZHU, M.J. STARINK, Estimation of dislocation densities in cold rolled Al-Mg-Cu-Mn alloys by combination of yield strength data, EBSD and strength models, J Microsc 217 (2005) 174–178. https://doi.org/10.1111/j.1365-2818.2005.01449.x.

[32] J.G. Kaufman, Properties of Pure Aluminum, Aluminum Science and Technology (2018) 31–43. https://doi.org/10.31399/ASM.HB.V02A.A0006505.

[33] A.H. Committee, Properties and Selection: Nonferrous Alloys and Special-Purpose Materials, Properties and Selection: Nonferrous Alloys and Special-Purpose Materials (1990). https://doi.org/10.31399/ASM.HB.V02.9781627081627.

[34] 2618 and 2618A: Al-Cu-Mg-Ni Alloys for High-Temperature Service, Properties and Selection of Aluminum Alloys (2019) 328–329. https://doi.org/10.31399/ASM.HB.V02B.A0006616.

[35] C. Weiping, Diffusion of cerium in the aluminium lattice, J Mater Sci Lett 16 (1997) 1824–1826. https://doi.org/10.1023/A:1018572803223/METRICS.

[36] H. Okamoto, Al-Ce (Aluminum-Cerium), J Phase Equilibria Diffus 32 (2011) 392–393. https://doi.org/10.1007/S11669-011-9914-X/TABLES/1.

[37] M.J. Paul, T. Klein, C. Simson, J. Niedermayer, J.J. Kruzic, B. Gludovatz, Strength and fracture resistance of in-situ alloyed compositionally-graded Al-Si processed by dual-wire arc directed energy deposition, Addit Manuf 60 (2022) 103291. https://doi.org/10.1016/j.addma.2022.103291.

[38] S.P. Lynch, R.J.H. Wanhill, R.T. Byrnes, G.H. Bray, Fracture Toughness and Fracture Modes of Aerospace Aluminum–Lithium Alloys, in: Aluminum-Lithium Alloys, Elsevier, 2014: pp. 415–455. https://doi.org/10.1016/B978-0-12-401698-9.00013-6.

[39] R. Gope, S. Mondol, S. Ganguly, A. Mandal, Microstructure and mechanical properties of suction-cast aluminium–cerium alloys, Materials Science and Technology (United Kingdom) 39 (2023) 2824–2841. https://doi.org/10.1080/02670836.2023.2228056.

[40] S. Bolognesi, D. Tong, The Deformation and Ageing of Mild Steel: III Discussion of Results, Proceedings of the Physical Society. Section B 64 (1951) 747. https://doi.org/10.1088/0370-1301/64/9/303.

[41] Z.N. Farhat, Y. Ding, D.O. Northwood, A.T. Alpas, Effect of grain size on friction and wear of nanocrystalline aluminum, Materials Science and Engineering: A 206 (1996) 302–313. https://doi.org/10.1016/0921-5093(95)10016-4.

[42] N. Hansen, X. Huang, Microstructure and flow stress of polycrystals and single crystals, Acta Mater 46 (1998) 1827–1836. https://doi.org/10.1016/S1359-6454(97)00365-0.

[43] H. Mecking, U.F. Kocks, C. Hartig, Taylor factors in materials with many deformation modes, Scr Mater 35 (1996) 465–471. https://doi.org/10.1016/1359-6462(96)00137-6.

[44] M.E. Kassner, Taylor hardening in five-power-law creep of metals and Class M alloys, (n.d.). https://doi.org/10.1016/j.actamat.2003.08.019.

[45] N.Q. Vo, D.C. Dunand, D.N. Seidman, Improving aging and creep resistance in a dilute Al-Sc alloy by microalloying with Si, Zr and Er, (2013). https://doi.org/10.1016/j.actamat.2013.10.008.

Supplementary Information

The grain size and misorientation distributions of samples CE, CE-10 and CE-100 are shown in Fig. S 2.1. The average grain size is reduced significantly due to extrusion, and it does not change upon annealing. The grain size decreases from 582 mm in the AC state to 2.06 ± 0.68 mm in the CE case. Annealing at 300℃ for 10 h and 100 h leads to grain sizes of 2.27 ± 0.75 and 2.99 ± 0.72 mm, respectively, i.e annealing does not modify the grain size within the accuracy of the present measurements. The average misorientation is 28.93º, 26.53º, 26.40º for CE, CE-10 and CE-100, respectively. A tendency is observed for the low angle end of the misorientation distribution to become more pronounced upon annealing. This is associated with the evolution of texture discussed in the article.

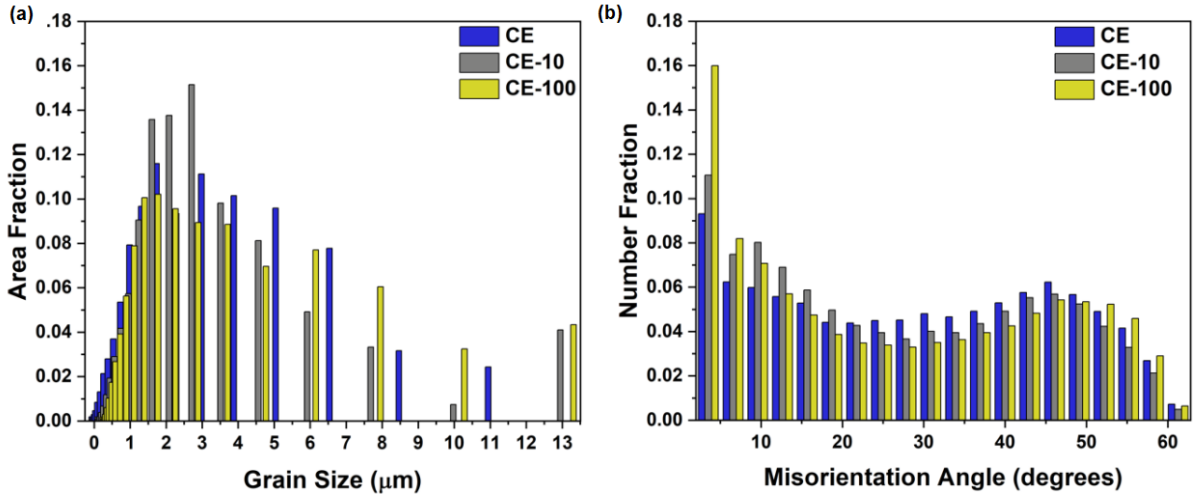

Figure S2.1(a) The grain size distribution and (b) misorientation angle distribution of CE, CE-10 and CE-100 states of the Al-10Ce alloy.

The inverse pole figure, grain size distribution and the misorientation distribution of as-cast samples are shown in Fig. S2.2. The grain size obtained from EBSD maps such as that

shown in Fig. S2.2a is 582 mm. The distribution of grain sizes is shown in Fig. S2.2c. The average misorientation is 11.54º, while the distribution of miorientation angles is shown in Fig. S2.2d. Cast samples are not textured.

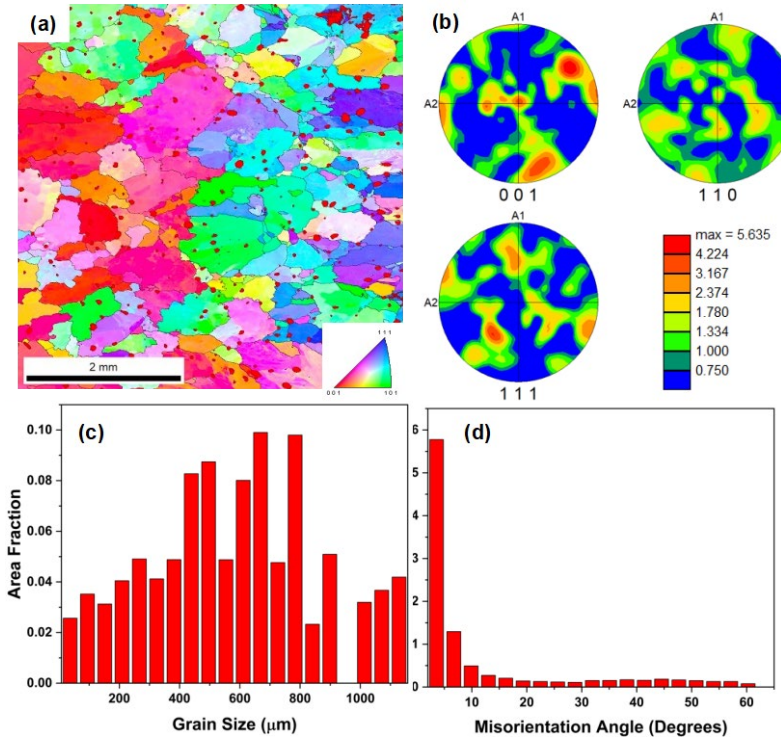

Figure S2.2 (a) Inverse pole figure map, (b) pole figure, (c) grain size distribution and, (d) misorientation distribution of as-cast (AC) Al-10Ce.

The phase maps for the three states are shown in Fig. S2.3. The $Al_{11}Ce_3$ phase volume fraction inferred from these images is 7% in the extruded state and 8.2% and 8.4% after annealing at 300℃ for 10h and 100h, respectively. However, XRD data shown in Fig. 2.1 indicates no change in the height of the peaks corresponding to the intermetallic during annealing. This suggests that the non-monotonic variation obtained from EBSD (Fig. S2.3) is an artifact due to the limited 2D field of view and possibly the error associated with the identification of small precipitates.

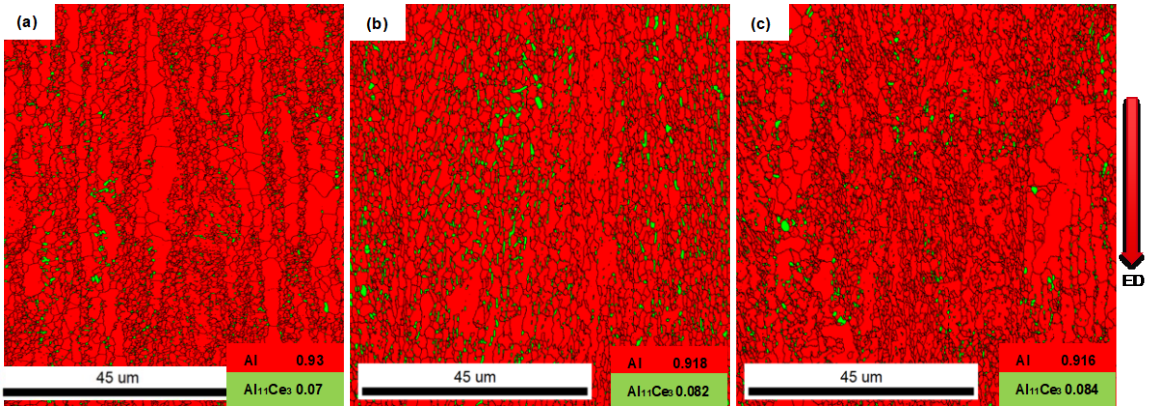

Figure S2.3 The phase maps corresponding to CE, CE-10, and CE-100 condition are shown in (a), (b) and (c), respectively.

The Williamson-Hall plot is shown in Fig, S2.4. It is used to determine the crystallite size and the microstrain for the calculation of the dislocation density.

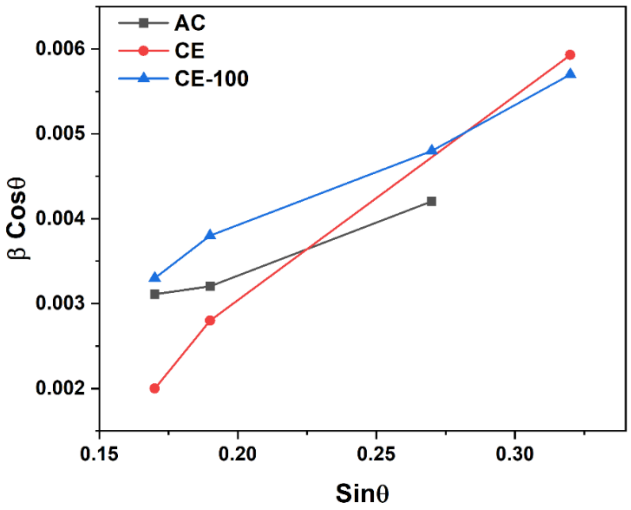

Figure S2.4 The Williamson-Hall plot of AC, CE, and CE-100 condition.

The fracture surfaces of samples subjected to tensile loading were imaged with scanning electron microscopy to understand the mechanisms of failure. Fracture surfaces of as cast and extruded Al-10Ce are shown in Fig. S2.5 (a-f). AC and AC-100 fractographs show many dimples and few cleavage facets (indicated by white circles in Fig. S2.5), while other fracture surfaces show only dimples. The extruded Al-10Ce alloys exhibit deeper and smaller (in projection in the image plane) dimples compared to as cast alloys, as shown in Fig. S2.5(d-f), which indicates that more pronounced plastic deformation took place before

failure in these samples. These observations correlate with the larger strains at failure observed for the extruded samples (22%) as compared to the cast samples (13%).

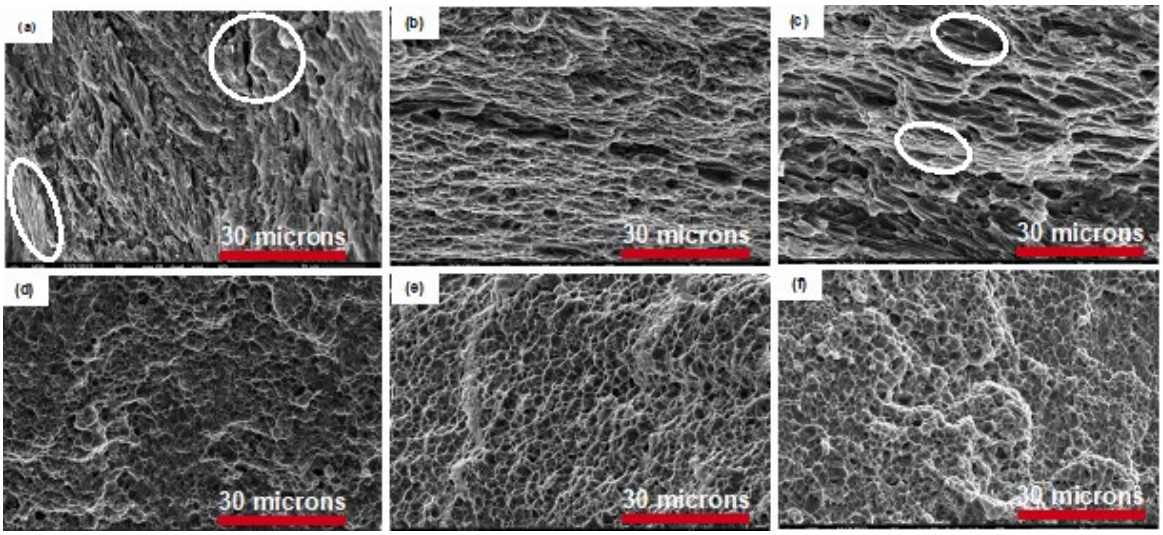

Figure S2.5 Fracture surfaces of the ((a) AC, (b) AC-10, (c) AC-100, (d) CE, (e) CE-10, and (f) CE-100 eutectic Al-10Ce alloy

CHAPTER 3: EFFECT OF THERMOMECHANICAL PROCESSING ON MECHANICAL PROPERTIES AND THE MICROSTRUCTURE OF TERNARY AL-CE-MG ALLOY

Gaurav Singh[1], Humphrey Wara Odhiambo[2], Mohamad Hasan Bin Tasneem[1], Gaoyuan Ouyang[2,3*], Monica A. Soare[4], Min-chul Kang[3], Lin Zhou[3], Jun Cui[2,3], Ralph E. Napolitano[2], Catalin R. Picu[1*]

[1]Department of Mechanical, Aerospace, and Nuclear Engineering, Rensselaer Polytechnic Institute, Troy, NY 12180

[2]Department of Materials Science & Engineering, Iowa State University, Ames, IA 50011

[3]Division of Materials Sciences and Engineering, Ames National Laboratory, Ames, IA 50011

[4]GE Aerospace Research, Niskayuna, NY 12309

Corresponding Authors: Catalin R. Picu (picuc@rpi.edu) & Gaoyuan Ouyang (gaoyuan@iastate.edu)

3.1 ABSTRACT

This work focuses on ternary Al-Ce-Mg alloys which have enhanced mechanical properties retention upon exposure to elevated temperatures, with focus on the effect of extrusion on microstructural refinement and property enhancement. Working with Al-10Ce-4Mg, it is observed that extrusion produces a highly refined microstructure with a twofold increase in strength (tensile strength of 390 MPa at room temperature) relative to the as cast state. We show that the Al-10Ce-4Mg is highly stable upon exposure to elevated temperature (86% strength retention after exposure to 300°C for 100h), far superior to high-temperature grade Al alloy AA2618. The extruded Al-10Ce-4Mg also has room temperature ductility of 15%, as well as fracture toughness of 23 kJ/m^2; the toughness is retained in proportion of 97.6% after exposure to 300°C for 100h. The ratio of the strength at 300°C to the strength at room temperature is 0.4, below the corresponding ratio for the Al-10Ce binary alloy (ratio 0.7) but higher than that of AA2618 (ratio 0.1).

Keywords: Al-Ce-Mg alloy; Mechanical Properties; Microstructure; Fracture toughness; Extrusion.

3.2 Statement of Contribution

The materials presented in this chapter have been submitted to the *Materials Science and Engineering A (MSEA)* journal awaiting publication. My specific contributions to the published work include:

1. Al-Ce alloy design and development
2. Al-Ce-Mg alloy processing design and compositional optimization
3. Microstructural and mechanical characterization, including scanning electron microscopy (SEM), X-ray diffraction (XRD), room-temperature tensile testing, and Vickers microhardness test measurements.

3.3 Introduction

A need exists for light materials with enhanced thermal stability to be used in supersonic aircraft design. The use of Al alloys would provide higher fuel savings, lower CO_2 emissions, and overall increased energy efficiency. However, the use of current Al alloys from the AA2XXX and AA7XXX class, which are precipitate hardened, is impossible as their properties degrade above ~200℃ due to the dissolution and/or coarsening of precipitates[1][2]. In contrast, the Al-Ce intermetallics are highly stable and resistant to coarsening up to at least 350°C [3–6]. This drives the emergence of a new generation of castable Al-Ce alloys with significantly improved high-temperature strength [4,7–11].

Cerium is an inexpensive rare-earth element (REE), which is relatively abundant, and is obtained as a byproduct of the extraction and purification of more valuable REEs, including Li, Pr, Nd, Dy, and Tb [10]. Cerium lacks high-volume applications at present time [10,12]. When added to Al as an alloying element, Ce forms the $Al_{11}Ce_3$ intermetallic, with an eutectic point at 10% Ce [13] (all percentages in wt%). Microstructures with off-eutectic compositions contain a dominant Al (fcc) phase for hypoeutectic, and script-like (or plate-shaped) $Al_{11}Ce_3$ particles in the case of hypereutectic alloys [14–21]. The non-uniform distribution of the intermetallics in the as-cast state leads to sub-optimal strengthening. Nevertheless, Al-Ce alloys in the near-eutectic range (5-15% Ce) exhibit excellent castability and resistance to hot tearing and cracking [22].

Cerium has low diffusivity and solubility in the Al (fcc) phase [15] which implies slow dissolution and Oswald ripening of precipitates at elevated temperatures and hence superior temperature stability of these alloys [6,9]. To benefit from this exceptional behavior,

it would be necessary to ensure high strength and ductility/toughness at room temperature. To this end, a uniform dispersion of fine intermetallics is desirable [23]. This has been achieved by additive manufacturing [5,24] and by thermo-mechanical processing of cast alloys [6,25,26]. Despite significant enhancement of the room temperature yield stress and strength of binary Al-Ce alloys processed by these methods, the performance remains below that of high strength commercial Al alloys. To address this problem, strengthening of the Al matrix has been pursued by alloying to promote either solid solution hardening or precipitation strengthening associated with other alloying elements.

Several studies evaluated the effect of Mg on the microstructural and mechanical properties of cast and additive-manufactured Al-Ce alloy [5,24,27–30]. Hu et al. studied the effect of solid solution strengthening in high-pressure die-casting Al–Ce–Mg alloys. They suggest that the work hardening of Al–8Ce-yMg increases as the Mg content, 'y', increases from 0 wt% to 0.75 wt% [30]. Nam et al. studied ternary alloys (Al-8Ce-10Mg, Al-16Ce-1Mg) produced by additive manufacturing over a wide composition range [5]. Weiss et al. studied the addition of 10% Mg in an Al-8Ce alloy, demonstrating an increase in yield stress from ~50 MPa to ~162 MPa [10]. Forging, rolling, extrusion, high-pressure torsion and equal-channel angular pressing (ECAP), have been used to produce microstructural refinement in metals and alloys and some of these procedures have been also applied to Al-Ce alloys [6,31]. Processing of Al-Ce-Mg alloys by these methods has not been attempted to date. Extrusion has been shown to be effective in refining the microstructure of Al-Ce binary alloys [6].

Since the mechanical properties and thermal stability of the alloy depend on the distribution and morphology of $Al_{11}Ce_3$ intermetallics and on the presence of Mg, in this work we consider cast and extruded Al-10Ce-4Mg alloy. The specific addition of 4 wt% Mg was chosen here for utility in the investigation of thermomechanical processing effects because it provides an opportunity to perform deformation above or below the relevant intermetallic solvus boundaries, within the range of ~290°C to 310°C. For the specific experiments described here, the selected deformation and annealing temperatures are at or just below the t-$Al_{13}CeMg_6$ solvus and just above the metastable b-AlMg solvus. This affords the opportunity to utilize the high dislocation density generated during deformation to stimulate nucleation of fine intermetallics either at this temperature, or upon subsequent

cooling below the b-AlMg solvus. These determinations are based on CALPHAD modeling of Al-Ce-Mg phase equilibria using the assessed parameters reported in [32].

Microstructural characterization is performed using SEM, XRD, EBSD, DSC and HRTEM. Uniaxial tensile testing is performed at ambient and elevated temperatures, as well as in ambient conditions after exposure to elevated temperatures. Fracture toughness testing is performed in ambient conditions, before and after exposure to elevated temperatures. The degree of microstructural refinement retention and thermal stability are evaluated for both cast and extruded states.

3.4 Experimental

3.3.1 Materials and processing

Al-10Ce-4Mg alloys were prepared by mixing Al-Ce and Al-Mg master alloys into molten Al held at 850°C in a graphite crucible, followed by casting into a 25.4 mm diameter graphite mold, preheated to 400°C. The cast rods were hot extruded to a final diameter of 9.5 mm using an Innovare LMS extrusion press. This was done by heating to 300℃, holding isothermally for 30 minutes, extruding through a steel die at an average rate of (96.2 MPa/min) with a maximum pressure of 560 MPa, and forced-air cooling to room temperature. The total reduction during extrusion was 86%, which corresponds to a plastic strain of 1.97. Properties were measured in the as-cast (AC) and cast and extruded (CE) conditions, and also in the corresponding heat-treated conditions (AC-10, AC-100, CE-10, CE-100), where 10 and 100 indicate the number of hours of exposure to 300ºC. Table 1 summarizes the test alloys and conditions considered in this study.

Table 3.1. Materials and conditions considered in the present study.

Naming Convention	**Description**
AC	As cast
CE	Cast and extruded
AC-10	As cast + 300ºC for 10 hours
AC-100	As cast + 300ºC for 100 hours
CE-10	Cast and extruded + 300ºC for 10 hours
CE-100	Cast and extruded + 300ºC for 100 hours

3.3.2 Tensile and fracture toughness experiments

Tensile specimens of 52 mm gauge length for all cast, extruded, and heat-treated conditions were CNC machined per the ASTM E8 standard [33]. An Instron 5969 machine with a 50kN load cell was used for testing under quasi-static conditions ($\dot{\varepsilon} = 3 \times 10^{-4}\ s^{-1}$). Tests were performed at room temperature (25℃) and at elevated temperatures of 150℃, 200℃, 250℃, 300℃ and 350℃. For testing at temperature, samples were heated at $5℃/s$ followed by a 300 s hold after the target temperature was reached and before the beginning of the test. Tensile testing was also performed with the same Instron 5969 machine equipped with a 50 kN load cell at various strain rates ($\dot{\varepsilon} = 3 \times 10^{-2}, 3 \times 10^{-3}, 3 \times 10^{-4}\ and\ 3 \times 10^{-5}\ s^{-1}$).

A microhardness tester (Qness 60M QATM) with a load of 500 g and 15 s dwell time was used for hardness measurements, as per the ASTM E92 standard [34]. Ten measurements were made for each sample condition, and the average values are reported. The elastic-plastic fracture toughness (J_{Ic}) was measured in a single-edge bend test configuration (ASTM E1820 standard) using the Instron frame also employed for uniaxial testing [35]. Sample dimensions were 12 × 6 × 60 mm and the loading span was 50 mm. Fatigue loading with amplitudes of 0.10 to 0.20 kN was performed before the toughness test, such to generate a sharp pre-crack extending for 1.2 mm from the machined notch. The pre-crack and the notch were oriented normal to the extrusion direction. The crack length to sample width ratio was 0.5. The toughness test (static bending) was performed at room temperature with a constant strain rate of $5 \times 10^{-3}\ s^{-1}$.

3.3.3 Microstructure characterization

To prepare samples for XRD and metallographic (SEM/EBSD) analysis, grinding was done with abrasive papers (320, 800, and 1200 grit), after which polishing was performed with cloths containing an abrasive suspension of alumina and colloidal silica, 5 mm to 0.05 mm. XRD was performed with a Panalytical XRD instrument with Cu-K_α radiation, between 20° to 90°, and at a scan rate of 1° per minute. Imaging (for metallography and fractography) was done using a FEI SEM. For this purpose, surfaces were etched with Kellar's reagent for 10 s after polishing. The inspection of fracture surfaces was performed without polishing and etching.

An Oxford SEM microscope was used for EBSD. The EBSD specimens' preparation required additional polished steps using diamond and colloidal silica to minimize surface deformation. The analysis of EBSD images was performed using MTEX software. The mapping is based on the fcc Al and orthorhombic $Al_{11}Ce_3$. Transmission electron microscope (TEM) samples were prepared with a focused ion beam instrument with a gas injection system (Helios, Thermo Fisher Scientific Ltd.) and investigated with an aberration-corrected TEM (Titan Cube, Thermo Fisher Scientific Ltd.) at 200 kV acceleration voltage. STEM-EDS was taken at 200 kV acceleration voltage with 40 pA current.

3.5 Results

3.4.1 Phase analysis

Figure 3.1 shows the normalized XRD spectra for as-cast, as-extruded, and extruded and heat treated Al-10Ce-4Mg. The spectra indicate the presence of the a-Al FCC phase and $Al_{11}Ce_3$ intermetallic phase. Prominent a-Al peaks are (111), (220), (200) and (311) in all material states considered. The intensity of the Al (200) and Al (220) peaks (relative to the Al (111) peak) increases after extrusion (CE) compared with the as cast state (AC), indicating the development of texture. Annealing for 100 h leads to a decrease of the Al (200) and Al (311) peaks which suggests a more random texture in CE-100 compared to CE and CE-10. No evidence of phase transformations taking place during extrusion and heat treatment is obtained. Similar observations have been made in the binary Al-10Ce alloy [6]. No direct evidence of Al-Mg phases is visible in the diffractogram.

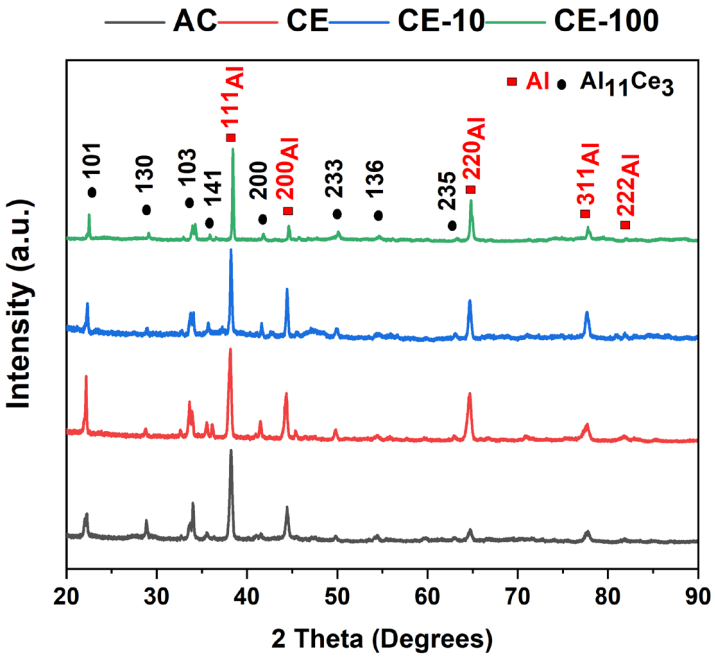

Figure 3.1. XRD of Al-10Ce-4Mg for as cast (AC), extruded (CE), extruded and heat treated at 300ºC for 10 h (CE-10), and 100 h (CE-100).

3.4.2 Microstructural evolution during extrusion and subsequent annealing

3.4.2.1 Scanning electron microscopy

The microstructure of Al-10Ce-4Mg in AC, CE, CE-100 states is shown in Fig. 2(a-c). Two phases are visible in these micrographs: the a-Al (fcc) matrix and the $Al_{11}Ce_3$ intermetallic. No phase containing Mg is visible at this magnification. The as cast micrograph, Fig. 2a, shows the eutectic microstructure commonly observed in the Al-10Ce binary alloy [6]. Extrusion leads to a fine distribution of $Al_{11}Ce_3$ particles in the Al matrix, as shown in Fig. 2b. Particles remain plate-like upon extrusion, but are shorter and become preferentially aligned in the extrusion direction. Phase fractions and phase compositions are statistically identical among the three states shown, indicating thermodynamic stability. In addition, the precipitate sizes are 3.57± 1.56 mm, 1.91 ± 1.12 mm and 2.51± 1.02 mm for AC, CE, and CE-100 states, respectively, showing the refinement from deformation and the resistance to coarsening of the refined structure. The SEM-EDX analysis of CE-100 (Al-10Ce-4Mg) is shown in the Supplementary information (SI), Fig. S1(a-d). This analysis indicates that, with the resolution of this probe (5 nm), Mg is present in solid solution in the a-Al phase and there is no other intermetallic phase present in CE-100; this conclusion is revisited in section 3.3.2.

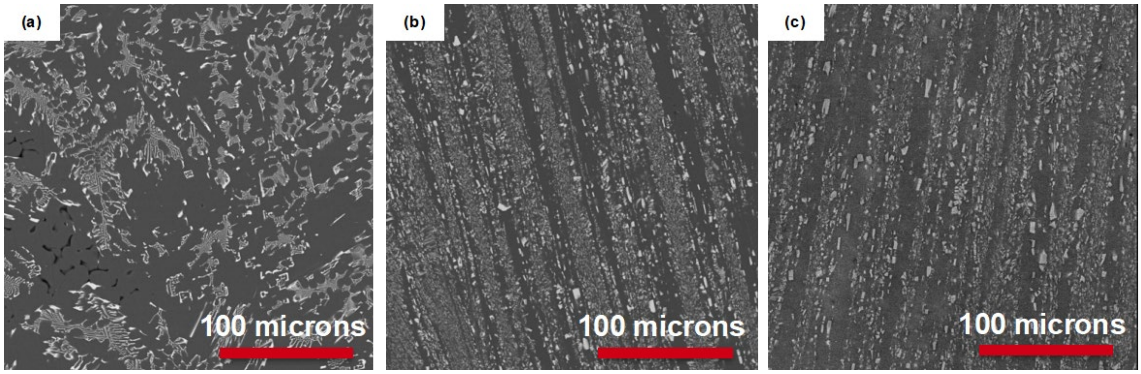

Figure 3.2. The microstructure of Al-10Ce-4Mg (a) AC, (b) CE, (c) CE-100 samples, (black = Al, gray = $Al_{11}Ce_3$).

3.4.2.2 Electron backscattered diffraction

Electron backscattered diffraction (EBSD) provides the grain size, grain misorientation, phase fraction, micro strain, and texture information in the as cast, extruded and heat-treated alloys. EBSD analysis includes the computation of pole figure (PF), inverse pole figure (IPF), and kernel averaged misorientation (KAM). Fig. 3a-c shows EBSD data for as cast Al-10Ce-4Mg. The IPF map in Fig. 3a shows that the microstructure contains primary Al-Mg fcc solid solution phase and $Al_{11}Ce_3$ precipitates. The grain size was measured as 23.56 $\pm$ 0.76 mm. The dendritic structure of the primary phase observed here is similar to that seen in the binary Al-10Ce alloy [6]. The high fraction of primary phase in both cases suggests that the eutectic coupled zone is skewed to higher Ce compositions, as common for faceted-non-faceted eutectics and previously shown experimentally for binary Al-Ce [36]. The phase map in Fig. 3.3b shows the spatial distribution of fcc and $Al_{11}Ce_3$ phases, with a measured area-based intermetallic phase fraction of 0.13. The average precipitates size is 3.57 $\pm$ 1.56 mm, but larger cuboidal precipitates are also present. The average misorientation across grain boundaries is 20.34^o. The KAM map of the cast samples is shown in Fig. 3.3c with an average KAM value of 0.59, which indicates the distribution of microstrain in the as cast state. This information is used to calculate the density of geometrically necessary dislocations later in this section.

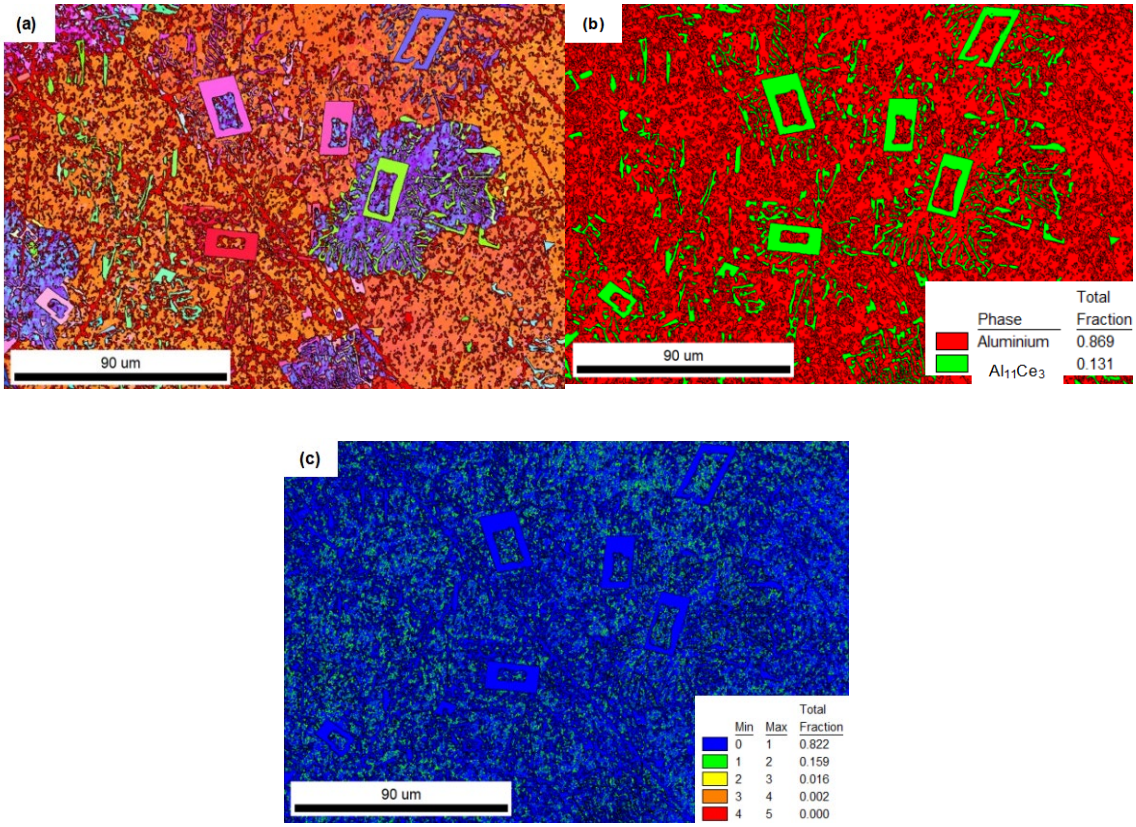

Figure 3.3. EBSD of as-cast Al-10Ce-4Mg (a) IPF map, (b) Phase map (c) KAM map.

Figures 3.4a-c shows the EBSD IPF maps of Al-10Ce-4Mg in the CE, CE-10, and CE-100 conditions. All samples show heterogeneous microstructures, with different grain sizes in different regions: strip-like regions oriented in the extrusion direction, with larger grains also elongated in the extrusion direction, are separated by finer grains. A similar observation has been made for binary Al-Ce in our previous work [6]. The average grain size for (111) oriented grains is 5.6 $\pm$ 2.6 mm, 5.8 $\pm$ 2.6 mm, and 9.2 $\pm$ 7.3 mm for CE, CE-10, and CE-100 conditions, respectively. The average grain size for (101) oriented grains is 7.9 $\pm$ 4.3 mm, 9.8 $\pm$ 6.9 mm, and 8.4 $\pm$ 5.4 mm for CE, CE-10, and CE-100 conditions, respectively. Considering the large relative uncertainty in these measurements, the difference between the two orientations is not statistically significant. Considering now the full population of grain orientations, we compare the average grain size for the three material conditions, yielding values of 7.24 $\pm$ 5.88 mm, 7.08 $\pm$ 6.09 mm, and 10.22 $\pm$ 8.11 mm, for CE, CE-10, and CE-100, respectively, suggesting that high temperature exposure does not modify the grain size to any statistically significant degree. The grain size distribution is shown in SI, Fig. S3.2a.

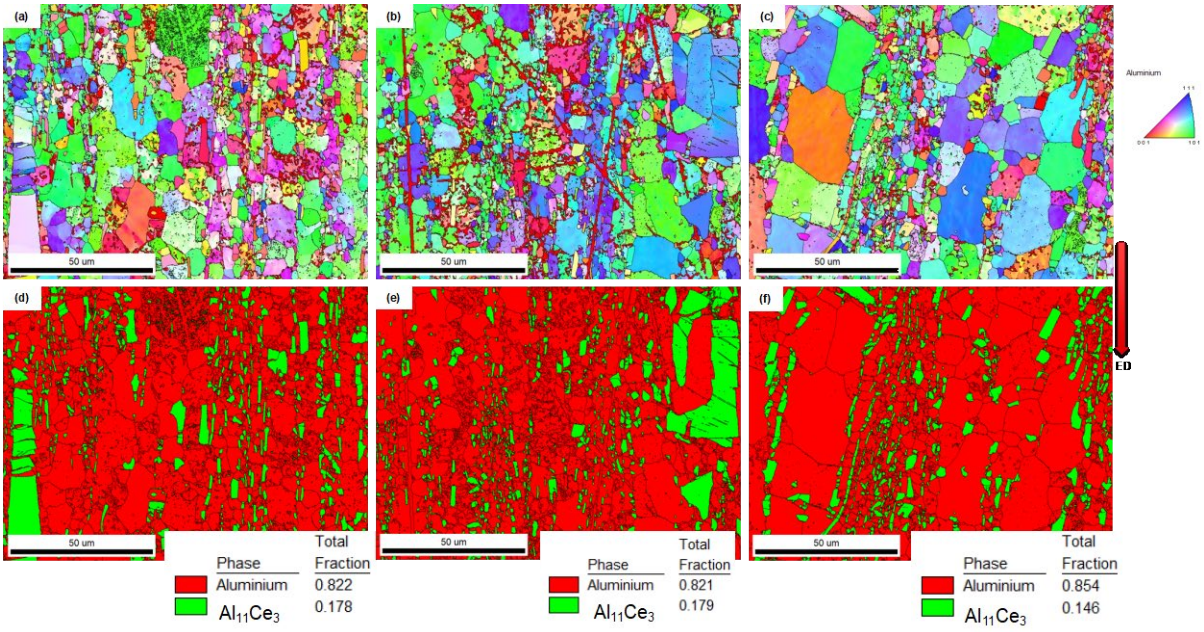

Figure 3.4. IPF maps of Al-10Ce-4Mg in the (a) CE, (b) CE-10, (c) CE-100 states. The phase maps corresponding to panels (a), (b) and (c) are shown in (d), (e) and (f), respectively.

The average dispersoid size is 1.91 ± 1.12, 2.22 ± 1.72, and 2.51± 1.02 mm for CE, CE-10, and CE-100, respectively. Consistent with the grain size measurements, this modest and statistically insignificant variation even after 100 h of annealing suggests reasonable microstructural stability at 300ºC. The average misorientation distribution is 26.57º, 29.06º, 29.82º for CE, CE-10, and CE-100, respectively. The distributions of misorientation are shown in Fig. S3.2b for the three states. Annealing leads to a slight shift of the misorientation distribution to higher angles. The fraction of high-angle grain boundaries (defined as boundaries with misorientation above 15º) is 0.60, 0.63, and 0.65 for CE, CE-10, and CE-100 sample conditions, respectively. The EBSD phase maps for the three states are shown in Fig. 3.4d-f. The $Al_{11}Ce_3$ phase volume fraction inferred from these images is 17.8% in the extruded state and 17.9% and 14.6% after annealing at 300ºC for 10 h and 100 h, respectively.

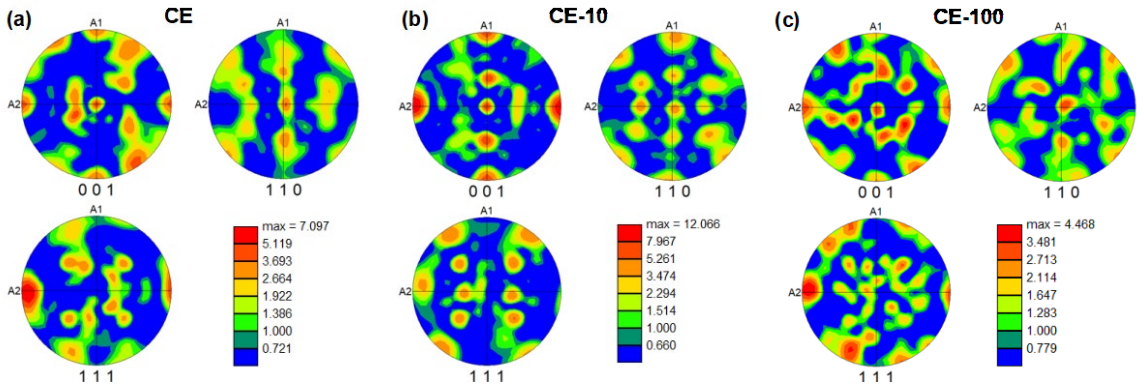

Figure 3.5. Pole figure of (a) CE, (b) CE-10, (c) CE-100 for Al-10Ce-4Mg, A1 is the extrusion direction and A2 is transverse direction.

Figures 3.5a-c show the pole figure map in (001), (110), and (111) projections for CE, CE-10, and CE-100 conditions. Annealing for 10 h increases the intensity of the brass texture ({110}<112>)of CE sample, but the texture becomes somewhat less well defined upon annealing for 100 h. This feature is consistent with the XRD measurements (Fig 3.1), where the intensity of the Al (200) and Al (220) peaks are observed to increase upon extrusion and then to decrease upon annealing for 100 h. This suggests a more random texture in CE-100 compared to CE and CE-10, which is further supported by the pole figure map, Fig. 3.5. Table 3.2 shows the maximum intensity of the pole figure and supports the described texture evolution (enhancement and weakening after 10 h and 100 h annealing, respectively). The influence of these texture variations on mechanical properties is discussed in section 3.3.

EBSD also provides the kernel average misorientation (KAM) values of the CE, CE-10, and CE-100 samples. This information is used to evaluate the dislocation density. The KAM map of CE, CE-10, and CE-100 are shown in Fig. 6a-c. The average KAM value of AC, CE, CE-10, and CE-100 are 0.59°, 0.59°, 0.62°, and 0.55°, respectively. The geometrically necessarily dislocations density, ρ_{GND}, is calculated based on the average KAM value using the strain gradient approach [37]:

$$\rho_{GND} = \frac{2\theta}{n\lambda|b_D|} . \quad (1)$$

Here θ is the experimental KAM value, λ = 1 mm is the step size, n is the number of nearest neighbors averaged in the KAM calculations (here it is 5), and b_D is the Burgers vector of the active slip system (b_D = 0.286 nm). The resulting dislocation density values are reported in Table 3.2. The dislocation density increases upon extrusion, as expected, it is

essentially unchanged upon annealing for 10 h and decreases slightly upon annealing for 100 h. The GNDs depend on the microstructural characteristics, such as grain size, texture, and phase [38,39]. The grain size increase and texture intensity decrease lead to a slight reduction in dislocation density for annealed samples (100 h).

The grain orientation spread (GOS) map is helpful in distinguishing strain-free (recrystallized; GOS ≤ 2°) and deformed grains (GOS > 2°). The GOS maps for the three states are shown in Fig. 3.6d-f. Recrystallization phenomena can be inferred from the GOS value. Recrystallization fractions of CE, CE-10, and CE-100 to be 0.59, 0.62, and 0.73, respectively. It suggests that CE-100 contains more recrystallized grains, which is consistent with the observation of a more random texture (lowest texture intensity, as shown in Fig. 3.5c) upon annealing for longer times.

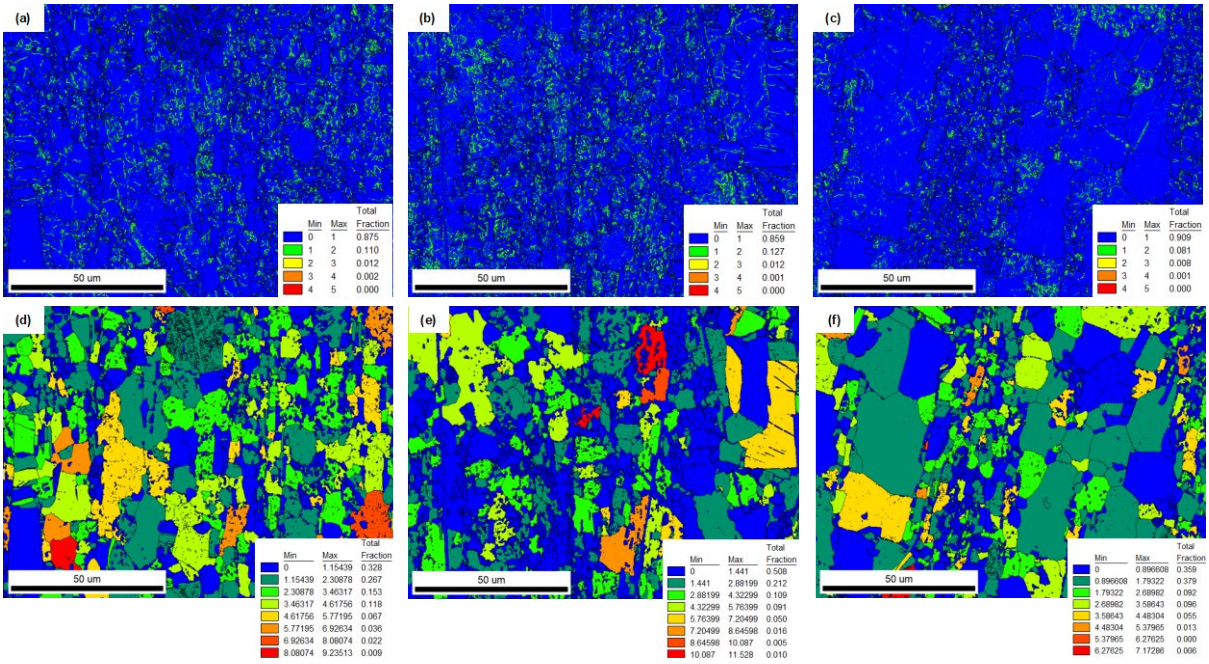

Figure 3.6. KAM maps of Al-10Ce-4Mg in the (a) CE, (b) CE-10, (c) CE-100 states. The GOS maps corresponding to panels (a), (b) and (c) are shown in (d), (e) and (f), respectively.

These results indicate that extrusion produces microstructural refinement (both smaller grains and smaller intermetallic particles), an increase of the dislocation density and the emergence of crystallographic texture. Annealing for 100 h does not substantially affect the mean grain and dispersoid size but decreases slightly the dislocation density and the texture intensity. No microstructural changes are observed upon annealing for 10 h. This

suggests that the annealing time should have some influence on the mechanical properties, which is discussed further in section 3.4.3.

Table 3.2. Mean grain size, maximum texture intensity, and dislocation density (obtained from EBSD, ρ_{GND}) for AC, CE, CE-10, and CE-100 states of the Al-10Ce-4Mg alloy.

	Mean grain size (mm)	**Maximum Texture Intensity (m.r.d.)**	**Main texture component**	**ρ_{GND} EBSD (m^{-2})**
AC	23.56	_	_	$6.92*10^{13}$
CE	7.24	7.10	brass texture ({110}<112>)	$1.4*10^{14}$
CE-10	7.08	12.07	brass texture ({110}<112>)	$1.44*10^{14}$
CE-100	10.22	4.47	brass texture ({110}<112>)	$1.34*10^{14}$

3.4.3 Mechanical properties

3.4.3.1 Mechanical properties of as cast and extruded Al-10Ce-4Mg

The room temperature engineering stress-strain curves of Al-10Ce-4Mg alloy in the AC, AC-10, AC-100 and CE, CE-10, and CE-100 conditions are shown in Fig. 3.7a. All AC samples (including after annealing) have rather poor mechanical properties, with strength below 150 MPa. The extruded (CE) samples have significantly improved properties: the yield stress and tensile strength increase by 2 and 3 times, respectively, while the elongation at failure increases ~5 times, from 3.8% to 17.2%. The simultaneous improvement in strength and ductility is attributed to microstructural refinement, increased uniformity of the distribution of the $Al_{11}Ce_3$ particles and the texture caused by extrusion. Structural refinement includes both the size and shape of the dispersoids, with the shape changing from thin interconnected eutectic lamellae in AC state to rod-like particles of low aspect ratio in the CE state, Fig. 3.4a.

Mechanical properties are slightly reduced by the exposure to 300℃ for both the as cast (AC) and extruded (CE) alloys, which is attributed to the variation of texture. The yield stress, tensile strength, and elongation at break for AC, AC-10, AC-100, CE, CE-10, and CE-

100 states are shown in Table 3.3 The percent retention of the yield stress and tensile strength after annealing for 10 h is 76% and 85%, and after annealing for 100 h is 79%, and 88%.

Table 3.3. Comparison of mechanical properties of binary Al-10Ce, from [6], and ternary Al-10Ce-4Mg in the as cast and extruded states.

	Binary Al-10Ce						**Ternary Al-10Ce-4Mg**					
	AC	**AC-10**	**AC-100**	**CE**	**CE-10**	**CE-100**	**AC**	**AC-10**	**AC-100**	**CE**	**CE-10**	**CE-100**
YS (MPa)	62.3	61.7	59.9	176	195	178	94	65	76	200	152	158
UTS (MPa)	126.7	130.6	135.7	228	251	227	132	102	108	390	332	344
%El	13.4	12.7	12.6	22.0	26.0	26.0	3.8	3.3	5.1	17.2	15.4	18.0

Table 3.3 shows a comparison of the mechanical properties of binary Al-10Ce (from [6]) and ternary Al-10Ce-4Mg alloys in as cast, extruded and heat-treated states. The corresponding stress-strain curves are shown in Fig. S3.3 of the SI. The extruded ternary alloy has much larger strength (390 MPa) compared to the binary alloy extruded in same conditions and to the same reduction (226 MPa), but it has lower strain at failure (17.2% compared with 22% in the binary CE case). The retention of yield stress and tensile strength in the case of the binary alloy is larger than 100% in both CE-10 and CE-100 states. The retention is significantly lower in the ternary case: 76% of the yield stress and 85% of the strength are retained after exposure to 300°C for 10 h, and 79% and 88% of the yield stress and strength are retained after exposure to 300°C for 100 h. The origin of this difference in behavior of the two types of alloys is explored further in section 3.3.2.

Figure 3.7b shows microhardness test results. Each value represents a minimum of 10 measurements with the standard deviation indicated by the error bars. The hardness is 98, 105, 101, 114, 111, and 104 HV for AC, AC-10, AC-100, CE, CE-10, and CE-100, respectively. Both tensile and hardness test results indicate strong property retention upon exposure to elevated temperatures, which is consistent with the microstructure-based observations discussed in the preceding section.

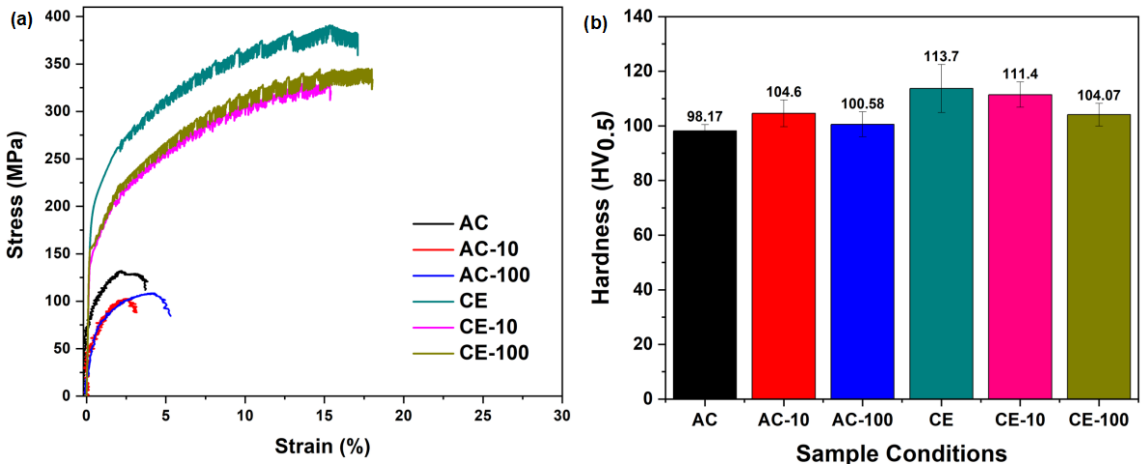

Figure 3.7. (a) Room temperature engineering stress-strain curves of extruded and cast Al-10Ce-4Mg samples tested with a strain rate of $\dot{\varepsilon} = 3 \times 10^{-4}\ s^{-1}$, and (b) hardness measured at room temperature for the same set of samples.

The fracture surfaces of Al-10Ce-4Mg samples were imaged to investigate the failure mechanisms and to correlate with microstructural features; images are shown in Fig. S3. Fracture surfaces of cast samples exhibit many cleavage facets, which indicate brittle failure. The cast samples showed some occasional shrinkage porosity. Fracture surfaces of extruded samples contain dimples which indicates intense plastic deformation during failure. This agrees with the rather large strain at failure of 17% of the extruded samples.

3.4.4 High temperature mechanical properties

Al-10Ce-4Mg samples were further tested at 150℃, 200℃ 250℃, 300℃ and 350℃. The stress-strain curves reported in Fig. 3.8 correspond to the CE state. The yield stress and the strength decrease with increasing temperature, as expected. Strain localization takes place at smaller strains as the temperature increases, while post-critical ductility increases.

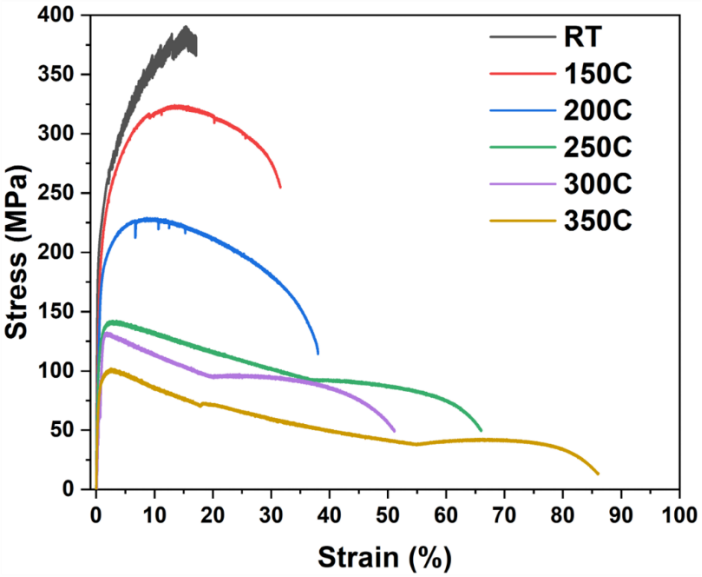

Figure 3.8 Nominal stress-strain curves of Al-10Ce-4Mg in the CE state, at temperatures ranging from room temperature to 350℃.

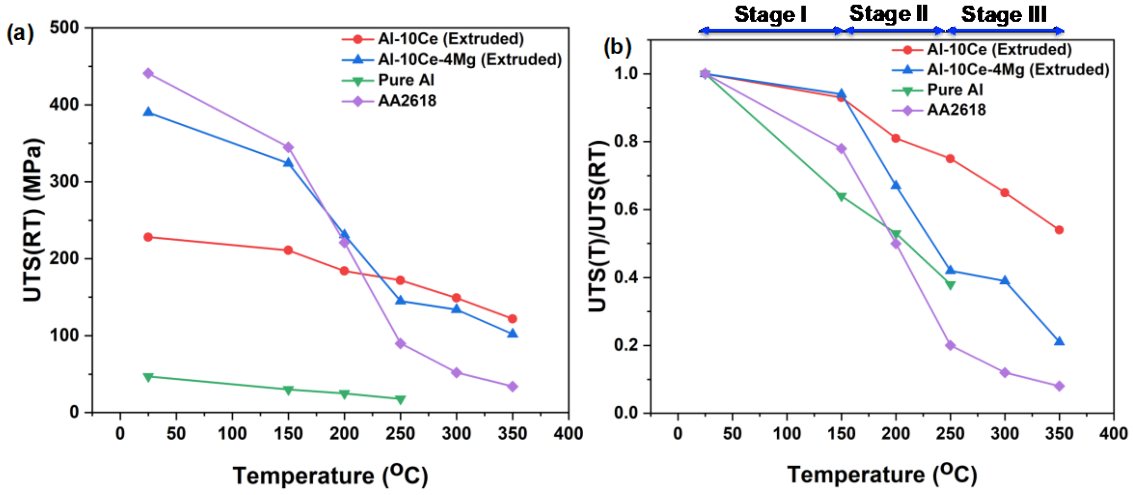

Figure 3.9 (a) Dependence on temperature of the strength (UTS(T)) of Al-10Ce-4Mg in CE state compared with Al-10Ce extruded under same conditions and to the same reduction [6], with pure Al [40,41] and AA2618 [42]. (b) Data in (a) normalized with the room temperature strength, UTS(RT), of the respective materials. Three stages are defined for the Al-10Ce-4Mg curve in (b).

For reference, we compare the temperature resistance of Al-10Ce-4Mg with that of AA2618, which is considered a commercial high temperature Al alloys. Figure 3.9a shows the temperature dependence of the strength (UTS) of Al-10Ce [6] and Al-10Ce-4Mg, both in CE state and subjected to extrusion in the same conditions and to the same reduction,

compared with data for extruded pure Al [40,41] and AA2618 (T61 conditions) [43]. Pure Al and AA2618 lose 80% and 90% of their room temperature strength, respectively, as the test temperature increases to 300℃. The extruded Al-10Ce loses 34% of its room temperature strength under the same conditions, while Al-10Ce-4Mg loses 60%. However, the UTS reduction of the ternary takes place mostly below 250°C, while above this temperature the UTS of the ternary is essentially identical to the UTS of the binary alloy. Hence, the room temperature UTS gain of Al-10Ce-4Mg relative to Al-10Ce is eliminated as the temperature increases to 250°C.

Fig. 3.9b shows the data in Fig. 3.9a normalized by the room temperature strength of the respective materials. The strength of pure Al decreases continuously as temperature increases (primarily in proportion to the reduction of the shear modulus). AA2618 exhibits three regimes: stage I, for T < 150℃ UTS decreases slower than in the pure Al case; stage II, for 150℃ < T < 250℃, UTS decreases fast due to the dissolution of the Al_2Cu q-phase and the increase of solubility of Cu in Al; stage III, for T > 250℃, the softening rate becomes equal to that of pure Al. The binary Al-10Ce alloy exhibits an initial regime, for T < 150℃, where UTS does not decrease with increasing temperature – a behavior reported in [6] for this particular alloy. For T>150℃, UTS decreases at the same rate with pure Al. Yet, the ternary Al-10Ce-4Mg alloy exhibits a behavior that combines features described for Al-10Ce and AA2618. Specifically, UTS is independent of temperature for T < 150℃ (stage I), decreases rapidly in the temperature range 150℃ < T < 250℃ (stage II), after which the decay continues at the rate of Al-10Ce and pure Al (stage III).

These observations suggest the existence of Al-Mg precipitates in Al-10Ce-4Mg which are not discernable by XRD and EBSD. To clarify this issue, we performed TEM, and the results corresponding to a region away from any $Al_{11}Ce_3$ dispersoids are shown in Fig. 3.10. The STEM-HAADF image in Fig. 3.10a shows the presence Al and Mg concentration fluctuations of nano-sized dimensions (~10 nm) – see Figs. 3.10b and 3.10c.

The variation of the UTS of Al-10Ce-4Mg in the temperature range 150℃ < T < 250℃ in which AlMg precipitates dissolve represents approximately 55% of the room temperature UTS value (pure Al softens by approximately 20% in the same temperature range). The DSC scan in Fig. 3.11 confirmed this precipitate dissolution event in Al-10Ce-4Mg sample. Fig. 3.11(b) shows that there is an endothermic event for Al-10Ce-4Mg sample when it is heated. This endothermal event has an onset temperature of 215 ℃. In contrast,

there is no such event in the DSC curves for Al-10Ce, Fig. 3.11a, suggesting that there is no dissolution of precipitates for Al-10Ce up to at least 400 ℃. We infer that AlMg precipitates account for about 55% of the room temperature flow stress. This issue is discussed further in section 3.4.4.

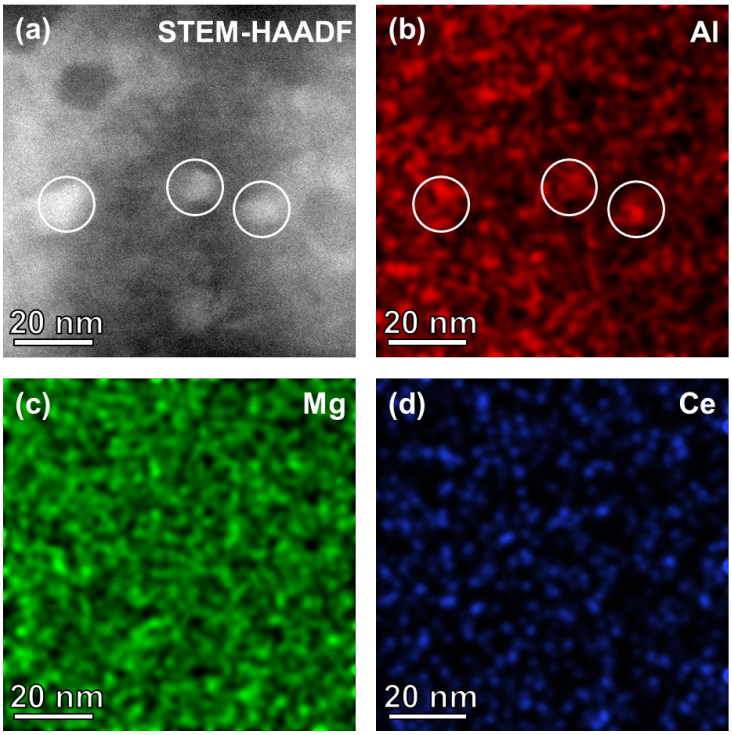

Figure 3.10 STEM HAADF image and EDS map of Al-10Ce-4Mg alloy. (a) STEM-HAADF image of matrix with Al and Mg concentration fluctuations. (b-d) EDS map of (b) Al, (c) Mg, (d) Ce, respectively. The brighter spot in the Al map is Al-rich.

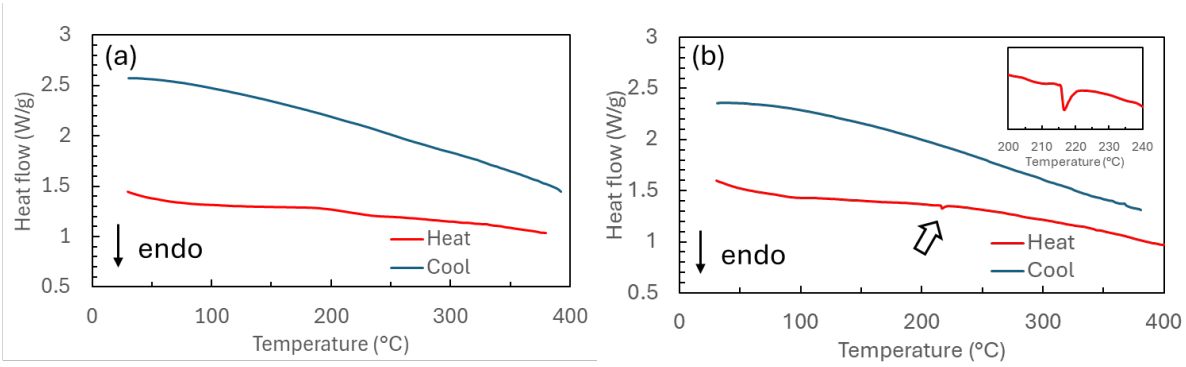

Figure 3.11. DSC curves of (a) Al-10Ce and (b) Al-10Ce-4Mg samples. The inset shows a zoomed in region highlighting the endothermic peak.

3.4.3.1 Strain rate sensitivity of Al-10Ce-4Mg Alloy

The stress-strain curves shown in Fig. 3.8 are serrated, which is a manifestation of the Portevin-LeChatelier (PLC) effect caused by dynamic strain aging (DSA). The occurrence of this phenomenon is well documented in various solid solutions [44–47], including Al-Mg alloys [48–51]. Several mechanisms explaining DSA have been proposed [48,52], all being related to the diffusion of Mg atoms in the vicinity of dislocation cores. Being diffusion-controlled, the mechanisms are temperature dependent. Equivalently, PLC is both temperature and strain rate-dependent and it is common to observe the effect within specific ranges of temperatures and strain rates. To explore it, Al-10Ce-4Mg in the CE state was tested at various strain rates with $\dot{\varepsilon}$ ranging from 10^{-2} to 10^{-5} s^{-1}, and the corresponding stress-strain curves are shown in Fig. 12. The curves are smooth (no PLC) for $\dot{\varepsilon} = 10^{-2}\ s^{-1}$ and $\dot{\varepsilon} = 10^{-5}\ s^{-1}$. Between these limits, the strain rate sensitivity is negative and strain-dependent. At $\dot{\varepsilon} = 10^{-4}\ s^{-1}$, serrations begin beyond an incubation strain of 2%, with the strain rate sensitivity being zero (compare the curves for $\dot{\varepsilon} = 10^{-5}\ s^{-1}$ and $\dot{\varepsilon} = 10^{-4}\ s^{-1}$) for $\varepsilon < 2\%$ and negative for $\varepsilon > 2\%$. The incubation strain decreases as the strain rate increases to $\dot{\varepsilon} = 10^{-3}\ s^{-1}$. The effect of temperature on PLC is visible in Fig. 3.8, where the room temperature stress-strain curve is serrated (PLC), while the curve at 150℃ is smooth (no PLC). The strain rate sensitivity parameter, $m = \partial \log \sigma / \partial \log \dot{\varepsilon}$, was calculated based on the curves in Fig. 3.8 for strains larger than 5%. At $\dot{\varepsilon} = 10^{-4}\ s^{-1}$ and $\dot{\varepsilon} = 10^{-3}\ s^{-1}$, m = -0.03. m increases towards the positive range as the strain rate increases or decreases away from the range shown in Fig. 3.8.

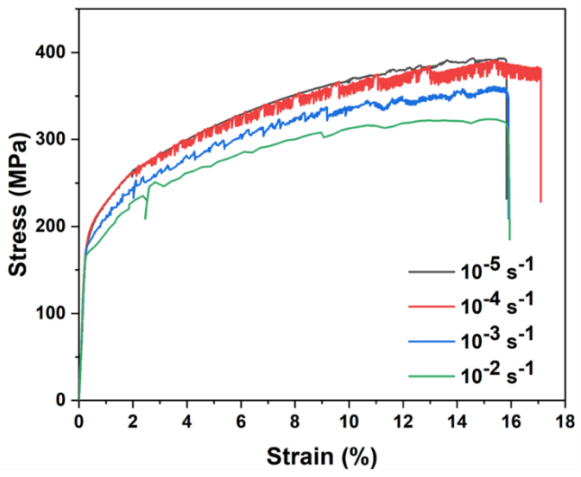

Figure 3.12. Effect of strain rates on engineering stress-strain curves of Al-10Ce-4Mg in CE state tested at room temperature.

3.4.3.2 Fracture toughness of cast and extruded Al-10Ce-4Mg alloys

The fracture toughness was measured using the single-edge bend configuration with load-line displacement method (ASTM-E1820) for the alloy in CE, CE-10 and CE-100 states. [35]. This requires determining the area under the force-displacement curve obtained in a 3-point bend test using a notched (including pre-crack) sample up to the maximum force value. Equations (2) and (3) provide the elastic and plastic components of the energy release rate [35]:

$$J_{el} = \frac{K_Q^2(1-\nu^2)}{E} \ , \tag{2}$$

$$J_{pl} = \frac{\eta_{pl}A_{pl}}{B(W-a_0)} \ , \tag{3}$$

where ν and E are the Poisson's ratio and elastic modulus, and K_Q is the stress intensity factor at fracture. ν and E are taken to be 0.34 and 70 GPa, as per our test results. η_{pl} is taken to be 1.9 per the ASTM E-1820 standard. A_{pl} is the area under the load-displacement curve calculated up to the maximum point. Parameters S, W, B, and a_o are the loading span length, specimen width and thickness, and the notch length, respectively. The critical energy release rate, J_{Ic}, is the sum of Eqs. (2) and (3):

$$J = J_{el} + J_{pl} \tag{4}$$

The load vs. displacement of CE, CE-10, and CE-100 are shown in Fig. 3.13. The ternary extruded and heat-treated samples have toughness values of 20.3 kJ/m^2, 15.5 kJ/m^2, and 24.3 kJ/m^2 for CE. CE-10, and CE-100, respectively. Component J_{pl} (18 kJ/m^2, 13 kJ/m^2, 21 kJ/m^2) is larger than J_{el} (2.3 kJ/m^2, 2.5 kJ/m^2, 3.3 kJ/m^2) since these materials are ductile. The annealed and non-annealed samples show similar fracture toughness which, again, demonstrates the thermal stability of this alloy. These values are comparable with some of the largest fracture toughness values reported for Al alloys, such as for wire-arc DED-processed Al-Si (J_c =36.8 kJ/m^2) [53], Al-Li ($J_c \approx$ 26 kJ/m^2[54] and Al2618 (J_c = 10.34 kJ/m^2) [55].

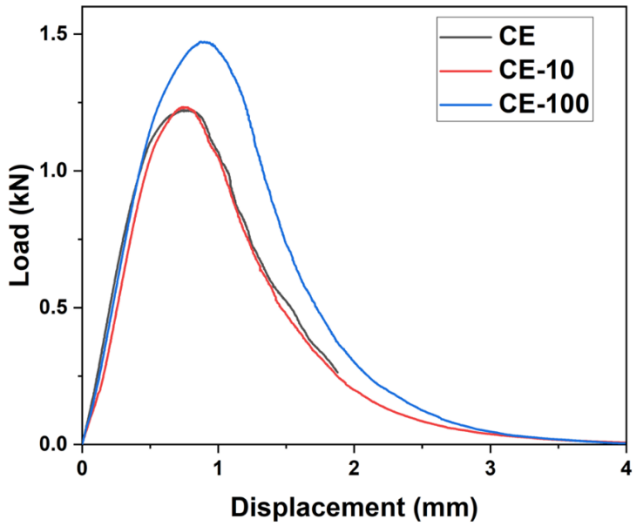

Figure 3.13. Load-displacement curves of notched CE, CE-10 and CE-100 samples loaded in the 3-point bend configuration.

3.4.4 Considerations related to the strengthening mechanisms

Solid solution and grain size strengthening, strain hardening and precipitation strengthening (due to $Al_{11}Ce_3$ and nanoscale AlMg precipitates) are expected to be active strengthening mechanisms in this alloy. Solid solution strengthening is associated with the Mg solute in Al, while Ce has too low solubility in Al to increase the flow stress through this mechanism.

Figure 3.14 shows the yield stress and UTS of as cast and extruded states of binary Al-10Ce [6] and ternary Al-10Ce-4Mg alloys, with the binary alloy being extruded in the same conditions as used here for the ternary. Comparing the stress values provides insight into the contribution to the flow stress of the various mechanisms. Specifically, the effect of microstructural refinement due to extrusion (both grain and dispersoid refinement) emerges by comparing the yield stress of Al-10Ce AC and CE states; this mechanism contributes 114 MPa to the yield stress. Same processing conditions applied to Al-10Ce-4Mg lead to similar refinement and an increase of the yield stress of 106 MPa, consistent with the value for the equivalent binary alloy. Comparing the yield stress of Al-10Ce and Al-10Ce-4Mg both in the AC state, indicates that the addition of Mg contributes only 32 MPa to the yield stress.

Comparing the yield stress with UTS sheds light on the strain hardening ability of the material. The ability of the binary alloy to strain harden is limited (65 MPa and 52 MPa in the AC and CE states). However, the ternary alloy in the CE state strain hardens by 190 MPa. This much larger strain hardening effect, compared with the binary alloy, can be attributed to the influence of a fine dispersion of AlMg nanoscale precipitates, which correlates with the TEM observations shown in Fig. 3.10.

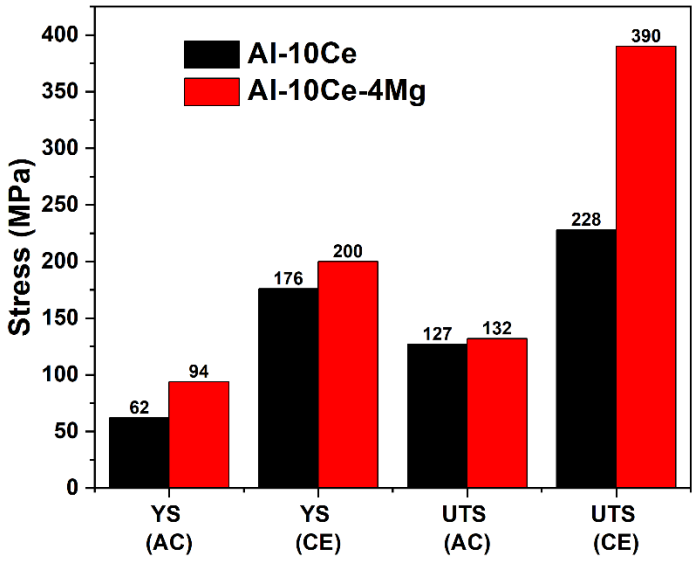

Figure 3.14. Yield stress and UTS of Al-10Ce (data from [6]) and Al-10Ce-4Mg in as cast (AC) and extruded (CE) states. Values of these stresses (in MPa) are shown above the bars.

3.6 Conclusion

The effect of extrusion on the microstructure and mechanical properties of Al-10Ce-4Mg is evaluated in this work in conjunction with the material's ability to retain properties upon exposure to elevated temperatures. The as-cast alloy has large grain size and relatively low yield stress and strength, while the effect of Mg in Al-Ce is not profound in cast condition. Significant microstructural refinement is observed upon extrusion which leads to both grain size reduction and a decrease of the size of $Al_{11}Ce_3$ intermetallics. Extrusion leads to larger yield stress, ultimate tensile strength, and elongation at failure by factors of 2.5, 2.5, and 10, respectively. These properties are largely preserved after annealing at 300ºC for up to 100 h. The toughness is also preserved upon annealing at 300ºC for up to 100 h. The strength at elevated temperatures decreases relative to the room temperature strength, with a rapid decrease in the 150℃ to 250℃ range. This is attributed to the dissolution of nanoscale AlMg precipitates which have been identified in the extruded alloy. The ratio of the UTS at 300℃

to the room temperature UTS is 0.39, lower than that of the equivalent binary alloy, Al-10Ce (ratio 0.65), but larger than the high temperature commercial alloy AA2618 (ratio 0.1). The study shows that adequate thermomechanical processing and associated microstructural refinement render these alloys potentially useful in applications requiring resistance to elevated temperatures.

Acknowledgement

This work was supported by the US Department of Energy (DOE) through Grant No. DE-EE0010219

Data availability: The data resulting from this investigation is included in the article.

3.7 References

[1] Y.H. Gao, C. Yang, J.Y. Zhang, L.F. Cao, G. Liu, J. Sun, E. Ma, Stabilizing nanoprecipitates in Al-Cu alloys for creep resistance at 300°C, Mater Res Lett 7 (2019) 18–25. https://doi.org/10.1080/21663831.2018.1546773.

[2] S. Mondol, T. Alam, R. Banerjee, S. Kumar, K. Chattopadhyay, Development of a high temperature high strength Al alloy by addition of small amounts of Sc and Mg to 2219 alloy, Materials Science and Engineering: A 687 (2017) 221–231. https://doi.org/10.1016/J.MSEA.2017.01.037.

[3] Y. Guo, J. Hu, Q. Han, B. Sun, J. Wang, C. Liu, Microstructure diversity dominated by the interplay between primary intermetallics and eutectics for Al-Ce heat-resistant alloys, J Alloys Compd 899 (2022). https://doi.org/10.1016/j.jallcom.2021.162914.

[4] S. Shen, C. Wu, Y. Li, Y. Huang, W. Huang, P. Zhang, S. Zhong, Y. Lu, G. Luo, Z. Gan, J. Liu, Refining mechanism and elevated-temperature mechanical properties of Al-Ce alloys solidified under super gravity field, Materials Science and Engineering: A 879 (2023). https://doi.org/10.1016/j.msea.2023.145191.

[5] S. Nam, E. Simsek, N. Argibay, O. Rios, H.B. Henderson, D. Weiss, E.E. Moore, A.P. Perron, S.K. McCall, R.T. Ott, Strength mechanisms and tunability in Al-Ce-Mg ternary alloys enabled by additive manufacturing, Mater Des 231 (2023) 112009. https://doi.org/10.1016/j.matdes.2023.112009.

[6] G. Singh, H.W. Odhiambo, M.H. Bin Tasneem, G. Ouyang, M.A. Soare, J. Cui, R.E. Napolitano, C.R. Picu, Effect of thermomechanical processing on mechanical properties and the microstructure of binary Al-Ce alloy, Materials Science and Engineering: A 916 (2024) 147395. https://doi.org/10.1016/j.msea.2024.147395.

[7] B. Stojanovic, M. Bukvic, I. Epler, Application of Aluminum and Aluminum alloys in engineering, Applied Engineering Letters 3 (2018) 2466–4847. https://doi.org/10.18485/aeletters.2018.3.2.2.

[8] Z.C. Sims, D. Weiss, S.K. McCall, M.A. McGuire, R.T. Ott, T. Geer, O. Rios, P.A.E. Turchi, Cerium-Based, Intermetallic-Strengthened Aluminum Casting Alloy: High-Volume Co-product Development, JOM 68 (2016) 1940–1947. https://doi.org/10.1007/s11837-016-1943-9.

[9] S. El-Hadad, M.E. Moussa, E. Riedel, M. Ahmed, R. Bähr, A. Nofal, Solidification Processing of Al-Ce Alloys for High-Temperature Applications, in: INALCO 2023, MDPI, Basel Switzerland, 2023: p. 17. https://doi.org/10.3390/engproc2023043017.

[10] D. Weiss, Improved High-Temperature Aluminum Alloys Containing Cerium, J Mater Eng Perform 28 (2019) 1903–1908. https://doi.org/10.1007/s11665-019-3884-2.

[11] Z. Huda, P. Edi, Materials selection in design of structures and engines of supersonic aircrafts: A review, Materials & Design (1980-2015) 46 (2013) 552–560. https://doi.org/10.1016/J.MATDES.2012.10.001.

[12] F. Czerwinski, Cerium in aluminum alloys, Journal of Materials Science 2019 55:1 55 (2019) 24–72. https://doi.org/10.1007/S10853-019-03892-Z.

[13] Z.C. Sims, O.R. Rios, D. Weiss, P.E.A. Turchi, A. Perron, J.R.I. Lee, T.T. Li, J.A. Hammons, M. Bagge-Hansen, T.M. Willey, K. An, Y. Chen, A.H. King, S.K. McCall, High performance aluminum-cerium alloys for high-temperature applications, Mater Horiz 4 (2017) 1070–1078. https://doi.org/10.1039/c7mh00391a.

[14] A.E. Perrin, R.A. Michi, D.N. Leonard, K.D. Sisco, A.J. Plotkowski, A. Shyam, J.D. Poplawsky, L.F. Allard, Y. Yang, Effect of Mn on eutectic phase equilibria in Al-rich Al-Ce-Ni alloys, J Alloys Compd 965 (2023). https://doi.org/10.1016/j.jallcom.2023.171455.

[15] H. Okamoto, Al-Ce (Aluminum-Cerium), J Phase Equilibria Diffus 32 (2011) 392–393. https://doi.org/10.1007/S11669-011-9914-X/TABLES/1.

[16] Z. Cao, G. Kong, C. Che, Y. Wang, H. Peng, Experimental investigation of eutectic point in Al-rich Al-La, Al-Ce, Al-Pr and Al-Nd systems, Journal of Rare Earths 35 (2017) 1022–1028. https://doi.org/10.1016/S1002-0721(17)61008-1.

[17] K. Dai, J. Ye, Z. Wang, J. Chen, C. He, K. Xiong, Beneficial Utilization of Electromagnetic Stirring Technology in Al-Ce Alloys, JOM 75 (2023) 2788–2798. https://doi.org/10.1007/s11837-023-05904-5.

[18] Y. Sun, C. Hung, R.J. Hebert, C. Fennessy, S. Tulyani, M. Aindow, Eutectic microstructures in dilute Al-Ce and Al-Co alloys, Mater Charact 154 (2019) 269–276. https://doi.org/10.1016/j.matchar.2019.06.010.

[19] J.R. Kozakevich, J. Stroh, D. Sediako, D. Weiss, Solidification Kinetics of an Al-Ce Alloy with Additions of Ni and Mn, Metals (Basel) 13 (2023). https://doi.org/10.3390/met13050955.

[20] J. Ye, K. Dai, M. Gao, J. Chen, R. Guan, Primary phase transformation mechanism in a hypereutectic Al-Ce alloy during rapid solidification, Mater Lett 340 (2023). https://doi.org/10.1016/j.matlet.2023.134172.

[21] S.O. Rogachev, E.A. Naumova, Thermal Stability of Al-Ca and Al-Ce Alloys Obtained by High-Pressure Torsion, J Mater Eng Perform 30 (2021) 9192–9199. https://doi.org/10.1007/s11665-021-06105-4.

[22] A. Plotkowski, K. Sisco, S. Bahl, A. Shyam, Y. Yang, L. Allard, P. Nandwana, A.M. Rossy, R.R. Dehoff, Microstructure and properties of a high temperature Al–Ce–Mn alloy produced by additive manufacturing, Acta Mater 196 (2020) 595–608. https://doi.org/10.1016/j.actamat.2020.07.014.

[23] S.O. Rogachev, E.A. Naumova, E.A. Lukina, A. V. Zavodov, V.M. Khatkevich, High strength Al–La, Al–Ce, and Al–Ni eutectic aluminum alloys obtained by high-pressure torsion, Materials 14 (2021). https://doi.org/10.3390/ma14216404.

[24] K. Sisco, A. Plotkowski, Y. Yang, D. Leonard, B. Stump, P. Nandwana, R.R. Dehoff, S.S. Babu, Microstructure and properties of additively manufactured Al–Ce–Mg alloys, Sci Rep 11 (2021) 6953. https://doi.org/10.1038/s41598-021-86370-4.

[25] A.D. D'Souza, S.S. Rao, M.A. Herbert, Assessment of influence of process parameters on properties of friction stir welded Al-Ce-Si-Mg aluminium alloy, Mater Res Express 6 (2019). https://doi.org/10.1088/2053-1591/ab1aec.

[26] C. Zhang, Y. Wang, H. Lv, H. Gao, J. Wang, B. Sun, Enhanced load transfer and ductility in Al–9Ce alloy through heterogeneous lamellar microstructure design by cold rolling and annealing, Materials Science and Engineering: A 821 (2021). https://doi.org/10.1016/j.msea.2021.141591.

[27] F. Czerwinski, B. Shalchi Amirkhiz, Aluminum Cast Alloys Based on the Al–Ce–Si–Mg System: An Influence of Silicon on Crystallization, Phase Composition, and Tensile Properties, Metallurgical and Materials Transactions A 53 (2022) 4233–4246. https://doi.org/10.1007/s11661-022-06812-0.

[28] J. Gröbner, D. Kevorkov, R. Schmid-Fetzer, Thermodynamic modeling of Al–Ce–Mg phase equilibria coupled with key experiments, Intermetallics (Barking) 10 (2002) 415–422. https://doi.org/10.1016/S0966-9795(02)00018-3.

[29] H. Lv, P. Peng, T. Feng, H. Gao, J. Ju, B. Wang, J. Wang, B. Sun, High-performance co-continuous Al-Ce-Mg alloy with in-situ nano-network structure fabricated by laser powder bed fusion, Addit Manuf 60 (2022) 103218. https://doi.org/10.1016/j.addma.2022.103218.

[30] B. Hu, B. Quan, D. Li, X. Wang, Z. Li, X. Zeng, Solid solution strengthening mechanism in high pressure die casting Al–Ce–Mg alloys, Materials Science and Engineering: A 812 (2021) 141109. https://doi.org/10.1016/j.msea.2021.141109.

[31] Y. Wang, X. Liang, L. Zeng, H. Wu, H. Li, The microstructure evolution of Al-5Ce alloy prepared by strain-induced melt activation during semi-solid isothermal treatment process, Mater Lett 326 (2022). https://doi.org/10.1016/j.matlet.2022.132948.

[32] E.E. Moore, P.E.A. Turchi, V. Lordi, D. Weiss, Z.C. Sims, H.B. Henderson, M.S. Kesler, O. Rios, S.K. McCall, A. Perron, Thermodynamic Modeling of the Al-Ce-Cu-Mg-Si

System and Its Application to Aluminum-Cerium Alloy Design, J Phase Equilibria Diffus 41 (2020) 764–783. https://doi.org/10.1007/s11669-020-00852-y.

[33] A. E8/E8M, Standard Test Methods for Tension Testing of Metallic Materials, ASTM International (2013).

[34] A. E384-17, Standard Test Method for Microindentation Hardness of Materials, (2016). https://doi.org/10.1520/E0384-17.

[35] F.M. Testing, ASTM Standard E1820-11. Standard Test Method for Measurement of Fracture Toughness, (2009).

[36] H. Jones, Some effects of solidification kinetics on microstructure formation in aluminium-base alloys, Materials Science and Engineering: A 413–414 (2005) 165–173. https://doi.org/10.1016/j.msea.2005.08.190.

[37] I. Basu, V. Ocelík, J.T.M. De Hosson, BCC-FCC interfacial effects on plasticity and strengthening mechanisms in high entropy alloys, Acta Mater 157 (2018) 83–95. https://doi.org/10.1016/J.ACTAMAT.2018.07.031.

[38] M. Kamaya, Assessment of local deformation using EBSD: Quantification of local damage at grain boundaries, Mater Charact 66 (2012) 56–67. https://doi.org/10.1016/j.matchar.2012.02.001.

[39] S.J. Sun, Y.Z. Tian, H.R. Lin, Z.J. Wang, Z.F. Zhang, Revisiting the role of prestrain history in the mechanical properties of ultrafine-grained CoCrFeMnNi high-entropy alloy, Materials Science and Engineering: A 801 (2021) 140398. https://doi.org/10.1016/j.msea.2020.140398.

[40] J.G. Kaufman, Properties of Pure Aluminum, Aluminum Science and Technology (2018) 31–43. https://doi.org/10.31399/ASM.HB.V02A.A0006505.

[41] A.H. Committee, Properties and Selection: Nonferrous Alloys and Special-Purpose Materials, Properties and Selection: Nonferrous Alloys and Special-Purpose Materials (1990). https://doi.org/10.31399/ASM.HB.V02.9781627081627.

[42] 2618 and 2618A: Al-Cu-Mg-Ni Alloys for High-Temperature Service, Properties and Selection of Aluminum Alloys (2019) 328–329. https://doi.org/10.31399/ASM.HB.V02B.A0006616.

[43] 2618 and 2618A: Al-Cu-Mg-Ni Alloys for High-Temperature Service, Properties and Selection of Aluminum Alloys (2019) 328–329. https://doi.org/10.31399/ASM.HB.V02B.A0006616.

[44] A. van den Beukel, Theory of the effect of dynamic strain aging on mechanical properties, Physica Status Solidi (a) 30 (1975) 197–206. https://doi.org/10.1002/pssa.2210300120.

[45] L.P. Kubin, Y. Estrin, Evolution of dislocation densities and the critical conditions for the Portevin-Le Châtelier effect, Acta Metallurgica et Materialia 38 (1990) 697–708. https://doi.org/10.1016/0956-7151(90)90021-8.

[46] P.G. McCormick, Y. Estrin, Transient flow behaviour associated with dynamic strain ageing, Scripta Metallurgica 23 (1989) 1231–1234. https://doi.org/10.1016/0036-9748(89)90332-3.

[47] R.A. Mulford, U.F. Kocks, New observations on the mechanisms of dynamic strain aging and of jerky flow, Acta Metallurgica 27 (1979) 1125–1134. https://doi.org/10.1016/0001-6160(79)90130-5.

[48] H. Fujita, T. Tabata, Discontinuous deformation in Al-Mg alloys under various conditions, Acta Metallurgica 25 (1977) 793–800. https://doi.org/10.1016/0001-6160(77)90094-3.

[49] J. Balík, P. Lukáč, Portevin-Le chatelier instabilities in Al-3 Mg conditioned by strain rate and strain, Acta Metallurgica et Materialia 41 (1993) 1447–1454. https://doi.org/10.1016/0956-7151(93)90253-O.

[50] R.C. Picu, G. Vincze, F. Ozturk, J.J. Gracio, F. Barlat, A.M. Maniatty, Strain rate sensitivity of the commercial aluminum alloy AA5182-O, Materials Science and Engineering: A 390 (2005) 334–343. https://doi.org/10.1016/j.msea.2004.08.029.

[51] A. Bintu, G. Vincze, R.C. Picu, A.B. Lopes, Effect of symmetric and asymmetric rolling on the mechanical properties of AA5182, Mater Des 100 (2016) 151–156. https://doi.org/10.1016/j.matdes.2016.03.123.

[52] R.C. Picu, A mechanism for the negative strain-rate sensitivity of dilute solid solutions, Acta Mater 52 (2004) 3447–3458. https://doi.org/10.1016/j.actamat.2004.03.042.

[53] M.J. Paul, T. Klein, C. Simson, J. Niedermayer, J.J. Kruzic, B. Gludovatz, Strength and fracture resistance of in-situ alloyed compositionally-graded Al-Si processed by dual-wire arc directed energy deposition, Addit Manuf 60 (2022) 103291. https://doi.org/10.1016/j.addma.2022.103291.

[54] S.P. Lynch, R.J.H. Wanhill, R.T. Byrnes, G.H. Bray, Fracture Toughness and Fracture Modes of Aerospace Aluminum–Lithium Alloys, in: Aluminum-Lithium Alloys, Elsevier, 2014: pp. 415–455. https://doi.org/10.1016/B978-0-12-401698-9.00013-6.

[55] E. Gariboldi, D. Ripamonti, L. Signorelli, G. Vimercati, F. Casaro, Fracture toughness and microstructure in AA 2XXX Aluminum alloys, Metallurgical Science and Tecnology 25 (2007).

Supplementary Information

The SEM-EDX analysis of CE-100 (Al-10Ce-4Mg) is shown in Fig. S1(a-d). This analysis indicates that, with the resolution of this probe (5 nm), Mg is present in solid solution in the a-Al FCC phase. This conclusion is revisited in section 3.3.2. The grain size distribution is shown in Fig. S2a. The average grain size in the CE state is 7.24 ± 5.88 mm. CE-10 and CE-100 have average grain sizes of 7.08 ± 6.09 mm and 10.22 ± 8.11 mm, respectively, and essentially indistinguishable distributions, i.e. annealing does not modify the grain size within the accuracy of the present measurements.

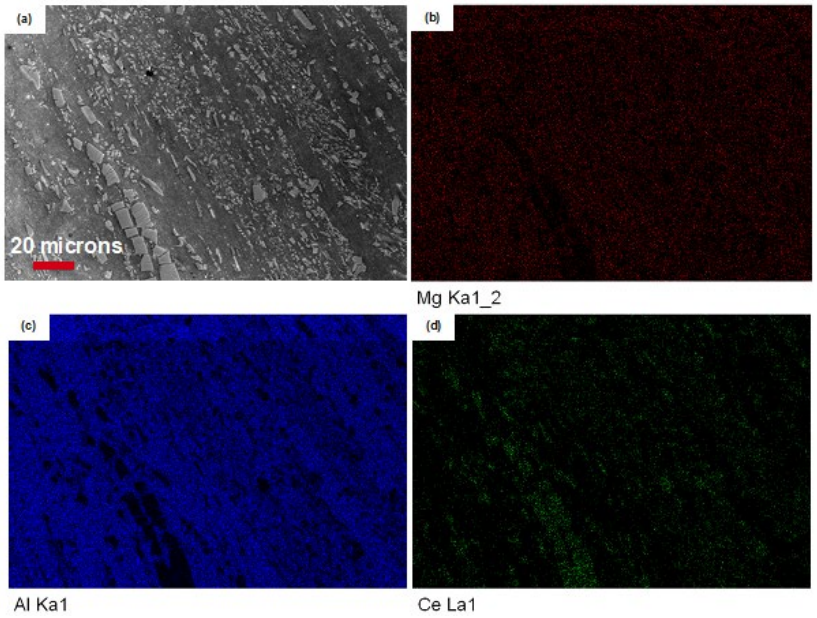

Figure S3.1(a) The SEM microstructure of CE-100, and elemental mapping of (b) Magnesium, (c) Aluminum, (d) Cerium in the microstructure shown in (a).

The distributions of misorientations are shown in Fig. S2b for the three material states. Annealing leads to a slight shift of the misorientation distribution to higher angles. The average misorientation is 26.57º, 29.06º, 29.82º for CE, CE-10, and CE-100, respectively.

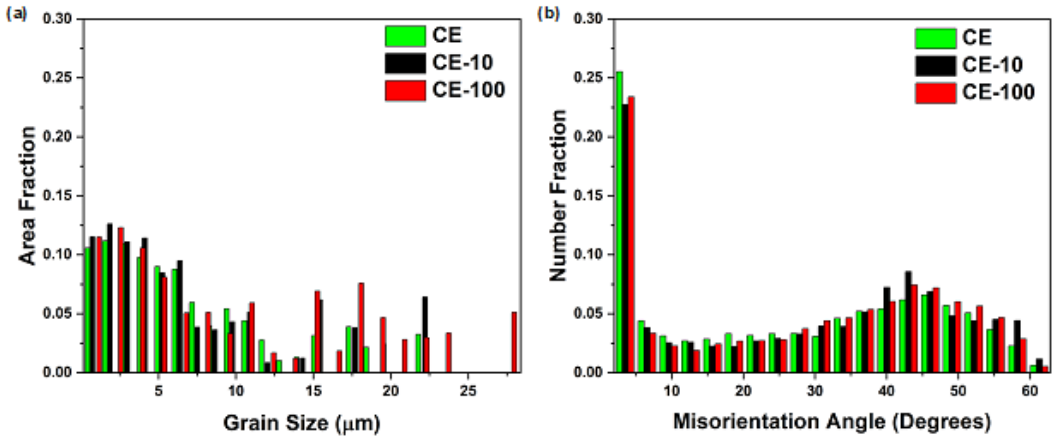

Figure S3.2 (a) Grain size distribution and (b) misorientation angle distribution of as-extruded, extruded and annealed Al-10Ce-4Mg samples at 300℃ for 10 h and 100 h.

A comparison of mechanical properties of ternary Al-10Ce-4Mg and binary Al-10Ce (from [1]) in cast and extruded states in shown in Fig. S3. The figure shows room temperature engineering stress-strain curves before and after annealing. The ternary alloy has much larger flow stress and strength compared with the binary: the strength of the ternary

alloy is 390 MPa, while the strength of the binary alloy extruded under same conditions and to the same reduction is 226 MPa. The ductility of the ternary alloy is 17%, while that of the binary alloy is 22%.

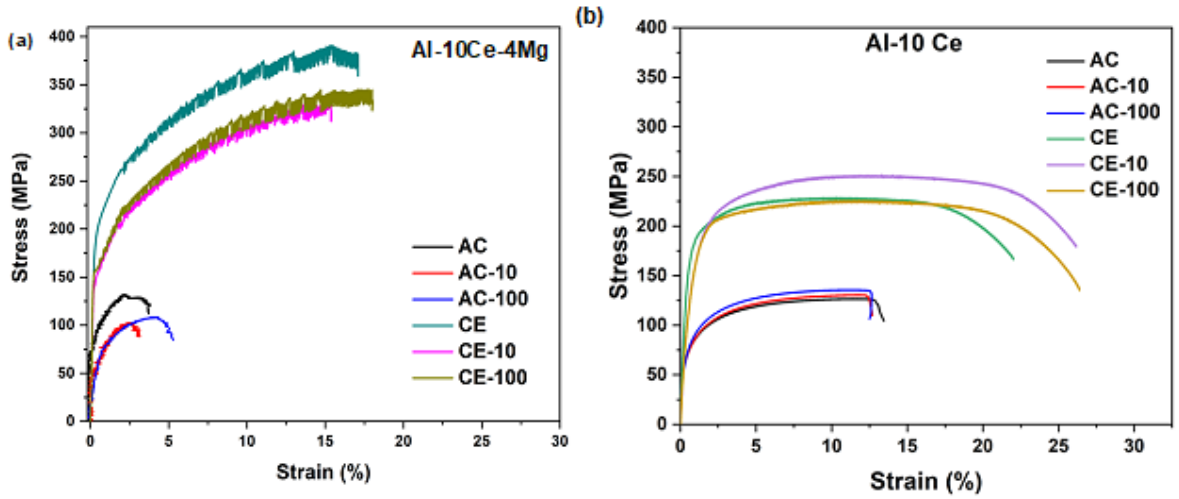

Figure S3.3 Engineering stress-strain curves of extruded and cast (a) Al-10Ce-4Mg and (b) Al-10Ce (data from [1]) samples, before and after annealing for 10 h and 100 h. All tests performed with a strain rate of 10^{-4} s^{-1}. The curves in (a) are averages of 3 samples for each reported state.

Fracture surfaces of samples subjected to tensile loading were imaged with SEM to investigate the mechanisms of failure and correlate with microstructural features. These images are shown in Fig. S4. Fracture surfaces of cast samples exhibit cleavage facets, while those of extruded samples show only dimples. The small dimple size indicates that intense plastic deformation took place during failure.

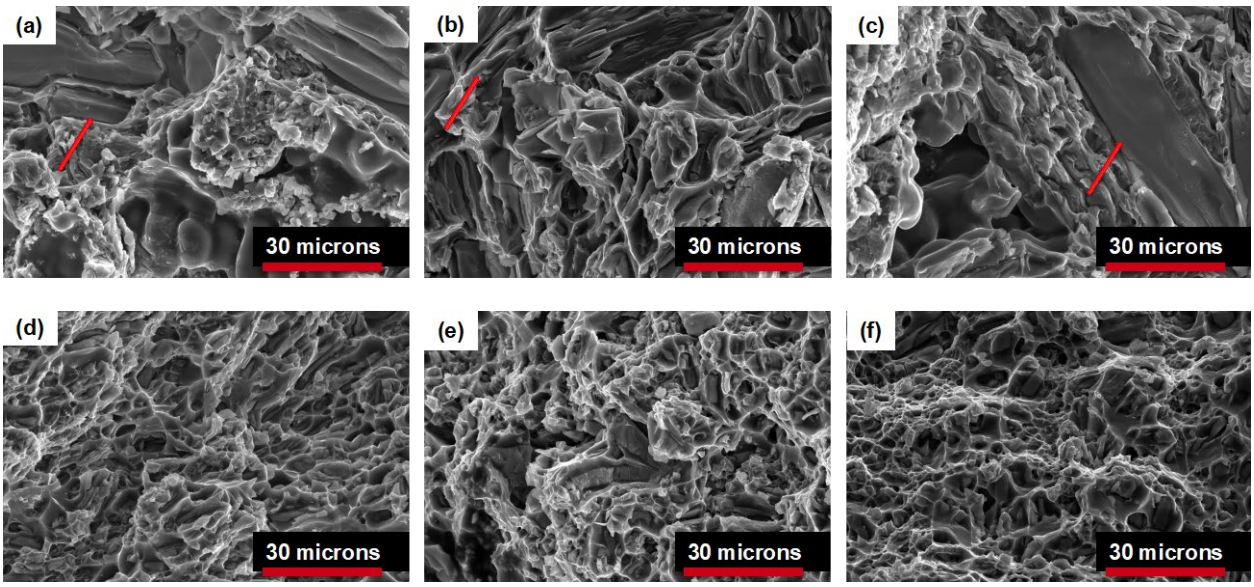

Figure S3.4 Fracture surfaces of as cast (a-c) and extruded (d-f) alloys before heat treatment (a and d), after 10 h annealing at 300°C (b and e) and after 100 h annealing at 300°C (c and f). Cleavage facets are shown by arrows in (a) to (c).

CHAPTER 4: MECHANICAL PROPERTIES AND MICROSTRUCTURE OF AL-CE-MG ALLOY PROCESSED BY ROLLINGs

Gaurav Singh[1,#], Humphrey Wara Odhiambo[2,#], Mohamad Hasan Bin Tasneem[1], Monica A. Soare[4], Jun Cui[2,3], Ralph E. Napolitano[2], Catalin R. Picu[1,*], Gaoyuan Ouyang[2,*]

[1]Department of Mechanical, Aerospace, and Nuclear Engineering, Rensselaer Polytechnic Institute, Troy, NY 12180

[2]Department of Materials Science & Engineering, Iowa State University, Ames, IA 50011

[3]Division of Materials Sciences and Engineering, Ames National Laboratory, Ames, IA 50011

[4]GE Aerospace Research, Niskayuna, NY 12309

#. Equal first author: Gaurav Singh and Humphrey Wara Odhiambo

*. Corresponding Authors: Catalin R. Picu (picuc@rpi.edu) & Gaoyuan Ouyang (gaoyuan@iastate.edu)

4.1 ABSTRACT

Aluminum alloys based on the Al-Ce-Mg system, with microstructure and properties weakly sensitive to elevated temperatures, are developed for applications such as thermal engine blocks and supersonic aircraft fuselage components. Cast Al-10Ce-4Mg (wt%) was produced by slab casting and further processed by rolling. Rolling with area reduction of 54% results in a 97% increase of the strength (tensile strength of 260 MPa at room temperature) relative to the as-cast state. We show that the Al-10Ce-4Mg is highly stable upon exposure to elevated temperature (81% strength retention after exposure to 300°C for 100h), far superior to high-temperature grade Al alloy AA2618. The ratio of the strength at 300°C to the strength at room temperature is 0.45, below the corresponding ratio of the Al-10Ce binary alloy (ratio 0.65) but above that of AA2618 (ratio 0.1).

Keywords: Al-Ce-Mg; Rolling; Microstructure characterization; Mechanical properties.

4.2 Statement of Contribution

The materials presented in this chapter are prepared and ready for submission. My specific contributions to the published work include:

1. Design and development of Al-Ce alloys.
2. Processing design and compositional optimization of Al-Ce-Mg alloys.
3. Microstructural and mechanical characterization, including scanning electron microscopy (SEM), X-ray diffraction (XRD), and Vickers microhardness testing.
4. Manuscript preparation, including drafting, writing, and editing.

4.3 Introduction

Aluminum-cerium alloys have been explored for use in components such as cylinder heads, turbocharger housings, and hydroelectric turbine blades, which demand high strength at elevated temperatures combined with the low density and corrosion resistance characteristic of Al alloys. These alloys are particularly notable for their thermal stability, retaining a large fraction of their room-temperature mechanical properties up to approximately 400 °C [1-4]. This remarkable property retention is primarily attributed to the thermodynamic and microstructural stability of the $Al_{11}Ce_3$ intermetallic phase [5-8]. The low solubility and diffusivity of Ce in the fcc Al matrix impart strong resistance to both intermetallic dissolution and particle coarsening at elevated temperatures [9]. In addition, the abundance and low cost of cerium compared to other rare-earth elements further enhance the attractiveness of Al-Ce alloys for high-temperature lightweight applications [10].

The strengthening effect of Ce addition arises mainly from a composite or phase-distribution strengthening mechanism, associated with a uniform dispersion of the hard $Al_{11}Ce_3$ intermetallic phase within the Al matrix. Consequently, Al-Ce alloys in the as-cast condition often exhibit moderate room-temperature strength [4,11,12]. Strength can, however, be enhanced by solution strengthening through alloying additions, which remain effective at elevated temperatures. For example, Mg additions have been shown to significantly increase the room-temperature strength of Al-Ce alloys [13,14].

Since the mechanical response of Al-Ce alloys depends critically on the volume fraction and morphology of the $Al_{11}Ce_3$ phase, the eutectic composition (approximately Al-10Ce) typically yields the best performance due to its fine lamellar or rod-like intermetallic

dispersion. Beyond compositional optimization, post-solidification processing can further refine the intermetallic morphology at a fixed volume fraction. Thermomechanical treatments, such as extrusion, effectively fragment lamellar or rod-like eutectic structures and refine the dispersion [12,15–17]. Despite its industrial relevance, rolling, a simpler and more widely applicable forming process, has received comparatively less attention in the context of Al-Ce alloys [18,19].

For example, Wang et al. [19] examined cold rolling of a hypoeutectic Al-5Ce alloy, which exhibited a cast microstructure of primary fcc-Al and an irregular eutectic (Al + $Al_{11}Ce_3$). After rolling, the dendritic features were no longer visible and the intermetallic particles aligned along the rolling direction. Zhang et al. [18] reported that cold rolling of an Al–9Ce alloy produced a heterogeneous lamellar microstructure consisting of alternating layers of coarse and fine grains, along with oriented $Al_{11}Ce_3$ particles, leading to an increase in ultimate tensile strength from 124 MPa (as-cast) to 200 MPa (rolled).

In the present work, we investigate the influence of deformation-induced structural refinement via rolling, in combination with solution strengthening from Mg addition, on the microstructure and high-temperature mechanical properties of the Al-10Ce-4Mg alloy. This study represents, to our knowledge, the first systematic examination of a rolled Al-Ce-Mg alloy. Microstructural evolution is characterized using SEM, XRD, and EBSD, while mechanical properties are evaluated through uniaxial tensile testing at both ambient and elevated temperatures. The effects of rolling-induced refinement on mechanical response and thermal stability are assessed in as-cast and hot-rolled conditions, before and after exposure to 300 °C for 100 h. We show that rolling produces dispersoid and grain refinement, and the resulting microstructure remains stable upon prolonged thermal exposure, exhibiting minimal degradation of mechanical properties.

4.4 Experimental Procedure

Al-10Ce-4Mg alloys were prepared by combining Al-20Ce and Al-50Mg master alloys with pure (0.9999 by weight) Al at 850°C in a graphite crucible, followed by mixing and casting into a graphite mold with internal dimensions of 5.5 × 2.8 × 0.8 in^3 (140 × 71 × 20 mm^3) and external dimensions of 6.89 × 4.33 × 1.26 in^3 (175 × 110 × 32 mm^3) preheated to 400°C. The cast Al-10Ce-4Mg ingot was rolled at different temperatures (225℃, 325℃, and 400℃). These temperatures were selected to span the τ phase ($Al_{13}CeMg_6$) solvus, as

shown by the phase diagram in Fig. 1a. Samples were heated to the target rolling temperature and held for 30 minutes before they were removed from the furnace and immediately fed to the rolling mill. The rolls were not heated. The nominal thickness reduction was about 10% for each pass, and samples were reheated to the respective rolling temperatures prior to each subsequent pass. A total of 5 passes were made on the rolls. The nominal rolling thickness reduction was 54% in all cases (above which excessive cracking may occur), which corresponds to a plastic strain of 61%. The rolled states are denoted by R-225C, R-325C and R-400C, while AC denotes the as cast state.

Tensile specimens with 52 mm gauge length were machined per the ASTM E8 standard [21] for all cast, rolled, and heat-treated conditions. Heat treatment of 10 h and 100 h at 300℃ was applied to selected samples, which were subsequently tested at room temperature to evaluate property retention. Tensile tests were performed using an Instron machine (Instron 5969, 50kN load cell) under quasi-static conditions ($\dot{\varepsilon} = 3 \times 10^{-3}\ s^{-1}$) at room temperature (25℃). Tests at elevated temperatures of 150℃, 200℃, 250℃, 300℃ and 350℃ were performed with the same system, samples being heated at a rate of $5℃/s$ to reach the test temperature, followed by a 300 s hold before the beginning of the test. Hardness was measured with a microhardness tester (Qness 60M QATM) with a load of 500 g, with 15 s dwell time, in accordance with ASTM E92 [22]. 10 measurements were made of each sample condition. The average values are reported here.

A FEI SEM was used for the metallography and fractography studies. Polished planar surfaces were prepared for examination by etching with Kellar's reagent for 10 s. EBSD was performed using an Oxford SEM microscope. Specimens were prepared with extra polishing steps (diamond and colloidal silica) to minimize surface deformation. EBSD image analysis was carried out using MTEX software. Phase mapping is based on FCC Al and orthorhombic $Al_{11}Ce_3$.

4.5 Results and Discussion

Figure 4.1b presents the normalized XRD patterns of the as-cast (AC) and rolled samples, confirming the presence of fcc-Al and $Al_{11}Ce_3$ phases in all conditions. No additional phases were detected within the resolution limits of the measurements. A slight variation in the Al peak intensities is observed between the AC and rolled samples, reflecting texture evolution that becomes more pronounced with increasing rolling temperature. The

absence of new diffraction peaks indicates that rolling does not alter the phase composition of the alloy.

The corresponding microstructures for the as-cast and rolled conditions are shown in Fig. 4.1d-g. Fine eutectic intermetallics formed during solidification are retained along with larger primary $Al_{11}Ce_3$ particles. Rolling induces partial fragmentation of these intermetallics and results in a measurable increase in hardness relative to the AC condition (Fig. 4.1c), although the hardness differences among the three rolled states remain minimal. No evidence of the ternary τ phase or any other Mg-containing intermetallic was observed by SEM or XRD in either the as-cast or rolled Al-10Ce-4Mg samples.

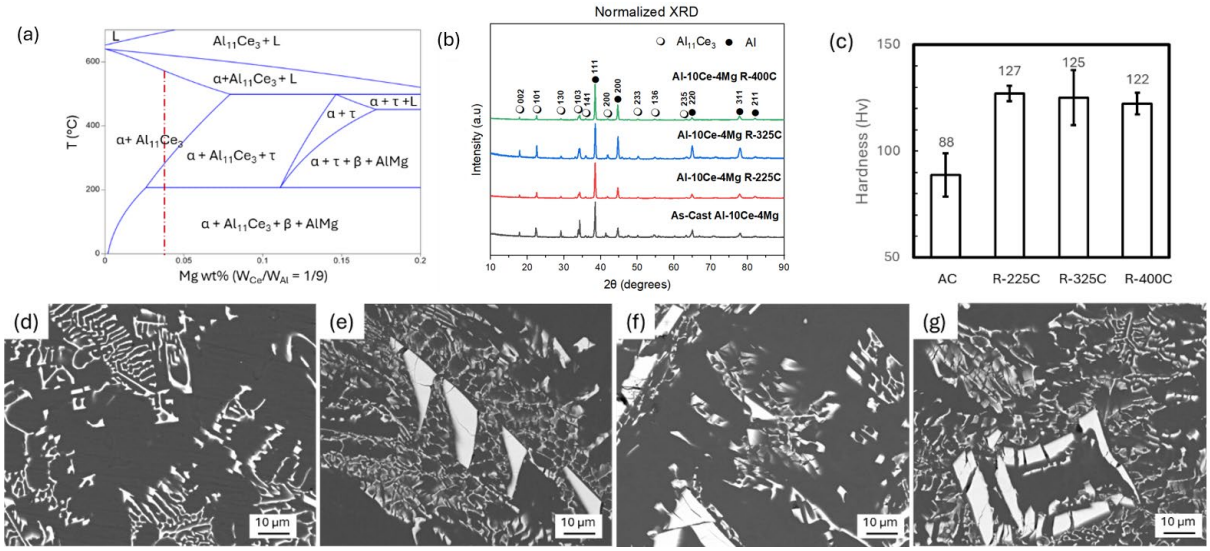

Figure 4.1. (a) Calculated pseudo binary Al-Ce-Mg phase diagram with the 4%Mg indicated by the red line; (b) XRD patterns for AC and rolled states; (c) Room temperature Vickers hardness of AC and rolled samples; Microstructure of Al-10Ce-4Mg alloy: (d) As-cast (e) R-225C (f) R-325C, and (g) R-400C.

Rolling produced significant microstructural refinement across all deformation conditions. In the R-225C specimen, the primary solidification phase was partially fragmented, while the eutectic $Al_{11}Ce_3$ network experienced pronounced plastic deformation. Localized surface cracking was observed under the applied deformation conditions. At 325 °C (R-325C), the microstructure exhibited limited coarsening of both the α-Al primary phase and the $Al_{11}Ce_3$ eutectic constituent, with particle growth accompanied by mild spanwise cracking that was less severe than in the R-225C sample. When rolled at 400 °C (R-400C), the alloy demonstrated higher flow stress and a relatively homogenized microstructure

compared to the other two samples (R-225C and R-325C). The primary solidification phase exhibited controlled coarsening comparable to that of R-225C and R-325C, and no surface defects were detected after deformation.

Based on these observations, the R-400C condition of the Al-10Ce-4Mgalloy was selected for detailed mechanical evaluation. Samples were tested in the as-rolled (AR) condition and after thermal exposure at 300 °C for 10 h (AR-10) and 100 h (AR-100) to assess strength retention and microstructural stability. The engineering stress-strain curves for all six conditions are presented in Figure 4.2a. The rolled samples (AR) exhibited substantially improved mechanical performance compared with the as-cast (AC) alloy. The AR condition showed an ultimate tensile strength (UTS) approximately 1.97 times higher than the AC condition, with elongation to failure increasing from 3.8 % to 7.9 %. After thermal exposure at 300 °C for 100 h, the AR-100 sample maintained an ultimate tensile strength approximately 1.94 times higher than that of the AC-100 alloy, while exhibiting a comparable elongation to failure of about 5.1 % (Table 4.1).

This improvement is attributed to deformation-induced refinement of both grains and $Al_{11}Ce_3$ dispersoids, which enhances load transfer and impedes dislocation motion, consistent with prior reports on rolled Al-Ce systems [18, 19]. The high-temperature stability of the $Al_{11}Ce_3$ phase restricts coarsening during thermal exposure, preserving the refined microstructure and enabling excellent property retention after extended heat treatment.

Heat treatment was performed to evaluate the retention of mechanical properties after thermal exposure at 300 °C. The engineering stress–strain curves for the AR-10 and AR-100 conditions (Fig. 4.2a) show a reduction in tensile strength of approximately 26% and 19%, respectively, compared with the as-rolled (AR) state. This strength reduction is attributed to the development of a more randomized crystallographic texture in the heat-treated samples, as observed in Fig. 4.3e-f. The yield and tensile strength retention ratios – defined as the ratio of the property in the heat-treated condition to that in the AR state – were determined to be 77% and 73% for AR-10, and 92% and 81% for AR-100, respectively. The concurrent decrease in elongation, to 77% and 66% of the AR values for AR-10 and AR-100, respectively, indicates that particle coarsening and texture evolution likely contribute to the observed variation in ductility.

The XRD patterns of the heat-treated and non-heat-treated samples are presented in Fig. 4.2b. No phase transformation was detected after thermal exposure at different durations, indicating that the $Al_{11}Ce_3$ intermetallic phase remains stable under the applied conditions. A significant decrease in the Al (200) peak intensity is observed from the AR state to the AR-10 condition, followed by a subsequent increase in the AR-100 sample. This evolution reflects variations in crystallographic texture, consistent with the EBSD observations shown in Fig. 4.3d-f. The texture modification during heat treatment may partially account for the non-monotonic trend in the stress-strain response of the rolled samples with increasing annealing time, as illustrated in Fig. 4.2a.

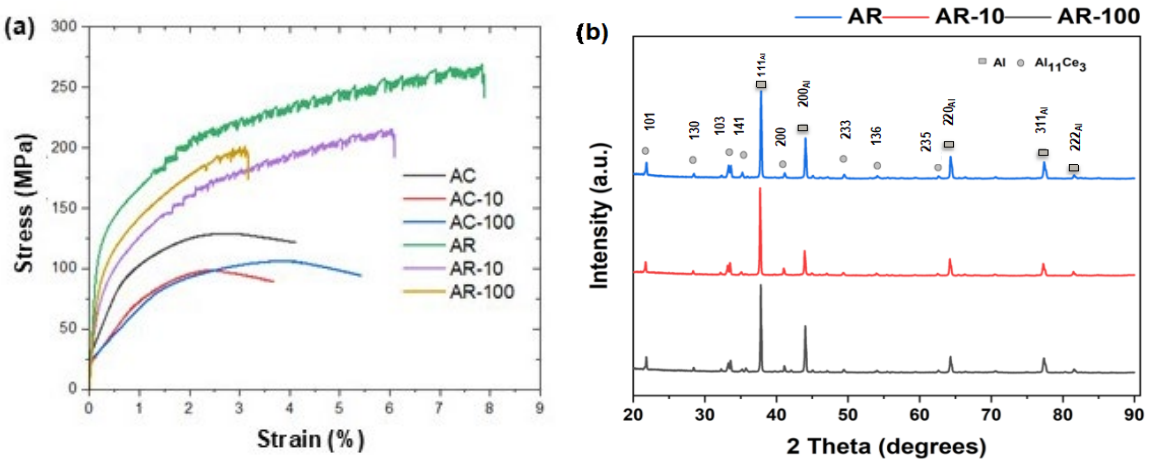

Figure 4.2. (a) Engineering stress-strain curves for as cast and rolled samples before and after heat treatment, (b) XRD spectra of rolled samples before and after heat treatment. 3 samples are tested, and these are representative curves.

Table 4.1. Comparison of room temperature mechanical properties of as cast and rolled alloy Al-10Ce-4Mg. The percentage represents strength/elongation retention after exposure to 300ºC.

	AC	**AC-10**	**AC-100**	**AR**	**AR-10**	**AR-100**
YS (MPa)	94	65	76	135	104 (77%)	124 (92%)
UTS (MPa)	132	102	108	260	190 (73%)	210 (81%)
%El	3.8	3.3	5.1	7.9	6.1 (77%)	5.2 (66%)

Figure 4.3a–c presents the EBSD inverse pole figure maps for the AR, AR-10, and AR-100 samples. No significant variation in grain size is observed across the three conditions, with average values of 19.8µm, 19.3µm, and 19.2µm for AR, AR-10, and AR-100, respectively. The as-cast (AC) sample exhibits a coarser average grain size of 24µm. A similar lack of substantial grain refinement has been reported for rolled AA5754 [23] and AA5182 [24] alloys with area reductions of 56% and 50%, respectively. The near invariance in grain size in the present study highlights the excellent thermal stability of the Al-10Ce-4Mgalloy, which can be attributed to the dispersion of thermally stable $Al_{11}Ce_3$ intermetallic particles and their Zener pinning effect on grain boundary motion.

With grain growth effectively suppressed, the modest decrease in strength during heat treatment is primarily attributed to the evolution of crystallographic texture. The texture intensity first decreases and subsequently increases with increasing annealing time, as shown in Fig. 4.3d-f. This trend parallels the variation in flow stress and ultimate tensile strength (UTS) observed for the AR, AR-10, and AR-100 samples (Fig. 4.2a), suggesting a strong correlation between texture evolution and mechanical response.

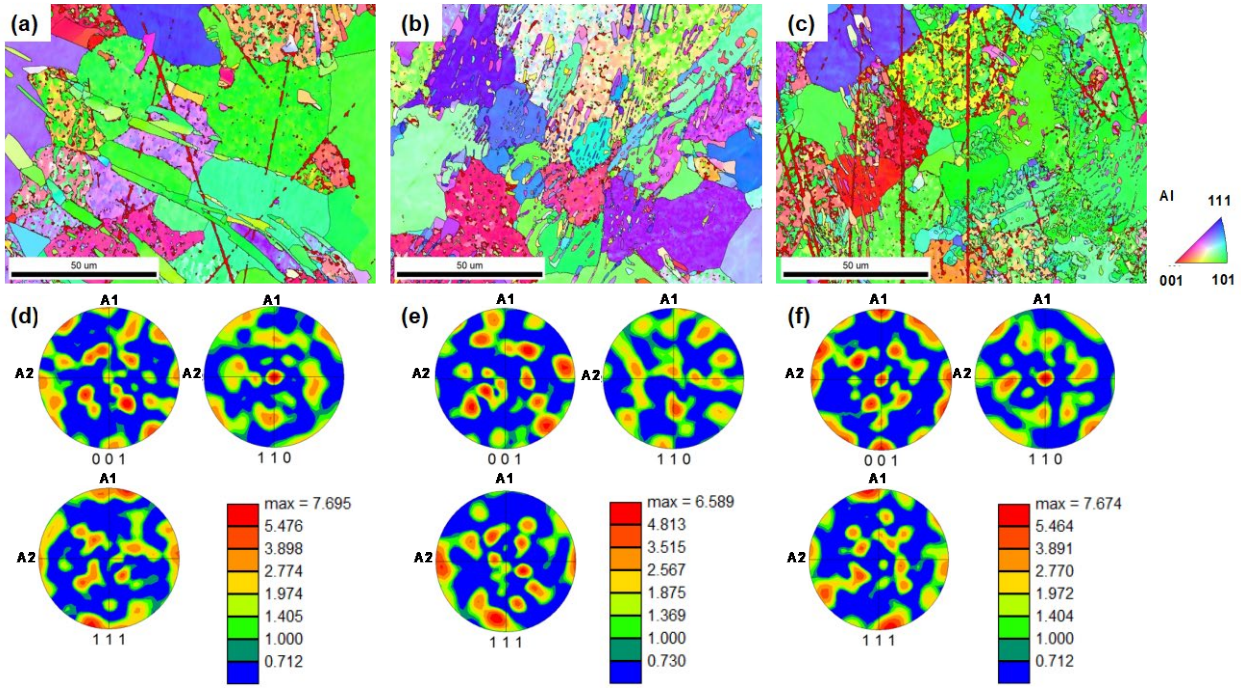

Figure 4.3. Inverse pole figure (IPF) map of (a) AR, (b) AR-10, (c) AR-100, and pole figures of (d) AR, (e) AR-10, and (f) AR-100 Al-10Ce-4Mg samples. (A1 is rolling direction, A2 is transverse direction)

Rolled samples (R-400C) were further tested at various temperatures of 150 °C, 200 °C, 250 °C, 300 °C, and 350 °C. Both the ultimate tensile strength (UTS) and yield strength decreased progressively with increasing temperature. Figure 4.4a presents the variation of UTS with temperature for the as-rolled (AR) Al-10Ce-4Mg alloy, compared with Al-10Ce [4] and the commercial Al-Mg alloy AA5182-O [25,26]. The Al-10Ce data corresponds to the as-cast (AC) condition, as rolled data are unavailable. The AA5182 alloy is included as a reference due to its similar magnesium content (~4 wt.% Mg).

The Al-10Ce alloy exhibits excellent thermal stability, showing only a modest reduction in UTS with increasing temperature up to 300 °C. In contrast, AA5182 displays a sharp decline in strength between 150 °C and 300 °C, attributed to the dissolution of fine Al-Mg precipitates [26]. The Al-10Ce-4Mg alloy demonstrates a combined response characteristic of both reference systems. Its room-temperature UTS is comparable to that of AA5182, yet the rate of strength degradation with temperature is markedly lower, owing to the thermal stability of the $Al_{11}Ce_3$ intermetallic dispersion. The alloy retains approximately 45% of its room-temperature UTS when tested at 300 °C, with a UTS value comparable to that of Al–10Ce at the same temperature.

For further context, the temperature-dependent behavior of the commercial high-temperature aluminum alloy AA2618 is also shown [27]. Although AA2618 exhibits a higher room-temperature UTS than the alloys examined here, its strength at 300 °C is inferior, underscoring the exceptional high-temperature stability of the Al-10Ce-4Mg system.

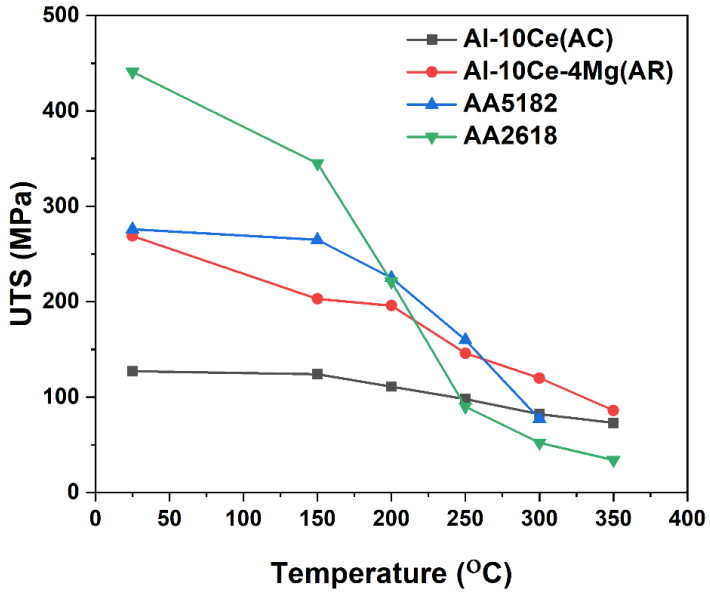

Figure 4.4. Variation with temperature of UTS for the AR state of Al-10Ce-4Mg compared with Al-10Ce and AA5182. The performance of the commercial high temperature alloy AA2618 is included for reference [4,24,26].

4.6 Conclusion

Hot rolling resulted in a clear enhancement of both strength and ductility in the Al-10Ce-4Mg alloy compared with the as-cast condition. The deformation process promoted fragmentation of the eutectic $Al_{11}Ce_3$ network and refinement of the aluminum matrix, leading to a more homogeneous microstructure. The addition of magnesium provided additional solid-solution strengthening, contributing to the superior room-temperature performance relative to the binary Al-Ce alloy.

Upon thermal exposure, the alloy exhibited exceptional microstructural stability. The $Al_{11}Ce_3$ intermetallic phase remained unchanged after prolonged annealing, effectively inhibiting grain growth through Zener pinning. Only minor variations in texture intensity were observed with increasing exposure time, corresponding to modest reductions in tensile strength and ductility. The rolled alloy retained approximately 45% of its room-temperature strength after testing at 300 °C, demonstrating superior high-temperature strength retention compared with conventional Al-Mg alloys such as AA5182 and even the high-temperature alloy AA2618.

The combined effects of dispersoid strengthening from $Al_{11}Ce_3$, solid-solution strengthening by Mg, and microstructural refinement induced by rolling result in a thermally stable alloy system with excellent strength retention up to 300–350 °C. These findings confirm the potential of the Al-10Ce-4Mg alloy as a lightweight, cost-effective candidate for elevated-temperature structural applications such as cylinder heads, turbocharger components, and turbine blades.

Acknowledgement

This work was supported by the US Department of Energy (DOE) through Grant No. DE-EE0010219.

4.7 References

[1] S. El-Hadad, M.E. Moussa, E. Riedel, M. Ahmed, R. Bähr, A. Nofal, Solidification Processing of Al-Ce Alloys for High-Temperature Applications, in: Ina. 2023, MDPI, Basel Switzerland, 2023: p. 17. https://doi.org/10.3390/engproc2023043017.

[2] A.E. Perrin, R.A. Michi, D.N. Leonard, K.D. Sisco, A.J. Plotkowski, A. Shyam, J.D. Poplawsky, L.F. Allard, Y. Yang, Effect of Mn on eutectic phase equilibria in Al-rich Al-Ce-Ni alloys, J. Alloys Compd. 965 (2023). https://doi.org/10.1016/j.jallcom.2023.171455.

[3] S. Nam, E. Simsek, N. Argibay, O. Rios, H.B. Henderson, D. Weiss, E.E. Moore, A.P. Perron, S.K. McCall, R.T. Ott, Strength mechanisms and tunability in Al-Ce-Mg ternary alloys enabled by additive manufacturing, Mater. Des. 231 (2023) 112009. https://doi.org/10.1016/j.matdes.2023.112009.

[4] G. Singh, H.W. Odhiambo, M.H. Bin Tasneem, G. Ouyang, M.A. Soare, J. Cui, R.E. Napolitano, C.R. Picu, Effect of thermomechanical processing on mechanical properties and the microstructure of binary Al-Ce alloy, Mater. Sci. Eng. A. 916 (2024) 147395. https://doi.org/10.1016/j.msea.2024.147395.

[5] Z. CAO, G. KONG, C. CHE, Y. WANG, H. PENG, Experimental investigation of eutectic point in Al-rich Al-La, Al-Ce, Al-Pr and Al-Nd systems, J. Rare Earths. 35 (2017) 1022–1028. https://doi.org/10.1016/S1002-0721(17)61008-1.

[6] Y. Sun, C. Hung, R.J. Hebert, C. Fennessy, S. Tulyani, M. Aindow, Eutectic microstructures in dilute Al-Ce and Al-Co alloys, Mater. Charact. 154 (2019) 269–276. https://doi.org/10.1016/j.matchar.2019.06.010.

[7] J. Ye, K. Dai, M. Gao, J. Chen, R. Guan, Primary phase transformation mechanism in a hypereutectic Al-Ce alloy during rapid solidification, Mater. Lett. 340 (2023). https://doi.org/10.1016/j.matlet.2023.134172.

[8] S. Shen, C. Wu, Y. Li, Y. Huang, W. Huang, P. Zhang, S. Zhong, Y. Lu, G. Luo, Z. Gan, J. Liu, Refining mechanism and elevated-temperature mechanical properties of Al-Ce alloys solidified under super gravity field, Mater. Sci. Eng. A. 879 (2023). https://doi.org/10.1016/j.msea.2023.145191.

[9] H. Okamoto, Al-Ce (Aluminum-Cerium), J. Phase Equilibria Diffus. 32 (2011) 392–393. https://doi.org/10.1007/S11669-011-9914-X/TABLES/1.

[10] K. Dai, J. Ye, Z. Wang, J. Chen, C. He, K. Xiong, Beneficial Utilization of Electromagnetic Stirring Technology in Al-Ce Alloys, JOM. 75 (2023) 2788–2798. https://doi.org/10.1007/s11837-023-05904-5.

[11] Y. Liu, R.A. Michi, D.C. Dunand, Cast near-eutectic Al-12.5 wt.% Ce alloy with high coarsening and creep resistance, (2019). https://doi.org/10.1016/j.msea.2019.138440.

[12] Z.C. Sims, O.R. Rios, D. Weiss, P.E.A. Turchi, A. Perron, J.R.I. Lee, T.T. Li, J.A. Hammons, M. Bagge-Hansen, T.M. Willey, K. An, Y. Chen, A.H. King, S.K. McCall, High performance aluminum-cerium alloys for high-temperature applications, Mater. Horizons. 4 (2017) 1070–1078. https://doi.org/10.1039/c7mh00391a.

[13] H. Lv, P. Peng, T. Feng, H. Gao, J. Ju, B. Wang, J. Wang, B. Sun, High-performance co-continuous Al-Ce-Mg alloy with in-situ nano-network structure fabricated by laser powder bed fusion, Addit. Manuf. 60 (2022) 103218. https://doi.org/10.1016/j.addma.2022.103218.

[14] G. Singh, H.W. Odhiambo, M.H. Bin Tasneem, G. Ouyang, M.A. Soare, Min-chul Kang, Lin Zhou, J. Cui, R.E. Napolitano, C.R. Picu, Effect of Thermomechanical Processing on Mechanical Properties and the Microstructure of Ternary Al-Ce-Mg Alloy, Acta Materialia, Submitted (2025).

[15] B. Hu, B. Quan, D. Li, X. Wang, Z. Li, X. Zeng, Solid solution strengthening mechanism in high pressure die casting Al–Ce–Mg alloys, Mater. Sci. Eng. A. 812 (2021). https://doi.org/10.1016/j.msea.2021.141109.

[16] D. Weiss, Improved High-Temperature Aluminum Alloys Containing Cerium, J. Mater. Eng. Perform. 28 (2019) 1903–1908. https://doi.org/10.1007/s11665-019-3884-2.

[17] Z.C. Sims, D. Weiss, S.K. McCall, M.A. McGuire, R.T. Ott, T. Geer, O. Rios, P.A.E. Turchi, Cerium-Based, Intermetallic-Strengthened Aluminum Casting Alloy: High-Volume Co-product Development, JOM. 68 (2016) 1940–1947. https://doi.org/10.1007/s11837-016-1943-9.

[18] C. Zhang, Y. Wang, H. Lv, H. Gao, J. Wang, B. Sun, Enhanced load transfer and ductility in Al–9Ce alloy through heterogeneous lamellar microstructure design by cold rolling and annealing, Mater. Sci. Eng. A. 821 (2021). https://doi.org/10.1016/j.msea.2021.141591.

[19] Y. Wang, X. Liang, L. Zeng, H. Wu, H. Li, The microstructure evolution of Al-5Ce alloy prepared by strain-induced melt activation during semi-solid isothermal treatment process, Mater. Lett. 326 (2022). https://doi.org/10.1016/j.matlet.2022.132948.

[20] J. Gröbner, D. Kevorkov, R. Schmid-Fetzer, Thermodynamic modeling of Al–Ce–Mg phase equilibria coupled with key experiments, Intermetallics. 10 (2002) 415–422. https://doi.org/10.1016/S0966-9795(02)00018-3.

[21] A. E8/E8M, Standard Test Methods for Tension Testing of Metallic Materials, ASTM Int. (2013). https://www.astm.org/standards/e8 (accessed May 21, 2022).

[22] A. E384-17, Standard Test Method for Microindentation Hardness of Materials, (2016). https://doi.org/10.1520/E0384-17.

[23] H. Jin, D.J. Lloyd, The reduction of planar anisotropy by texture modification through asymmetric rolling and annealing in AA5754, Mater. Sci. Eng. A. 399 (2005) 358–367. https://doi.org/10.1016/j.msea.2005.04.027.

[24] A. Bintu, G. Vincze, R.C. Picu, A.B. Lopes, Effect of symmetric and asymmetric rolling on the mechanical properties of AA5182, Mater. Des. 100 (2016) 151–156. https://doi.org/10.1016/j.matdes.2016.03.123.

[25] N. Abedrabbo, F. Pourboghrat, J. Carsley, Forming of AA5182-O and AA5754-O at elevated temperatures using coupled thermo-mechanical finite element models, Int. J. Plast. 23 (2007) 841–875. https://doi.org/10.1016/j.ijplas.2006.10.005.

[26] L. Ju, S. Patil, J. Dykeman, T. Altan, Forming of Al 5182-O in a Servo Press at Room and Elevated Temperatures, J. Manuf. Sci. Eng. 137 (2015). https://doi.org/10.1115/1.4030334.

[27] 2618 and 2618A: Al-Cu-Mg-Ni Alloys for High-Temperature Service, Prop. Sel. Alum. Alloy. (2019) 328–329. https://doi.org/10.31399/ASM.HB.V02B.A0006616.

CHAPTER 5: STRUCTURE AND PROPERTY RELATIONS OF A RAPIDLY SOLIDIFIED AL-CE-XY ALLOY

Humphrey Odhiambo [1], Ryan Ott [2], Jun Cui [1,2],Gaoyuan Ouyang [2]

1. Department of Materials Science and Engineering, Iowa State University, Ames, IA 50011, USA

2. Ames Laboratory/US Department of Energy, Ames, IA 50011, USA

5.1 ABSTRACT

Aluminum alloys are extensively utilized in the transportation sector due to their favorable strength-to-weight ratio and corrosion resistance. The incorporation of Ce into Al matrices promotes the formation of thermally stable intermetallic phases, such as $Al_{11}Ce_3$, which enhance high-temperature mechanical performance. However, the resultant properties are highly sensitive to the alloy's microstructural scale, primarily governed by the solidification kinetics. In this study, a ternary Al-7Ce-14Cu-0.5Zr (wt%) alloy was synthesized and subjected to rapid solidification via melt spinning. The process yielded a refined, nanoscale cellular microstructure with a continuous Al-Ce intermetallic network. Vickers hardness measurements revealed a significant enhancement, reaching 244 HV - approximately four times greater than that of conventionally cast binary Al-Ce alloys. Isothermal aging at 350 °C for 100 hours demonstrated excellent thermal stability, with the alloy retaining ~82% of its as-solidified hardness. These findings underscore the critical role of solidification rate in tailoring microstructure and mechanical performance in Al-Ce-based systems. The demonstrated thermal and microstructural stability of the Al-7Ce-14Cu-0.5Zr alloy renders it a promising candidate for structural components in elevated-temperature aerospace environments, such as supersonic airfoil applications. A detailed investigation into the influence of cooling rate and aging treatment on phase stability and mechanical behavior is presented.

Keywords: Al, Ce, thermal stability, rapid cooling, Microstructure.

5.2 Statement of Contribution

The materials presented in this chapter are prepared and ready for submission. My specific contributions to the published work include:

1. Processing design and development of Al-7Ce-14Cu-0.5Zr alloy.
2. Microstructural and mechanical characterization, including scanning electron microscopy (SEM), X-ray diffraction (XRD), and Vickers microhardness testing.
3. Manuscript preparation, including drafting, writing, and editing.

5.3 Introduction

Research into Al alloys designed for elevated temperature service has historically centered around precipitation-strengthened systems containing Sc, Zr, or V. These alloying elements form coherent, ordered Al_3X (X = Sc, Zr, V) precipitates within the face-centered cubic (fcc) Al matrix. These $L1_2$-structured particles impose coherency strains that hinder dislocation motion and act as barriers to diffusional creep, thereby improving strength retention at elevated temperatures [1,2]. However, these alloys suffer performance degradation above the so-called coherency loss temperature, at which the precipitates coarsen and transform into incoherent morphologies, significantly reducing their strengthening effect.

In contrast, Al-Ce alloys present a fundamentally different strengthening paradigm. These systems exhibit excellent thermal stability independent of processing history, primarily due to the formation of the incoherent, thermodynamically stable $Al_{11}Ce_3$ intermetallic phase during solidification [3,4]. Cerium's negligible solid solubility in Al and extremely low diffusivity impede Ostwald ripening and interfacial coarsening, thus preserving the eutectic morphology and associated mechanical properties even under extended thermal exposure [5].

Experimental investigations have confirmed that thermomechanical processing, such as extrusion, enhances the mechanical performance of Al-Ce alloys significantly. For instance, extruded binary Al-Ce alloys can achieve ultimate tensile strengths (UTS) near 400 MPa and yield strengths (YS) up to 320 MPa, attributable to fine-scale eutectic microstructures [6]. Even in the absence of deformation, as with hot isostatic pressing (HIP), these alloys maintain commendable strength levels (UTS ≈ 280 MPa, YS ≈ 220 MPa), emphasizing the inherent robustness of their solidification-derived microstructures [7].

The eutectic reaction in the Al-Ce system occurs at approximately 10.6 wt.% Ce and 621 °C, producing a finely lamellar network of α-Al and $Al_{11}Ce_3$ [3]. Since cerium does not significantly dissolve in Al, solid solution strengthening is negligible. However, minor additions of Mg, Si, or Cu can refine eutectic morphology and introduce additional hardening mechanisms via dispersed intermetallic formation. For example, alloying Al-12Ce with 4 wt.% Si and 0.4 wt.% Mg elevates the yield strength from approximately 57 MPa to 75 MPa, though at some expense to ductility [5-7].

Notably, the Al-7Ce-14Cu-0.5Zr alloy does not exhibit classical age-hardening behavior. Instead, the system shows limited solid solubility due to rapid quenching, consistent with the observations by Waterloo et al. (1996) and Zhang et al. (2022) [12, 13]. This further confirms that the observed hardness is largely microstructure-dependent, rather than arising from conventional precipitation hardening mechanisms. Microstructural characterization via Scanning Electoral Spectroscopy (SEM) reveals that Al_8CeCu_4 precipitates emerge during prolonged annealing. The gray phase, corresponding to this ternary intermetallic, becomes increasingly prominent over time. Crucially, no significant grain coarsening is observed even after 100 hours of annealing, implying a stable microstructural framework capable of preserving mechanical properties under thermal load.

According to Belov et al. (2006), the eutectic reaction $L \rightarrow (Al) + CeCu_4Al_8$ occurs at 610 °C for compositions near 14 wt.% Cu and 7 wt.% Ce-parameters that closely match the nominal composition of Al-7Ce-14Cu-0.5Zr [9]. At these concentrations, the solubility of Cu in α-Al is limited (<2%), thereby promoting the formation of thermodynamically stable intermetallics. Consequently, Cu contributes to both room-temperature and elevated-temperature strength via solid solution and precipitation strengthening, while Ce enhances grain refinement, castability, corrosion resistance, and thermal stability [12]. Zr further stabilizes the microstructure by inhibiting coarsening of intermetallic phases. The presence of $AlCu_2Zr$, complements the strengthening mechanisms by acting as a diffusion barrier and hindering grain boundary migration. The observed dominance of Ce-containing phases at grain boundaries restricts Cu diffusion and prevents the formation of Cu-depleted zones, improving resistance to intergranular corrosion [12]. Melt spinning promotes the redistribution and fragmentation of intermetallics, leading to a refined, homogeneous microstructure characterized by fine equiaxed grains and nanoscale precipitates. This morphology underpins the alloy's high initial hardness and thermal stability.

Beyond composition, the processing route dictates the microstructure morphology, precipitate size and distribution. While conventional casting offers industrial scalability, post-solidification treatments – such as extrusion, rolling, or induction melting – improve phase homogeneity and minimize porosity. Among these, rapid solidification (RS) techniques such as melt spinning have proven especially effective. These methods create high undercooling rates, reduce interlamellar spacing, suppress microsegregation, and enhance hardness [4]. sFrom an economic and sustainability standpoint, Ce offers a compelling alternative to Sc. As a low-cost, abundant rare earth metal, Ce enables large-scale alloy production with reduced dependence on strategic or critical elements.

Table 5.1. Al-Ce alloys Mechanical properties

		As-Cast				
No	**Alloy**	**UTS (MPa)**	**Yield Strength (MPa)**	**Elongation%**	**References**	**Comments**
1	Al-4Ce	72.1	29.9	15.4	[6]	
2	Al-6Ce	103	30	25	[30]	
3	Al-8Ce	148	-	19	[32]	
4	Al-10Ce	126	62.3	13.4	[6]	
5	Al-12Ce	163	58	13.5	[30]	
6	Al-16Ce	78.9	44.7	1.4	[6]	
7	Al-12Ce-1Cu-0.8Mg	172	74	6.2	[19]	
8	Al-12Ce-2Cu-0.8Mg	179	78	3.2	[19]	
9	Al-12Ce-3Cu-0.8Mg	148	83	1.4	[19]	
10	Al-12Ce-3Cu-1.5Mg	153	107	1.3	[19]	

Table 5.1 Continued

No	Alloy	As-Cast			References	Comments
		UTS (MPa)	Yield Strength (MPa)	Elongation %		
11	Al-12Ce-3Cu-2.4Mg	164	122	0.9	[19]	
12	Al-0.06Si-8.72Ce	68.7	0	1.3	[26]	
13	Al-9.7Fe-5.0Ce	490	380	10	[27]	
14	Al-8.4Fe-7.0Ce	570	470	9	[27]	
15	Al-9.6Fe-8.0Ce	610	500	5	[27]	
16	Al-7Cu-3Ce	459	274	4.4	[28]	
17	Al-14Cu-7Ce	438	367	1	[29]	Cold rolled
18	Al-14Cu-7Ce	360	320	1	[29]	Hot rolled at 450ºC
19	Al-8Ce-4Mg	189	107	3	[30]	
20	Al-8Ce-7Mg	195	151	2	[30]	
21	Al-8Ce-10Mg	227	186	1	[30]	
22	Al-10Ce-4Mg	132	94	3.8	[6]	
23	Al-12Ce-0.4Mg	200	78	6	[31]	
24	Al-12Ce-4Si-0.4Mg	141	75	2	[31]	

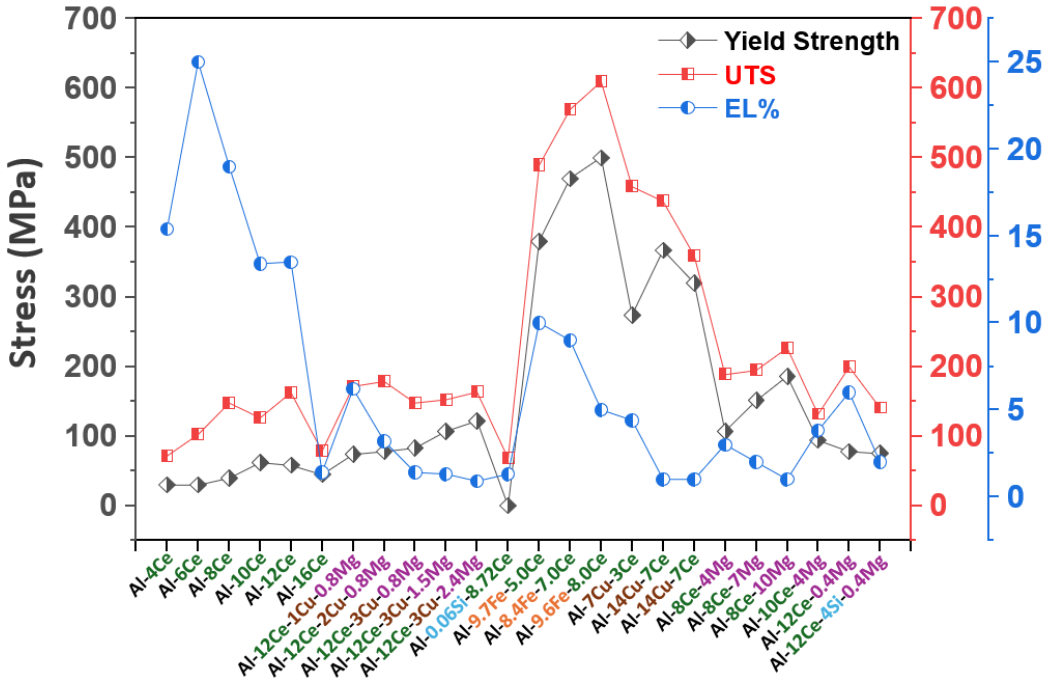

Figure 5.1. Summary of the mechanical properties of Al-Ce alloys, plotted from the results in Table 5.1

Although Al-Sc alloys can deliver higher peak strengths, their limited availability and high cost hinder widespread application [7]. The high-temperature stability and mechanical resilience of Al-Ce alloys derive from the inherent stability and dispersion of the $Al_{11}Ce_3$ phase. Unlike traditional precipitation-hardened alloys that are susceptible to overaging, Al-Ce systems maintain their properties through thermodynamic and kinetic suppression of coarsening. With optimized alloy design and processing strategies, particularly via rapid solidification and compositional tuning, Al-Ce alloys offer a viable path forward for next-generation structural components in aerospace, automotive, and energy sectors operating under thermal stress [1,4]. Table 5.1 and figure 5.1 above show the mechanical properties of Al-Ce alloys.

According to literature reports, Al-7Ce-14Cu exhibits the highest strength among the investigated Al-Ce-Cu alloys, a performance that is largely attributed to the synergistic effects of Cu additions on solid-solution strengthening and precipitation hardening. The incorporation of Zr is expected to provide an additional strengthening contribution through the formation of fine, thermally stable Al_3Zr precipitates, which can effectively hinder dislocation motion and suppress grain coarsening during thermal exposure. Furthermore,

increasing the cooling rate during solidification promotes significant grain refinement and the formation of a more uniform distribution of $Al_{11}Ce_3$ intermetallics, thereby enhancing both yield strength and thermal stability. Together, these effects suggest that careful control of alloying additions (e.g., Zr) and processing conditions (e.g., rapid solidification) could optimize the microstructural scale and stability of Al-7Ce-14Cu, ultimately enabling superior mechanical performance and strength retention at elevated temperatures. Such improvements are critical for extending the applicability of Al-Ce-Cu-Zr alloys in high-temperature structural applications, particularly in the automotive and energy sectors where lightweight, thermally stable materials are increasingly demanded.

5.4 Experiment Procedure

A master alloy with the nominal composition Al–7Ce–14Cu–0.5Zr (all compositions in wt.%) was synthesized by direct-chill casting. The alloy charge was melted at 850 °C and poured into a graphite mold (1 inch in diameter) preheated to 400 °C. Mold preheating was employed to minimize thermal gradients at the metal–mold interface, thereby promoting directional solidification and reducing macrosegregation [1]. A 4.60 g cylindrical section was cut from the cast ingot and subsequently processed by rapid solidification using the melt-spinning technique. The melt, held at 800 °C in a quartz crucible equipped with a 0.8 mm nozzle, was ejected onto a rotating copper wheel under a reduced helium pressure of approximately 0.33 atm. The process parameters included a nozzle-to-wheel distance of 1.0 mm, a wheel speed of 30 m/s, and a 90° injection angle, producing cooling rates on the order of 10^5–10^6 K/s. These conditions yielded continuous ultrafine ribbons with an average thickness of approximately ~32 μm, consistent with previously reported results for high-energy melt spinning of Al-Ce-based alloys [14].

The ribbons were mounted in epoxy and prepared using standard grinding and polishing techniques for hardness and microstructure characterization. Microhardness measurements were carried out using a Vickers indenter under a 10 g load and 13 s dwell time, capturing the as-solidified microstructure's mechanical response. A minimum of ten indentations per condition (as-spun and annealed) were taken to ensure data reproducibility. To investigate thermal stability and microstructural evolution, isothermal annealing was conducted at 350 °C for durations of 0.5, 1, 5, 10, 50, and 100 hours. This temperature was selected to simulate service environments and evaluate precipitate coarsening behavior. Post-annealing characterization involved optical microscopy and scanning electron microscopy

(SEM) to analyze grain morphology and the evolution of $Al_{11}Ce_3$, Al_2Cu, and Al_3Zr intermetallic phases [12, 16].

Additionally, X-ray diffraction (XRD) was employed to identify phase constituents and track the development of secondary phases over prolonged exposure. The selection of Cu and Zr in the alloy design is informed by their synergistic strengthening roles: Cu enhances age-hardening via Al_2Cu precipitates, while Zr contributes to grain boundary pinning and recrystallization resistance via Al_3Zr dispersoids [5, 13]. Meanwhile, Ce promotes thermal stability by forming the thermodynamically stable, coarsening-resistant $Al_{11}Ce_3$ phase, which does not dissolve during thermal exposure and impedes dislocation motion [12]. This integrated processing approach – combining rapid solidification, multi-component alloying, and thermal stability analysis – targets the development of a high-strength, thermally stable Al alloy suitable for applications requiring sustained mechanical performance at elevated temperatures.

5.5 Results and Discussion

5.5.1 Processing

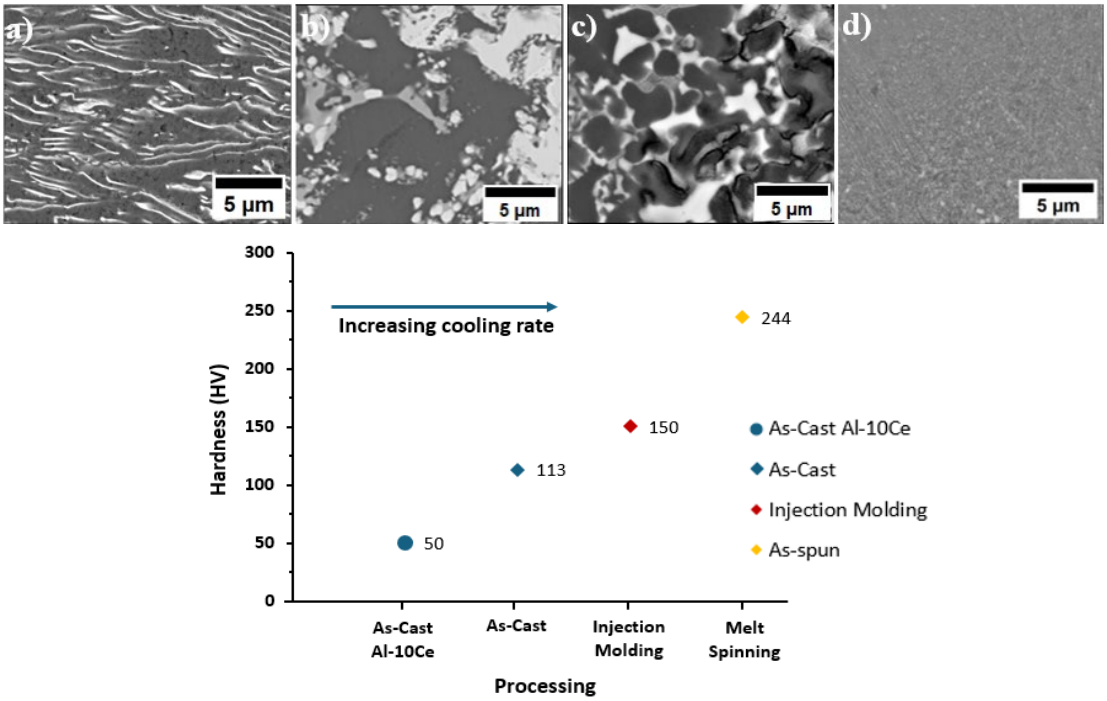

Figure 5.2. Microstructures of (a) as-cast Al-10Ce, (b) as-cast Al-7Ce-14Cu-0.5Zr, (c) Al-7Ce-14Cu-0.5Zr processed via injection molding, and (d) Al-7Ce-14Cu-0.5Zr melt-spun ribbon.

Figure 5.2 (a) shows a two-phase microstructure composed of a dark α-Al (FCC) matrix and a bright eutectic constituent. The eutectic consists of lamellar networks of α-Al and $Al_{11}Ce_3$, where the $Al_{11}Ce_3$ intermetallic forms a uniformly distributed, interconnected morphology. This finely dispersed second phase provides the primary strengthening contribution, and its thermal stability is essential for maintaining mechanical performance at elevated temperatures. In contrast, Figures 5.2(b–d) reveal a more complex four-phase microstructure, three of which are clearly visible. The dark regions correspond to the α-Al matrix, the gray regions to the Al_8CeCu_4 phase, and the bright regions to $Al_{11}Ce_3$. A fourth phase, Al_2CuZr, is present in the matrix but appears sporadically and may precipitate depending on the specific processing conditions.

In Al-10Ce alloys, solidification is governed by the near-eutectic composition of the Al-Ce binary system, where the eutectic reaction occurs at approximately 10.6 wt.% Ce and 621 °C [15]. As cooling proceeds, the melt undercools until the eutectic temperature is reached, at which point simultaneous cooperative growth of the primary α-Al matrix and the thermodynamically stable $Al_{11}Ce_3$ intermetallic phase occurs from the remaining liquid. This process produces a lamellar eutectic morphology, with alternating α-Al and $Al_{11}Ce_3$ phases arranged in a finely coupled network. The lamellar spacing is sensitive to the cooling rate, coarsening under slow solidification and refining significantly under rapid solidification conditions [15,7].

Unlike metastable precipitate-strengthened alloys, where coarsening and loss of coherency degrade properties, Al-Ce systems derive their stability from the negligible solid solubility of Ce in Al and the extremely low diffusivity of Ce atoms. These factors suppress Ostwald ripening and interfacial coarsening, preserving the integrity of the eutectic morphology during extended thermal exposure. Experimental evidence confirms that the as-cast eutectic in Al-10Ce alloys exhibits remarkable thermal stability, retaining its microstructural features and associated mechanical performance even under elevated temperatures relevant to aerospace and automotive applications [17].

Literature establishes that when the Cu:Ce ratio is approximately 2:1, Cu interacts with Al and Ce to form stable Al-Ce-Cu intermetallic phases, thereby enhancing alloy properties [19]. Belov et al. reported an invariant quasi-binary eutectic reaction in Al-Ce-Cu alloys, alloys [$L \rightarrow (Al) + Al_8CeCu_4$ (610^{o}C, 14 wt.% Cu and 7wt.% Ce)] which has guided alloy design strategies by highlighting the influence of composition and solidification path on

microstructural development [9]. Complementary work by Guoqiang et al. on eutectic Al-10Ce alloys demonstrated that increasing Zr content from 0.05 to 0.15 wt.% resulted in gradual coarsening of the $Al_{11}Ce_3$ phase, whereas further additions promoted refinement and homogenization of the microstructure. Importantly, the eutectic morphology transformed from lamellar to rod-like $Al_{11}Ce_3$ with higher Zr concentrations, underscoring the sensitivity of phase morphology to compositional tuning [20].

The refinement trends observed in Figure 2(a–d) illustrate the combined effects of alloying and processing on microstructure evolution. Guarav and Odhiambo et al. reported an average grain size of 582 ± 143 μm for as-cast Al-10Ce [21]. Further, the addition of 0.2 wt.% Zr to Al–5Ce reduced grain size from 1320 μm to 495 μm [23], a refinement attributed to the formation of Al_3Zr precipitates that serve as effective heterogeneous nucleation sites while suppressing coarse columnar grains [22]. Ce contributes additional refinement through the formation of intermetallic phases such as $Al_{11}Ce_3$ and Al_8CeCu_4, both of which act as potent nucleation substrates for the Al matrix. The concurrent addition of Zr to Al-Ce-Cu alloys, such as Al-7Ce-14Cu, is therefore expected to synergistically refine grain structure even in the as-cast condition. The progressive reduction in grain size observed in Figure 1(a–d) reflects this combined influence of composition optimization and processing route.

The microstructural refinement observed in Figure 2(a–d) is directly reflected in the hardness response of the alloys. The as-cast Al-10Ce binary eutectic exhibits a relatively low hardness of ~50 HV, consistent with its coarse lamellar α-Al + $Al_{11}Ce_3$ morphology. By comparison, the as-cast Al-7Ce-14Cu-0.5Zr alloy demonstrates a significantly higher hardness of ~113 HV. This increase can be attributed to the compositional effect of Cu and Zr additions, which modify the morphology of the $Al_{11}Ce_3$ eutectic phase and promote the formation of additional intermetallics such as Al_8CeCu_4 and Al_2CuZr. These phases contribute to microstructural refinement and act as stable strengthening constituents.

Literature further supports the significance of composition, with Odhiambo et al. reporting that near-eutectic Al–10Ce exhibits higher strength than hypereutectic Al-16Ce, while alloys with lower Ce content display reduced hardness, emphasizing the importance of compositional balance [24].Microstructural analysis demonstrates that fabrication route strongly dictates the morphology and spatial distribution of phases. In the as-cast condition, three distinct constituents are observed: primary α-Al (dark), Al_8CeCu_4 (gray), and the thermally stable $Al_{11}Ce_3$ intermetallic (white). No evidence of primary $Al_{11}Ce_3$ crystallization

or a fully interconnected eutectic network is detected, consistent with the hypoeutectic nature of the Al-7Ce composition. The heterogeneous distribution of precipitates in this state correlates with the relatively low hardness of ~113 HV.

Injection molding produces a similar phase constitution but with notable refinement and more homogeneous dispersion. The $Al_{11}Ce_3$ phase manifests as discrete particles rather than interconnected laths, while the Al_8CeCu_4 phase remains stable. These morphological modifications yield a ~30% increase in hardness relative to the as-cast condition, underscoring the influence of moderately increased cooling rates on precipitate refinement and phase stability. The most significant transformation occurs in the melt-spun ribbons, where rapid solidification drives nanoscale phase dispersion. The $Al_{11}Ce_3$ phase develops a fine cellular lath-like morphology, and both Al_8CeCu_4 and $AlCu_2Zr$ appear as sub-micrometer precipitates uniformly embedded within the α-Al matrix. This nanoscale dispersion enhances strengthening through grain refinement, solute trapping, and dislocation pinning. EDS analysis confirms the presence of four phases: α-Al, $AlCu_2Zr$, Al_8CeCu_4, and $Al_{11}Ce_3$. The transition from the coarse, inhomogeneous as-cast structure to the refined, homogeneously distributed microstructure in the melt-spun ribbon explains the substantial hardness increase from 113.2 HV to 244 HV – a ~116% improvement.

Processing effects are equally critical in determining mechanical response. The injection-molded Al-7Ce-14Cu-0.5Zr alloy attains a hardness of ~150 HV, exceeding its as-cast counterpart due to higher cooling rates that promote finer and more homogeneously distributed microstructural features. The most pronounced refinement is observed in the melt-spun ribbon, which exhibits a hardness of ~244 HV. This nearly 200% increase relative to the as-cast state is a direct consequence of rapid solidification, producing ultrafine, uniformly distributed eutectic phases with grain sizes below 2 μm. Such refinement highlights the efficacy of rapid solidification in enhancing property retention by suppressing microstructural coarsening. These observations also conform to the classical Hall–Petch relationship, wherein yield strength (and hardness as a proxy) increases with decreasing grain size due to the restriction of dislocation motion by grain boundaries [24]. Collectively, these results demonstrate that a synergistic strategy of compositional tuning and processing control – particularly by optimizing cooling rates and precipitate morphology – provides an effective pathway to engineer microstructures with superior mechanical performance in Al-Ce-based alloys.

5.5.2 Microstructure evolution with Heat treatment

Current research on Al-Ce alloys increasingly emphasizes compositional design and processing control to optimize mechanical performance and thermal stability. Among these systems, the quaternary Al-7Ce-14Cu-0.5Zr alloy (all compositions in wt.%) has shown promise when processed via rapid solidification methods such as melt spinning. This alloy exemplifies the effectiveness of composition-processing synergy in achieving both microstructural refinement and enhanced hardness for high-temperature structural applications.

To evaluate thermal stability, melt-spun Al-7Ce-14Cu-0.5Zr ribbons were annealed isothermally at 350 °C for durations between 0.5 and 100 h. Figure 5.3 presents the microstructural evolution under these conditions. The as-spun state displays a finely dispersed $Al_{11}Ce_3$ network, uniformly distributed within the α-Al matrix, with a characteristic grain size below 0.5 μm. Whereas conventional Al–Ce alloys typically show microstructural degradation above 250 °C, this alloy maintains stability at ~350 °C. After 1h of annealing, nanoscale Al_8CeCu_4 precipitates emerge, contributing to additional precipitation strengthening. Even after 100 h, coarsening remains limited and the eutectic architecture is largely preserved. These findings confirm the exceptional high-temperature stability of the alloy and highlight the effectiveness of rapid solidification coupled with multicomponent alloying in suppressing microstructural degradation under prolonged thermal exposure.

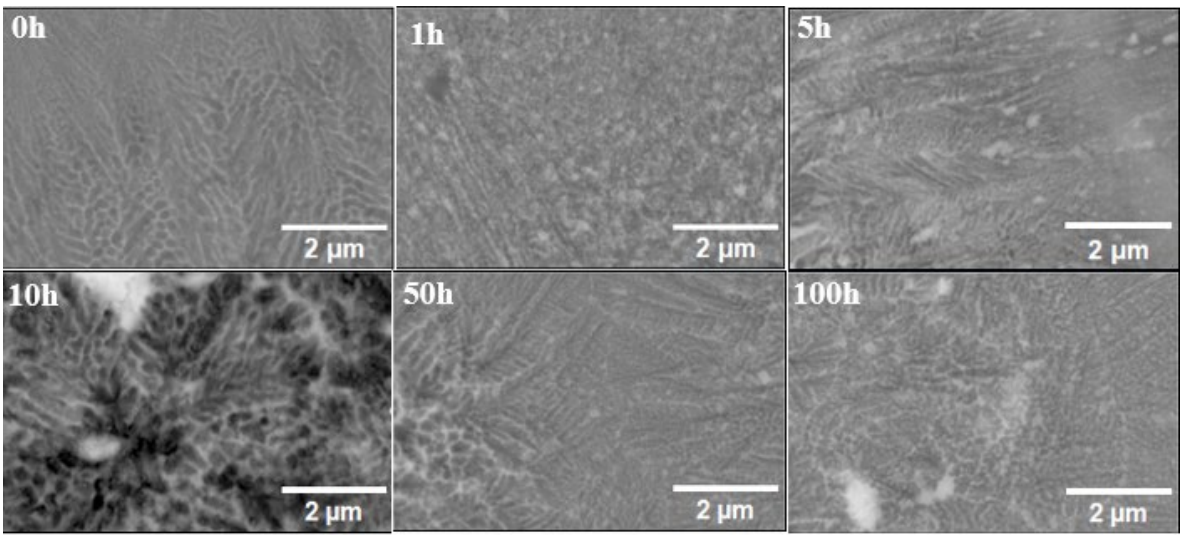

Figure 5.3. Microstructural evolution of melt-spun Al-7Ce-14Cu-0.5Zr alloy during isothermal annealing for 0–100 h, showing progressive coarsening of the eutectic network and morphological transformation of the $Al_{11}Ce_3$ phase.

The evolution of Vickers hardness with annealing time highlights the interplay between recovery, precipitation, and coarsening mechanisms. Figure 5.4 presents (a) Vickers microhardness values and (b) XRD patterns of melt-spun Al-7Ce-14Cu-0.5Zr subjected to isothermal annealing at 350 °C for up to 100 h. The as-spun ribbon exhibits an initial hardness of 244 HV, which decreases to 228 HV after 0.5 h due to recovery and partial dislocation annihilation. At 1 h, a modest increase to 233 HV suggests the onset of precipitation hardening, most likely associated with the nucleation of fine Al_8CeCu_4 precipitates. Peak hardness of 237 HV is attained at 5 h, corresponding to optimal dispersion strengthening from uniformly distributed nanoscale intermetallics. Prolonged annealing induces overaging and eutectic coarsening, leading to gradual hardness reduction—213 HV at 10 h, 181 HV at 50 h, and 189 HV at 100 h. Despite this decline, the alloy retains ~77% of its peak hardness after 100 h, underscoring the exceptional thermal stability of the melt-spun microstructure and confirming its ability to withstand extended exposure at 350 °C without catastrophic degradation.

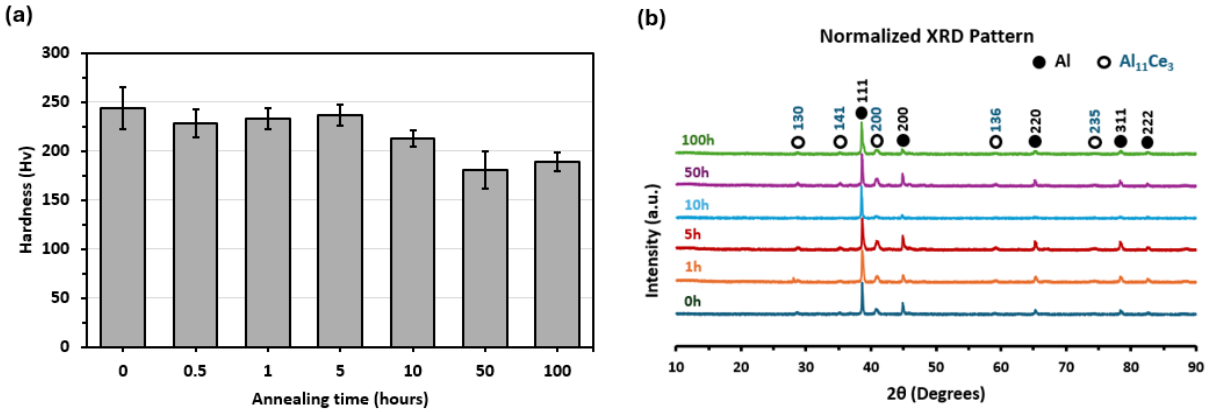

Figure 5.4. Melt-spun Al-7Ce-14Cu-0.5Zr alloy subjected to annealing for 0-100 h: (a) Vickers microhardness measurements illustrating hardness response as a function of annealing time, and (b) XRD patterns showing phase stability and evolution.

The exceptional hardness of the as-spun Al-7Ce-14Cu-0.5Zrribbon (244 HV) arises from a synergistic combination of solid solution strengthening, grain refinement, and the homogeneous dispersion of nanoscale precipitates. The rapid solidification achieved during

melt-spinning produces a cellular lath-like $Al_{11}Ce_3$ phase embedded within the α-Al matrix, while solute trapping and suppressed segregation enhance uniformity. To evaluate microstructural stability, isothermal annealing at 350 °C was conducted for 0.5–100 h. This treatment enables both precipitation of metastable and equilibrium phases and assessment of thermal robustness under prolonged exposure. After 1 h, nanoscale bright precipitates corresponding to intermetallic phases are observed, indicating early-stage precipitation; this coincides with a ~10% reduction in hardness relative to the as-spun state.

These results are consistent with Zhang et al. (2022), who reported that rapid solidification of Al-Ce alloys under high undercooling suppresses coarse primary intermetallics [14]. In the present alloy, no primary $Al_{11}Ce_3$ crystallization is detected in the as-spun state, further supporting this mechanism. Moreover, Zhang et al. demonstrated that rapidly solidified Al-8Ce and Al-20Ce alloys retained their hardness during annealing below 300 °C. The present findings extend this stability to 350 °C, confirming the thermal robustness of the Al-7Ce-14Cu-0.5Zrsystem.

5.5.3 X-ray Diffraction

The normalized XRD spectra of the as-spun ribbon subjected to aging treatments (0 - 100 h) at 350 °C are shown in Figure 4(b). In all conditions, the diffraction patterns reveal the presence of α-Al and $Al_{11}Ce_3$ intermetallic phases. The relative intensities of the $Al_{11}Ce_3$ peaks remain essentially unchanged throughout aging, indicating that the volume fraction and stability of this phase are unaffected by prolonged exposure. The dominant α-Al reflections correspond to the (111) and (200) planes across all annealing times, with the (111) peak consistently exhibiting the highest intensity. A gradual decline in the intensity of most α-Al reflections, except for (111), is observed after 10 h, suggesting crystallite size refinement and possible texture evolution at this aging condition. Importantly, no additional peaks or shifts are detected, confirming the absence of phase transformations in both the as-spun and aged samples. These findings underscore the thermal stability of the alloy with respect to phase constitution and align with Vickers microhardness results, which show negligible loss in hardness for as-spun Al-7Ce-14Cu-0.5Zreven after 100 h of aging.

5.5.4 Strengthening Mechanism of as-spun Al-7Ce-14Cu-0.5Zr

The strengthening in the as-spun Al-7Ce-14Cu-0.5Zr alloy can be described as the additive contribution of multiple mechanisms, expressed as:

$$\sigma_y = \sigma_{Disl} + \sigma_{Gb} + \sigma_{SS} + \sigma_{PP}$$

where σ_y is the macroscopic yield strength, σ_{Disl} is the contribution from dislocation strengthening, σ_{Gb} is Hall–Petch grain boundary strengthening, σ_{SS} is solid solution strengthening, and σ_{PP} is precipitation strengthening [25].

Dislocation strengthening follows the Taylor relation:

$\Delta\sigma_{Disl} = MG\alpha b\sqrt{\rho}$,

where M is the Taylor factor (2.94 for Al), α is a constant (0.24), G is the shear modulus (26 GPa), b is the Burgers vector (0.286 nm), and ρ is the dislocation density (~5×10^{13} m^{-2}). Substitution yields ~37 MPa.

Hall–Petch strengthening is given as:

$\sigma_{Gb} = \sigma_o + kd^{0.5}$

where σ_o is the intrinsic yield strength of pure Al (~20 MPa), k is the Hall–Petch coefficient (0.07 MPa·$m^{0.5}$) and d is the average grain size (< 0.5 μm for melt-spun ribbons).

Solid solution strengthening can be estimated using:

$$\Delta\sigma_{SS} = kc^{2/3}$$

where $k \approx 29$ MPa/at.%$^{2/3}$ and c is the solute concentration in atomic percent.

Precipitation strengthening is derived from the dispersed $Al_{11}Ce_3$, Al_8CeCu_4, and Al_2CuZr phases, approximated by:

$$\Delta\sigma_{pp} = 4\emptyset\gamma G_{Al} f_{Al11Ce3}\varepsilon^*$$

Where: $\gamma = \frac{1}{2(1-\nu)}$, ν is the Poisson ratio, $\varepsilon*$ is the effective plastic strain (~0.002), ϕ is a shear modulus mismatch factor defined as

$$\phi = \frac{G_{Al11Ce3}}{G_{Al11Ce3} - \gamma(G_{Al11Ce3} - G_{Al})}$$

and $f_{Al11Ce3}$ is the precipitate volume fraction.

Assuming a grain size of 0.5 μm and a dislocation density of approximately 5×10^{13} m^{-2} (as reported in Ref. [25]), with an $Al_{11}Ce_3$ volume fraction of 20%, the following strengthening contributions were obtained as shown in table 5.2 below:

Table 5.2 Strengthening Contributions in the as-spun Al-7Ce-14Cu-0.5Zr alloy

σ_{Gb}	σ_{Disl}	σ_{PP}
119MPa	37MPa	17.7MPa

From Table 5.2, it is evident that Hall–Petch grain boundary strengthening provides the most significant contribution to the overall yield strength. This enhancement arises from the refinement and uniform dispersion of the $Al_{11}Ce_3$ intermetallic phase, which promotes a more homogeneous microstructure. The refined $Al_{11}Ce_3$ particles effectively inhibit grain growth and improve resistance to dissolution and coarsening during thermal exposure, thereby stabilizing the microstructure and maintaining strength at elevated temperatures.

5.6 Conclusion

Melt spinning fundamentally transforms the Al-7Ce-14Cu-0.5Zr microstructure and, consequently, its properties. Relative to the as-cast state (~113 HV), rapid solidification produces an ultrafine, homogeneously dispersed α-Al/$Al_{11}Ce_3$ architecture with nanoscale Al_8CeCu_4 and $AlCu_2Zr$ precipitates, raising hardness to ~244 HV. Isothermal aging at 350 °C for up to 100 h results in only moderate softening (to ~189 HV, ~77% retention), indicating suppressed coarsening and exceptional thermal stability of the as-spun microstructure. The observed behavior is consistent with coupled Hall–Petch strengthening (sub-micrometer structural length scale, ≤0.5 μm) and Orowan strengthening from uniformly dispersed, non-shearable intermetallics, complemented by limited solid-solution and dislocation contributions. Collectively, these results demonstrate that coordinated control of composition (Ce-Cu-Zr) and processing (cooling rate) provides a robust pathway to engineer stable, high-strength Al-Ce-based alloys for elevated-temperature applications.

5.7 References

[1] Meyers MA, Chawla KK. Mechanical behavior of materials. Cambridge university press; 2008 Nov 6.

[2] Callister WD, Rethwisch DG. Materials Science and Engineering, eight edition.

[3] Czerwinski F. Thermal stability of Al alloys. Materials. 2020 Aug 4;13(15):3441.

[4] Plotkowski A, Rios O, Sridharan N, Sims Z, Unocic K, Ott RT, Dehoff RR, Babu SS. Evaluation of an Al-Ce alloy for laser additive manufacturing. Acta Materialia. 2017 Mar 1;126:507-19.

[5] Czerwinski F. Cerium in Al alloys. Journal of materials science. 2020 Jan;55(1):24-72.

[6] Singh G, Odhiambo HW, Tasneem MH, Ouyang G, Soare MA, Cui J, Napolitano RE, Picu CR. Effect of thermomechanical processing on mechanical properties and the microstructure of binary Al-Ce alloy. Materials Science and Engineering: A. 2024 Nov 1;916:147395.

[7] Sims ZC, Rios OR, Weiss D, Turchi PE, Perron A, Lee JR, Li TT, Hammons JA, Bagge-Hansen M, Willey TM, An K. High performance Al–cerium alloys for high-temperature applications. Materials Horizons. 2017;4(6):1070-8.

[8] Sisco K, Plotkowski A, Yang Y, Leonard D, Stump B, Nandwana P, Dehoff RR, Babu SS. Microstructure and properties of additively manufactured Al–Ce–Mg alloys. Scientific Reports. 2021 Mar 26;11(1):6953.

[9] Belov NA, Khvan AV, Alabin AN. Microstructure, and phase composition of Al-Ce-Cu alloys in the Al-rich corner. In Materials science forum 2006 Jul 1 (Vol. 519, pp. 395-400). Trans Tech Publications Ltd.

[10] Duwez, Pol, R. H. Willens, and W. Klement. "Continuous series of metastable solid solutions in silver-copper alloys." *Journal of Applied Physics* 31, no. 6 (1960): 1136.

[11] Waterloo, G., and H. Jones. "Microstructure and thermal stability of melt-spun Al-Nd and Al-Ce alloy ribbons." *Journal of materials science* 31 (1996): 2301-2310.

[12] Weiss D. Composites and Alloys Based on the Al-Ce System. Al Alloys and Composites. 2019 Nov 23.

[13] Zhang, Zhonghua, Xiufang Bian, and Yan Wang. "Effect of ejection temperature and wheel speed on the microstructure of melt-spun Al-20 Ce alloy." *Journal of alloys and compounds* 349, no. 1-2 (2003): 185-192.

[14] Zhang Z, Bian X, Wang Y. Microstructural characterization and microhardness of rapidly solidified Al–Ce alloys. International Journal of Materials Research. 2022 Jan 3;93(6):578-84.

[15] Kang YB, Pelton AD, Chartrand P, Fuerst CD. Critical evaluation and thermodynamic optimization of the Al–Ce, Al–Y, Al–Sc and Mg–Sc binary systems. Calphad. 2008 Jun 1;32(2):413-22.

[16] Russell A, Lee KL. Structure-property relations in nonferrous metals. John Wiley & Sons; 2005 Jun 24.

[17] Zhang Z, Bian X, Wang Y. Microstructural characterization and microhardness of rapidly solidified Al–Ce alloys. International Journal of Materials Research. 2022 Jan 3;93(6):578-84.

[18] Yang Y, Bahl S, Sisco K, Lance M, Shin D, Shyam A, Plotkowski A, Dehoff RR. Primary solidification of ternary compounds in Al-rich Al–Ce–Mn alloys. Journal of Alloys and Compounds. 2020 Dec 5;844:156048.

[19] Wang Y, Hou F, Fu Z, Mao H, Xu H. Microstructure and mechanical properties of novel heat-resistant Al-12Ce-xCu-yMg alloy under laser melting. Journal of Alloys and Compounds. 2022 Nov 30;924:166359.

[20] Qin G, Lv X, Li K, Yang Z, Sheng T, Zhang S, Wei X, Yu G, Yu J, Song R. Excellent mechanical properties and corrosion resistance of Al–Ce–Zr alloys. Scientific Reports. 2025 Jul 1;15(1):21965.

[21] Wang F, Qiu D, Liu ZL, Taylor JA, Easton MA, Zhang MX. The grain refinement mechanism of cast aluminium by zirconium. Acta materialia. 2013 Sep 1;61(15):5636-45.

[22] Wang L, Ye B, Bai Y, Zhao B, Ding W. Effect of Zr and Sc micro-additions on the microstructure and mechanical properties of as-cast Al-5Ce alloy. Materials Science and Engineering: A. 2021 Aug 3;822:141654.

[23] Odhiambo HW, Singh G, Tasneem M, Soare MA, Leszczewicz J, Cui J, Napolitano RE, Ouyang G, Picu CR. Al–Ce-Based Alloys: Processing, Mechanical Properties, and High-

Temperature Stability. In TMS Annual Meeting & Exhibition 2025 Mar 3 (pp. 87-96). Cham: Springer Nature Switzerland.

[24] Li Y, Bushby AJ, Dunstan DJ. The Hall–Petch effect as a manifestation of the general size effect. Proceedings of the Royal Society A: Mathematical, Physical and Engineering Sciences. 2016 Jun 30;472(2190):20150890.

[25] Nam S, Simsek E, Argibay N, Rios O, Henderson HB, Weiss D, Moore EE, Perron AP, McCall SK, Ott RT. Strength mechanisms and tunability in Al-Ce-Mg ternary alloys enabled by additive manufacturing. Materials & Design. 2023 Jul 1;231:112009.

[26] Gillett HW, Schnee VH. Cerium in Aluminium Alloys. Industrial & Engineering Chemistry. 1923 Jul 1;15(7):709-11.

[27] Langenbeck SL, Griffith WM, Hildeman GJ, Simon JW. Development of dispersion-strengthened Al alloys. Rapidly Solidified Powder Al Alloys. 1986 Jan 1:410-22.

[28] Manca DR, Churyumov AY, Pozdniakov AV, Prosviryakov AS, Ryabov DK, Krokhin AY, Korolev VA, Daubarayte DK. Microstructure and properties of novel heat-resistant Al–Ce–Cu alloy for additive manufacturing. Metals and Materials International. 2019 May 1;25(3):633-40.

[29] Khvan A. Optimization of the phase composition of high-tech Al alloys with a composite structure based on Ce-and Ca containing eutectics (Doctoral dissertation, Ph. D. thesis. NUST MISIS, Moscow).

[30] Weiss D, Rios O, Sims Z, McCall S, Ott R. Casting characteristics of high cerium content Al alloys. InLight Metals 2017 2017 Feb 12 (pp. 205-211). Cham: Springer International Publishing.

[31] Sims ZC, Weiss D, McCall SK, McGuire MA, Ott RT, Geer T, Rios O, Turchi PA. Cerium-based, intermetallic-strengthened Al casting alloy: high-volume co-product development. Jom. 2016 Jul;68(7):1940-7.

[32] Weiss D. Improved high-temperature Al alloys containing cerium. Journal of Materials Engineering and Performance. 2019 Apr 1;28(4):1903-8.

CHAPTER 6: GENERAL CONCLUSION

This research was driven by the need to develop Al-Ce alloys with high-temperature stability at 300 °C for use in structurally demanding environments such as automotive engine components and aircraft structures. The study demonstrates that through a systematic combination of secondary processing (post-casting), targeted alloying, and compositional optimization, the high-temperature performance of Al-Ce alloys can be significantly enhanced. These advancements not only improve mechanical stability under elevated temperatures but also establish a high-value application for Ce – an abundant and currently underutilized rare earth element – thereby increasing resource efficiency and economic viability.

Current materials used in high-temperature aerospace applications, such as Ti-based alloys for aircraft wing skins, are effective but costly and dense. The results of this research show that optimized and thermomechanically processed Al-Ce alloys possess the potential to deliver comparable thermal stability while offering substantial weight reduction and cost advantages. This positions Al-Ce alloys as viable candidates for replacing Ti-based systems in certain structural applications, contributing to improved fuel efficiency, reduced emissions, and enhanced sustainability in aerospace and automotive sectors.

6.1 Processing

In designing our alloy systems, we employed a strategic processing route consisting of three primary steps: casting, extrusion, and rolling. Each of these steps introduces distinct mechanisms of microstructural refinement and strengthening, and their combined effects yield compelling improvements in mechanical performance. In addition, rapid solidification via melt spinning was explored for quaternary alloy variants to further refine the microstructure and evaluate extreme cooling-rate effects on thermal stability and property retention.

Extrusion of both binary Al-Ce and ternary Al-Ce-Mg systems at 300 °C results in substantial enhancement of strength and ductility. In the binary system, the ultimate tensile strength (UTS) increases from approximately 125 MPa in the as-cast Al-10Ce alloy to ~228 MPa after extrusion at 300 °C with an 86 % area reduction, representing a ~100 % increase in UTS. Concurrently, ductility improves from about 13.4 % to ~25 % in the extruded condition. On the microstructural scale, grain refinement plays a critical role, with grain size

reduced from ~582 μm in the as-cast state to ~2 μm post-extrusion. In accordance with the Hall–Petch relation, this grain size reduction is a key contributor to the observed increase in strength. EBSD analysis further reveals the development of a pronounced {110}<112> brass texture in the extrusion direction, which facilitates favorable slip activation and contributes to the enhanced ductility.

In the Al-Ce binary alloy, strengthening arises from the interaction between a soft Al matrix (fcc) and hard $Al_{11}Ce_3$ intermetallic phases. Our findings indicate that precipitation strengthening dominates, as the spatial distribution, morphology, and refinement of the $Al_{11}Ce_3$ phase strongly influence mechanical performance at both ambient and elevated temperatures. During extrusion, the initially coarse, lamellar $Al_{11}Ce_3$ intermetallics present in the as-cast condition are fragmented into finer rod-like dispersoids that are more uniformly distributed within the matrix, improving load transfer and hindering dislocation motion.

High-temperature tensile tests conducted at 300 °C demonstrate that both as-cast and extruded Al-10Ce alloys outperform current state-of-the-art (SOTA) aerospace-grade aluminum alloys above 250 °C. These results confirm that processing-driven microstructural modification – particularly through extrusion – has a profound influence on high-temperature strength retention. Consequently, Al-Ce alloys exhibit strong potential as lightweight, thermally stable alternatives to Ti- and Sc-based alloys for structural applications in demanding thermal environments.

Hot rolling of Al-Ce-Mg alloys introduces additional microstructural refinement, enhancing both strength and ductility. For example, in the Al-10Ce-4Mg alloy, hot rolling results in measurable increases in yield strength, UTS, and elongation compared to the as-cast condition, reflecting improved load-bearing capacity and deformation capability. At room temperature, the Mg addition provides supplemental solid-solution and dispersion strengthening relative to the binary Al-10Ce system. However, this strength differential gradually diminishes with increasing temperature, and the mechanical properties of the rolled Al-10Ce-4Mg and binary alloy converge near 350 °C. This convergence suggests that while Mg contributes to strengthening at lower temperatures, its influence becomes secondary at elevated temperatures where thermally stable $Al_{11}Ce_3$ dispersoids dominate the deformation response.

Rapid solidification has a further profound effect on strengthening in Al-Ce-based alloys. Melt-spinning of the Al-7Ce-14Cu-0.5Zr alloy demonstrates that aging the resulting ribbon does not fundamentally degrade its mechanical properties nor lead to significant microstructural coarsening. Isothermal aging at 350 °C for up to 100 h results in only moderate softening (to ~189 HV, corresponding to ~77 % hardness retention), confirming suppressed coarsening and exceptional thermal stability of the as-spun microstructure. This stability is attributed to the extremely low diffusivity and negligible solubility of Ce in Al, which inhibits intermetallic coarsening and grain growth during high-temperature exposure. Consequently, the synergistic combination of rapid solidification and Ce-rich phase stabilization enables superior property retention and long-term thermal performance.

6.2 Composition

Before determining the appropriate processing route, alloy design plays a critical role in defining the dominant strengthening mechanisms and achievable performance. In the binary Al-Ce system, strengthening is primarily governed by precipitation strengthening resulting from the presence of thermally stable $Al_{11}Ce_3$ intermetallics, which enables tensile strengths of ~228 MPa in the as-extruded condition. However, achieving higher strength and enhanced high-temperature performance requires targeted microalloying to optimize both precipitation behavior and deformation resistance while maintaining an acceptable balance between strength and ductility.

The addition of Mg to form a ternary Al-Ce-Mg alloy increases ambient temperature strength to ~390 MPa due to combined solid-solution strengthening and refined dispersion strengthening. However, this Mg-related solid-solution contribution diminishes at elevated temperatures (~300 °C) due to precipitate dissolution, resulting in a reduction in mechanical performance. Therefore, the alloy design strategy shifts toward engineering thermally stable precipitates capable of retaining strength under long-term exposure to elevated temperatures.

To this end, Zr was introduced into the Al-Ce-Mg system. Literature on Al-Sc-Zr alloys indicates that Zr promotes the formation of Sc-rich cores with Zr-rich shells, which significantly suppress precipitate coarsening at high temperatures. In a similar manner, Zr additions in the present work promote the formation of coherent Al_3Zr precipitates, which exhibit high thermal stability and contribute to improved high-temperature strength retention.

Additionally, Zr acts as a grain refiner, further enhancing strength through grain boundary strengthening.

Driven by these insights, compositional optimization led to the development of a quaternary Al-Ce-Mg-Cu-Zr alloy. Due to the high melting point of Zr, a Cu-Zr master alloy was employed during casting. The presence of Cu enhances melt fluidity and promotes improved diffusivity of Zr, while also contributing to age-hardening through the formation of Al_2Cu precipitates. In the optimized composition Al-10Ce-4Mg-0.25Zr-0.145Cu, hardness increases from ~96 HV in the as-cast condition to ~108 HV after aging at 300 °C for 10 h, demonstrating the effectiveness of microalloying in enhancing thermal stability and precipitation strengthening.

6.3 Future Work

This work has made significant advancements in the microstructural refinement and high-temperature stabilization of Al-Ce-based alloys. Through extrusion, both the Al (fcc) matrix and the $Al_{11}Ce_3$ intermetallic phase undergo substantial refinement, leading to a dramatic transformation in mechanical performance. In the case of Al-10Ce-4Mg, extrusion results in grain refinement and increases in yield strength, ultimate tensile strength, and elongation by factors of approximately 2.5, 2.5, and 10, respectively. Notably, mechanical property retention does not degrade upon thermal aging. This stability is attributed to the high corrosion resistance of the alloy, the extremely low diffusivity of Ce in Al, and the limited solubility of Ce in the Al matrix, which collectively suppress precipitate coarsening and inhibit degradation in mechanical performance.

While this study successfully explored the quaternary Al-Ce-Mg-Zr system, further advancements would benefit from a comprehensive theoretical framework to better understand phase stability, precipitation pathways, and the interactions between microalloying elements. Such a framework is essential for guiding more precise compositional optimization. Overall, the demonstrated microstructural refinement, exceptional high-temperature property retention, and scalability of thermomechanical processing, position Al-Ce alloys as highly promising candidates for replacing heavier and more expensive high-temperature materials in automotive and aerospace structural applications.